FOSSIL



DOE/PC/79854-T1
(DE90005310)

# COMBINED $SO_x/NO_x$ REMOVAL AND CONCENTRATION FROM FLUE GAS THROUGH AN ELECTROCHEMICAL MEMBRANE

Final Report

By
Jack Winnick

November 1989

Work Performed Under Contract No. AC22-87PC79854

For
U. S. Department of Energy
Pittsburgh Energy Technology Center
Pittsburgh, Pennsylvania

By
Georgia Institute of Technology
Atlanta, Georgia

---

## DISCLAIMER



This report has been reproduced directly from the best available copy.

Available to DOE and DOE contractors from the Office of Scientific and Technical Information, P.O. Box 62, Oak Ridge, TN 37831; prices available from (615)576-8401, FTS 626-8401.

Available to the public from the National Technical Information Service, U. S. Department of Commerce, 5285 Port Royal Rd., Springfield, VA 22161.

Price: Printed Copy A08
Microfiche A01

Printed in the United States of America. Office of Scientific and Technical Information, Oak Ridge , Tennessee

DOE/PC/79854--T1

DE90 005310

# Combined $SO_x/NO_x$ Removal and Concentration from Flue Gas through an Electrochemical Membrane

DE-AC22-87PC79854

FINAL REPORT

November 1989

Georgia Institute of Technology

Jack Winnick, P.I.

## TABLE OF CONTENTS

## Titles for Tables

## Titles for Tables cont.

## Titles for Figures

## Titles for Figures

**Executive Summary**

Electrochemical membrane removal of $SO_2$ from flue gas and concentration into a salable by-product stream has been achieved. Full-cell tests have verified both the concept and choice of materials compatible with the process gas. Electrodes have been developed, manufactured from a conducting ceramic, which give performance commensurate with economic guidelines. Electrochemical cell reactions conform precisely with those discerned in free electrolyte. These reactions are stoichiometric to over 95% $SO_2$ removal. Oleum by-product generation is likewise totally stoichiometric (100% current efficiency).

$NO_x$ removal has been found to occur at the oxidizing electrode. A scheme to remove both $SO_2$ and $NO_x$ must thus be somewhat more complex than a one-pass, constant-potential cell stack.

Cell polarization, that is, the achievable current densities at reasonable voltage, is unacceptable with the membranes tested thus far. The problem appears related to lack of sufficient capillarity, due to insufficient particle area, i.e. particle sizes greater than that needed for electrolyte retention.

Future work will focus on identifying a ceramic matrix material and a membrane fabrication technique which yields a membrane with the proper capillarity match with the porous electrodes. This will give the cell the proper polarization performance to permit larger scale endurance tests.

## INTRODUCTION

An electrochemical concentrator was identified some years ago as a potentially viable method for removal and concentration of $SO_x$ from flue gas. The basic process, which operated at 600°C, was modified to permit operation at lower temperatures for retrofitting coal-burning power plants.

The process comprises a means for selectively transforming the $SO_x$ in the flue gas at a gas-diffusion electrode into a sulfoxyanion through reaction with reduced oxygen:

$$SO_2 + O_2 + 2e^- \rightarrow SO_4^{2-} \quad (1)$$

and

$$SO_3 + 1/2\ O_2 + 2e^- \rightarrow SO_4^{2-} \quad (2)$$

These negative ions are absorbed into an electrolyte in intimate contact with the electrode. At 600°C this was simply a mixture of alkali metal sulfates, melting at 512°C. For use below 400°C, a lower melting electrolyte, basically potassium pyrosulfate, was developed. This electrolyte can transport the sulfur anions, but was found to react electrochemically, presumably as

$$S_2O_7^{2-} + 2e^- \rightarrow SO_4^{2-} + SO_3^{2-} \quad (3)$$

The sulfate would then be oxidized at the anode, evolving gaseous $SO_3$ and oxygen.

$$SO_4^{2-} \rightarrow SO_3 + 1/2\ O_2 + 2e^- \quad (4)$$

Later work in free electrolyte showed that instead of (3), the pyrosulfate was reduced as

$$2\ S_2O_7^{2-} + 2e^- \rightarrow 3\ SO_4^{2-} + SO_2 \quad (5)$$

It seems possible that NO may be removed simultaneously with the $SO_3$ from any number of mechanisms, e.g.:

$$NO + O_2 + e^- \rightarrow NO_3^- \quad (6)$$

or

$$2\ NO + 4e^- \rightarrow 2O^{2-} + N_2 \quad (7)$$

A number of other chemical reactions is also possible, involving $SO_3$ as in the chamber process for sulfuric acid manufacture. The $SO_2$ evolved at the cathode would have to be chemically oxidized to $SO_3$ to react with some of the sulfate produced. It was thus necessary to have oxidation catalyst available in the electrolyte; without it, $SO_2$ would be released.

Five Tasks were designated, as stated in the proposal:

1. Optimization of the ceramic membrane
2. Optimization of the electrodes
3. $SO_2$ removal in free electrolyte

4. $NO_x$ removal in free electrolyte

5. Simultaneous $SO_2/NO_x$ removal (full-cell performance tests)

The first four tasks lead directly to the fifth: tests of the complete cell; electrodes and membrane with flowing simulated flue gas. The report is divided into descriptions of the results of these five tasks. This is followed with an analysis of the results; that is, a measure of the relative success of the process and suggestions for future work.

## I. Electrodes

A perovskite, $La_{0.8}Sr_{0.2}CoO_3$, was found to be a suitable electrode material in preliminary tests. The performance of these porous, gas-diffusion electrodes in full cell tests depends largely on the pore structure. These pores must be interconnecting and abundant enough so that diffusion rates of $SO_x$ and $O_2$ in the gas phase through them do not limit the process. In addition, the pores should be small enough so as to maximize the interfacial surface area between the electrodes and ceramic membrane without exerting capillary forces great enough to withdraw significant quantities of electrolyte out of the membrane. Electrode fabrication parameters such as sintering temperature, perovskite particle size, compaction pressure, and effect of binders were examined.

All perovskite was synthesized according to the following recipe:

1. Weigh out stoichiometric quantities of the corresponding metal acetates.
2. Ball mill to a homogeneous powder (4 to 6 hours).
3. Decompose mixture in an alumina crucible for one hour at each of the consecutive temperatures; 130°C, 170°C, 210°C, 240°C, and 275°C.

From this point to the final electrode product, fabrication parameters were varied and their effect examined. The first parameter was a secondary sintering step in which the perovskite from step 3 above was further sintered at either 275°C, 500°C or

800°C overnight. The final perovskite material was then ground and divided into particle size fractions of 177-297 μm, 125-177 μm, 63-125 μm, and < 63 μm. At this point a methylcellulose binder could be added to any of the particle size fractions if so desired. The perovskite particles (and possibly methylcellulose) were then pressed into a disc. The compaction pressure was varied from 20 $kg/cm^2$ to 160 $kg/cm^2$. The final step was sintering the discs at high temperature. These temperatures were varied from 1000°C to 1300°C. The electrodes were examined and tested for strength, density (porosity), and electrical resistance to determine the optimum fabrication conditions.

The results are displayed in tables I-1 through I-12. Tables I-1, -2, -3, -4 correspond to the perovskite synthesized with a secondary sintering step at 275°C, and the electrode discs sintered at 1000°C, 1100°C, 1200°C, and 1300°C respectively. Tables I-5 and I-6 are identical to I-1 and I-2 except that 5% methylcellulose (by weight) was added to the perovskite particles prior to pressing. Tables I-7 through I-10 correspond to the perovskite prepared with a secondary sintering step at 500°C and the electrode discs sintered at 1000°C, 1100°C, 1200°C, and 1300°C respectively. Tables I-11 and I-12 show the results of electrodes made with particles which underwent a secondary sintering step of 800°C.

The results show distinct trends with changes in each parameter. First, as the particle size decreased, electrode strength improved, while porosity and electrical resistance decreased; whereas adding methylcellulose reduced electrode

strength while porosity and electrical resistance increased. Increasing either the compaction pressure or the final sintering temperature resulted in electrodes of improved strength, decreased porosity, and decreased electrical resistance.

The optimum electrode would be one with high strength, maximized porosity, and minimized electrical resistance. Unfortunately, as shown above, the fabrication parameters work against each other somewhat and an absolute optimum does not exist. However, the results show certain conditions are superior. The best conditions appear to include; a secondary sinter at 500°C, a medium particle size (either 125-177$\mu$m or 63-125$\mu$m), no methylcellulose added, a low compaction pressure (either 20 or 40 kg/cm$^2$) and a final sintering temperature of 1100°C or 1200°C.

The fabrication procedure which produced the most effective electrodes included; 1) decomposing the precursor metal acetates at 500°C, 2) grind to a particle size of approximately 60 - 120 $\mu$m, 3) press particles into a disc at 20 to 40 kg/cm$^2$, and 4) sinter disc between 1100°C and 1200°C. This procedure was followed in fabricating each of the perovskite electrodes discussed in this report.

The capabilities of the perovskite electrodes were examined by comparing their performance to nickel oxide electrodes in a molten carbonate membrane cell. The molten carbonate/nickel oxide cell has been characterized in great detail through fuel cell research. The polarization behavior of this cell is well known and was used as a gauge to compare and assess the performance of

perovskite electrodes in this cell.

Figure I-1 shows the cathodic polarization behavior of perovskite electrodes in the molten carbonate cell under a wide range of conditions. Table I-13 displays the exchange current densities calculated from the low polarization data of Figure I-1. The values of the exchange current density were correlated with changes in gas composition and temperature to give:

$$i_o = 9\ (P_{CO_2})^{0.0}\ (P_{O_2})^{0.4}\ \exp(-6000/T) \qquad (8)$$

Where,

$i_0$ = exchange current density, $mA/cm^2$

$P_{CO_2}$ = partial pressure of carbon dioxide, atm

$P_{O_2}$ = partial pressure of oxygen, atm

T = temperature, Kelvin.

In a similar manner, Winnick and Ross[1] correlated the exchange current density to changes in gas composition and temperature for NiO electrodes. The result was:

$$i_o = 150\ (P_{CO_2})^{0.0}\ (P_{O_2})^{0.5}\ \exp\ (-6000/T) \qquad (9)$$

with terms defined as above. Comparing the two correlations shows that the two materials promote electrode kinetics very similarly. The oxygen pressure dependence, probably due to transport limitation in the dissolved state, is nearly the same for both.

Figure I-2 compares actual polarization data of perovskite to that of NiO. The figure shows the polarization behavior of the two

---

[1]Winnick, J. and Ross, P. N., J. Electrochem. Soc., 128 (5), 991, 1981.

materials are comparable. Even at high current densities, where mass transfer effects become important, the performance of the perovskite and NiO are similar.

These "optimized" perovskite electrodes were investigated in detail for 1) structure, under a scanning electron microscope, and 2) performance, as compared to commercial NiO electrodes, in a molten carbonate fuel cell (MCFC). Since the technologies of the electrochemical flue gas clean-up process and MCFC are quite similar, and the NiO/MCFC pair have been characterized in great detail, comparison of the perovskite and NiO in a MCFC provides a good basis for assessing the performance capabilities of the perovskite electrodes.

Figure I-3 displays three electron micrographs, a) perovskite electrode fabricated from 63-125 micron particles, b) perovskite electrode fabricated from powder (sub 38 micron particles), and c) commercial NiO (Gould Inc.). Both perovskite electrodes were fabricated with a 25 $kg/cm^2$ press and an 1100°C sinter, resulting in structures approximately 65% porous with a resistivity of 3 ohm-cm (600°C). As the micrographs indicate, the smaller perovskite particles resulted in a structure with finer pore and grain size. Comparing the finer grain perovskite with the NiO, one can clearly see the two structures are very similar with respect to pore and grain size.

The research with the perovskite and NiO electrodes in the MCFC set-up mainly focused on cathodic polarization. Figure I-4 compares the polarization performance of the two cathodes at 590°C

and various gas compositions. The polarization performance of the perovskite is seen to be comparable and actually slightly better than the NiO. Table I-14 displays values of the exchange current density calculated from polarization data, as a function of the gas composition and temperature. The exchange current density (superficial area basis) was correlated to gas composition and temperature for all of the data in Table 1-14 to give:

$$i_o = 50{,}000\ P_{CO_2}^{0.33}\ P_{O_2}^{0.25}\ \exp\ (-11{,}000/T) \qquad (10)$$

with terms defined as above.

This equation can be compared to that derived for NiO electrodes in a MCFC set-up, equation (9). The two equations differ considerably, especially in the temperature and $CO_2$ partial pressure dependencies, and may indicate a different mechanism for the perovskite electrode.

Figure I-5 displays polarization data of a perovskite cathode under standard MCFC conditions (650°C, 15% $O_2$, 30% $CO_2$ in $N_2$ oxidant gas). In addition, the figure shows polarization data of NiO cathodes reported by the Institute of Gas Technology[2,3] under otherwise identical conditions. The data again show the performance of the perovskite is comparable to that of NiO up to current densities of 250 mA/cm$^2$.

---

[2]Institute of Gas Technology, "Fuel Cell Research on Second Generation Molten Carbonate Systems," Project 61021 Quarterly Report (April, 1979).

[3]Institute of Gas Technology, "Fuel Cell Research on Second Generation Molten Carbonate Systems", Project 8984 Final Status Report (Sept., 1977)

The results reported here show that the perovskite material, $La_{0.8}Sr_{0.2}CoO_3$, can be processed to form an electrode of high porosity, relatively high conductivity with low resistance to gas diffusion. These are precisely the properties needed for the electrodes in the $SO_x/NO_x$ concentrator cell.

Table I-1 Perovskite synthesized with 275°C secondary sinter, pressed discs sintered at 1000°C.

| Particle Size (microns) | Compaction Pressure ($kg/cm^2$) | Density ($g/cm^3$) | Porosity (percent) | Resistance (ohms) | Comments |
|---|---|---|---|---|---|
| 180-300 | 160 | 1.96 | 67.5 | 9.0 | poor strength |
| 180-300 | 80 | 1.72 | 71.5 | 9.6 | poor strength |
| 180-300 | 40 | 1.58 | 73.8 | 10.3 | poor strength |
| 180-300 | 20 | 1.47 | 75.6 | 10.7 | poor strength |
| 125-180 | 160 | 2.04 | 66.2 | 8.3 | poor strength |
| 125-180 | 80 | 1.83 | 69.7 | 8.8 | poor strength |
| 125-180 | 40 | 1.70 | 71.8 | 9.0 | poor strength |
| 125-180 | 20 | 1.55 | 74.3 | 9.6 | poor strength |
| 63-125 | 160 | 2.07 | 65.7 | 8.1 | poor strength |
| 63-125 | 80 | 1.83 | 69.7 | 8.3 | poor strength |
| 63-125 | 40 | 1.73 | 71.3 | 8.8 | poor strength |
| 63-125 | 20 | 1.59 | 73.6 | 9.3 | poor strength |
| under 63 | 40 | 1.79 | 70.3 | 7.7 | poor strength |
| under 63 | 20 | 1.67 | 72.3 | 7.9 | poor strength |

Table I-2 Perovskite synthesized with a 275°C secondary sinter, pressed discs sintered at 1100°C.

| Particle Size (microns) | Compaction Pressure ($kg/cm^2$) | Density ($g/cm^3$) | Porosity (percent) | Resistance (ohms) | Comments |
|---|---|---|---|---|---|
| 180-300 | 160 | 2.83 | 53.1 | 6.0 | adequate strength |
| 180-300 | 80 | 2.40 | 60.2 | 6.4 | adequate strength |
| 180-300 | 40 | 2.15 | 64.3 | 6.7 | adequate strength |
| 180-300 | 20 | 1.87 | 69.0 | 7.6 | adequate strength |
| 125-180 | 160 | 2.89 | 52.1 | 5.9 | adequate strength |
| 125-180 | 80 | 2.49 | 58.7 | 6.0 | adequate strength |
| 125-180 | 40 | 2.18 | 63.8 | 6.4 | adequate strength |
| 125-180 | 20 | 1.99 | 67.0 | 6.9 | adequate strength |
| 63-125 | 160 | 2.88 | 52.2 | 5.7 | adequate strength |
| 63-125 | 80 | 2.50 | 58.5 | 6.0 | adequate strength |
| 63-125 | 40 | 2.20 | 63.5 | 6.2 | adequate strength |
| 63-125 | 20 | 2.05 | 66.0 | 6.6 | adequate strength |
| under 63 | 40 | 2.30 | 61.9 | 5.3 | adequate strength |
| under 63 | 20 | 2.12 | 64.8 | 5.6 | adequate strength |

Table I-3 Perovskite synthesized with a 275°C secondary sinter, pressed discs sintered at 1200°C.

| Particle Size (microns) | Compaction Pressure ($kg/cm^2$) | Density ($g/cm^3$) | Porosity (percent) | Resistance (ohms) | Comments |
|---|---|---|---|---|---|
| 180-300 | 160 | 4.25 | 29.5 | 4.9 | good strength |
| 180-300 | 80 | 3.61 | 40.1 | 5.5 | good strength |
| 180-300 | 40 | 3.40 | 43.6 | 5.7 | good strength |
| 180-300 | 20 | 2.57 | 57.4 | 6.1 | good strength |
| 125-180 | 160 | 4.35 | 27.9 | 5.1 | good strength |
| 125-180 | 80 | 3.75 | 37.8 | 5.1 | good strength |
| 125-180 | 40 | 3.38 | 43.9 | 5.5 | good strength |
| 125-180 | 20 | 2.69 | 55.4 | 5.8 | good strength |
| 63-125 | 160 | 4.32 | 28.4 | 4.8 | good strength |
| 63-125 | 80 | 3.69 | 38.8 | 5.3 | good strength |
| 63-125 | 40 | 3.38 | 43.9 | 5.2 | good strength |
| 63-125 | 20 | 2.65 | 56.1 | 6.0 | good strength |
| under 63 | 40 | 3.50 | 42.0 | 4.7 | good strength |
| under 63 | 20 | 2.72 | 54.9 | 5.0 | good strength |

Table I-4 Perovskite synthesized with a 275°C secondary sinter, pressed discs sintered at 1300°C.

| Particle Size (microns) | Compaction Pressure ($kg/cm^2$) | Density ($g/cm^3$) | Porosity (percent) | Resistance (ohms) | Comments |
|---|---|---|---|---|---|
| 180-300 | 160 | 4.91 | 18.6 | 8.0 | good strength |
| 180-300 | 80 | 4.22 | 30.0 | 9.5 | good strength |
| 180-300 | 40 | 3.90 | 35.3 | 10.8 | good strength |
| 180-300 | 20 | 2.93 | 51.4 | 13.2 | good strength |
| 125-180 | 160 | 5.00 | 17.1 | 5.1 | good strength |
| 125-180 | 80 | 4.35 | 27.9 | 5.1 | good strength |
| 125-180 | 40 | 3.83 | 36.5 | 5.5 | good strength |
| 125-180 | 20 | 3.12 | 48.3 | 5.8 | good strength |
| 63-125 | 160 | 4.77 | 20.9 | 4.8 | good strength |
| 63-125 | 80 | 4.29 | 28.9 | 5.3 | good strength |
| 63-125 | 40 | 3.79 | 37.1 | 5.2 | good strength |
| 65-125 | 20 | 3.20 | 46.9 | 6.0 | good strength |
| under 63 | 40 | 3.91 | 35.2 | 4.7 | good strength |
| under 63 | 20 | 3.36 | 44.3 | 5.0 | good strength |

Table I-5 Perovskite synthesized with a 275°C secondary sinter, 180-300 micron particles with 5% methylcellulose.

| Sintering Temperature (°C) | Compaction Pressure ($kg/cm^2$) | Density ($g/cm^3$) | Porosity (percent) | Resistance (ohms) | Comments |
|---|---|---|---|---|---|
| 1000 | 160 | 1.81 | 70.0 | 9.1 | poor strength |
| 1000 | 80 | 1.56 | 74.1 | 10.0 | poor strength |
| 1000 | 40 | 1.48 | 75.5 | 12.3 | poor strength |
| 1000 | 20 | 1.35 | 77.6 | 20.0 | poor strength |
| 1100 | 160 | 2.47 | 59.0 | 6.7 | adequate strength |
| 1100 | 80 | 2.14 | 64.5 | 7.0 | adequate strength |
| 1100 | 40 | 1.96 | 67.5 | 8.1 | adequate strength |
| 1100 | 20 | --- | --- | -- | electrode fell apart |
| 1200 | 160 | 3.84 | 36.3 | 5.9 | good strength |
| 1200 | 80 | 3.39 | 43.8 | 7.0 | good strength |
| 1200 | 40 | 2.80 | 53.6 | 6.9 | good strength |
| 1200 | 20 | --- | --- | -- | electrode fell apart |
| 1300 | 40 | 4.44 | 26.4 | 5.1 | good strength |
| 1300 | 20 | 3.85 | 36.2 | 5.5 | good strength |
| 1300 | 40 | 3.20 | 46.9 | 6.1 | good strength |
| 1300 | 20 | --- | --- | -- | electrode fell apart |

Table I-6 Perovskite synthesized with a 275°C secondary sinter, 125-180 micron particles with 5% methylcellulose.

| Sintering Temperature (°C) | Compaction Pressure ($kg/cm^2$) | Density ($g/cm^3$) | Porosity (percent) | Resistance (ohms) | Comments |
|---|---|---|---|---|---|
| 1000 | 160 | 1.84 | 69.5 | 8.9 | poor strength |
| 1000 | 80 | 1.65 | 72.6 | 9.6 | poor strength |
| 1000 | 40 | 1.55 | 74.3 | 11.0 | poor strength |
| 1000 | 20 | 1.40 | 76.8 | 15.0 | poor strength |
| 1100 | 160 | 2.62 | 56.6 | 6.3 | adequate strength |
| 1100 | 80 | 2.26 | 62.5 | 6.9 | adequate strength |
| 1100 | 40 | 2.00 | 66.8 | 7.7 | adequate strength |
| 1100 | 20 | --- | --- | -- | electrode fell apart |
| 1200 | 160 | 4.01 | 33.5 | 5.5 | good strength |
| 1200 | 80 | 3.52 | 41.6 | 5.9 | good strength |
| 1200 | 40 | 3.00 | 50.2 | 6.4 | good strength |
| 1200 | 20 | --- | -- | -- | electrode fell apart |
| 1300 | 40 | 4.57 | 24.2 | 4.7 | good strength |
| 1300 | 20 | 3.99 | 33.8 | 5.2 | good strength |
| 1300 | 40 | 3.25 | 46.1 | 6.0 | good strength |
| 1300 | 20 | --- | --- | -- | electrode fell apart |

Table I-7 Perovskite synthesized with a 500°C secondary sinter, pressed discs sintered at 1000°C.

| Particle Size (microns) | Compaction Pressure ($kg/cm^2$) | Density ($g/cm^3$) | Porosity (percent) | Resistance (ohms) | Comments |
|---|---|---|---|---|---|
| 180-300 | 160 | 2.14 | 64.5 | 6.7 | poor strength |
| 180-300 | 80 | 1.92 | 68.2 | 7.4 | poor strength |
| 180-300 | 40 | 1.77 | 70.6 | 8.5 | poor strength |
| 180-300 | 20 | 1.69 | 72.0 | 8.9 | poor strength |
| 125-180 | 160 | 2.21 | 63.3 | 5.5 | poor strength |
| 125-180 | 80 | 1.98 | 67.2 | 6.5 | poor strength |
| 125-180 | 40 | 1.80 | 70.1 | 7.3 | poor strength |
| 125-180 | 20 | 1.69 | 72.0 | 8.2 | poor strength |
| 63-125 | 160 | 2.16 | 64.2 | 6.0 | poor strength |
| 63-125 | 80 | 1.95 | 67.7 | 6.5 | poor strength |
| 63-125 | 40 | 1.73 | 71.3 | 7.5 | poor strength |
| 63-125 | 20 | 1.59 | 73.6 | 7.7 | poor strength |
| under 63 | 40 | 1.87 | 69.0 | 5.0 | poor strength |
| under 63 | 20 | 1.77 | 70.6 | 5.6 | poor strength |

Table I-8 Perovskite synthesized with a 500°C secondary sinter, pressed discs sintered at 1100°C.

| Particle Size (microns) | Compaction Pressure ($kg/cm^2$) | Density ($g/cm^3$) | Porosity (percent) | Resistance (ohms) | Comments |
|---|---|---|---|---|---|
| 180-300 | 160 | 2.68 | 55.6 | 4.0 | warped slightly |
| 180-300 | 80 | 2.48 | 58.9 | 4.5 | adequate strength |
| 180-300 | 40 | 2.30 | 61.9 | 5.1 | adequate strength |
| 180-300 | 20 | 2.12 | 64.8 | 4.9 | adequate strength |
| 125-180 | 160 | 2.98 | 50.6 | 3.1 | warped slightly |
| 125-180 | 80 | 2.75 | 54.4 | 3.3 | adequate strength |
| 125-180 | 40 | 2.45 | 59.4 | 3.7 | adequate strength |
| 125-180 | 20 | 2.31 | 61.7 | 4.6 | adequate strength |
| 63-125 | 160 | 3.16 | 47.6 | 2.8 | warped slightly |
| 63-125 | 80 | 2.85 | 52.7 | 3.1 | adequate strength |
| 63-125 | 40 | 2.54 | 57.9 | 3.7 | adequate strength |
| 63-125 | 20 | 2.32 | 61.5 | 3.8 | adequate strength |
| under 63 | 40 | 3.00 | 50.2 | 3.0 | adequate strength |
| under 63 | 20 | 2.80 | 53.6 | 3.5 | adequate strength |

Table I-9 Perovskite synthesized with a 500°C secondary sinter, pressed discs sintered at 1200°C.

| Particle Size (microns) | Compaction Pressure ($kg/cm^2$) | Density ($g/cm^3$) | Porosity (percent) | Resistance (ohms) | Comments |
|---|---|---|---|---|---|
| 180-300 | 160 | 4.04 | 33.0 | 3.5 | warped slightly |
| 180-300 | 80 | 3.63 | 39.8 | 3.9 | good strength |
| 180-300 | 40 | 3.39 | 43.8 | 3.9 | good strength |
| 180-300 | 20 | 3.21 | 46.8 | 4.8 | good strength |
| 125-180 | 160 | 4.38 | 27.4 | 2.9 | warped slightly |
| 125-180 | 80 | 3.94 | 34.7 | 3.5 | good strength |
| 125-180 | 40 | 3.59 | 40.5 | 3.4 | good strength |
| 125-180 | 20 | 3.44 | 43.0 | 3.8 | good strength |
| 63-125 | 160 | 4.42 | 26.7 | 2.4 | warped slightly |
| 63-125 | 80 | 4.08 | 32.3 | 3.0 | good strength |
| 63-125 | 40 | 3.72 | 38.3 | 2.8 | good strength |
| 63-125 | 20 | 3.42 | 43.3 | 2.9 | good strength |
| under 63 | 40 | 4.40 | 27.0 | 2.6 | good strength |
| under 63 | 20 | 3.75 | 37.8 | 2.8 | good strength |

Table I-10 Perovskite synthesized with a 500° secondary sinter, pressed discs sintered at 1300°C.

| Particle Size (microns) | Compaction Pressure ($kg/cm^2$) | Density ($g/cm^3$) | Porosity (percent) | Resistance (ohms) | Comments |
|---|---|---|---|---|---|
| 180-300 | 160 | 4.80 | 20.4 | 3.2 | warped slightly |
| 180-300 | 80 | 4.39 | 27.2 | 3.1 | good strength |
| 180-300 | 40 | 4.06 | 32.7 | 3.3 | good strength |
| 180-300 | 20 | 3.80 | 37.0 | 3.6 | good strength |
| 125-180 | 160 | 5.04 | 16.4 | 2.4 | warped slightly |
| 125-180 | 80 | 4.57 | 24.2 | 3.4 | good strength |
| 125-180 | 40 | 4.12 | 31.7 | 2.9 | good strength |
| 125-180 | 20 | 3.85 | 36.2 | 3.1 | good strength |
| 63-125 | 160 | 5.01 | 16.9 | 2.2 | warped slightly |
| 63-125 | 80 | 4.56 | 24.4 | 2.4 | good strength |
| 63-125 | 40 | 4.05 | 32.8 | 2.3 | good strength |
| 63-125 | 20 | 3.73 | 38.1 | 2.6 | good strength |
| under 63 | 40 | 4.73 | 21.6 | 1.9 | good strength |
| under 63 | 20 | 4.00 | 33.7 | 2.0 | good strength |

Table I-11 Perovskite synthesized with a 800°C secondary sinter, 180-300 micron particles.

| Sintering Temperature (°C) | Compaction Pressure ($kg/cm^2$) | Density ($g/cm^3$) | Porosity (percent) | Resistance (ohms) | Comments |
|---|---|---|---|---|---|
| 1000 | 160 | 2.48 | 58.9 | 4.0 | poor strength, warped slightly |
| 1000 | 80 | 2.28 | 62.2 | 4.6 | poor strength, warped slightly |
| 1000 | 40 | 2.15 | 64.3 | 4.9 | poor strength, warped slightly |
| 1000 | 20 | 2.05 | 66.0 | 5.4 | poor strength, warped slightly |
| 1100 | 160 | --- | --- | 2.7 | electrodes warped |
| 1100 | 80 | --- | --- | 3.1 | electrodes warped |
| 1100 | 40 | --- | --- | 3.0 | electrodes warped |
| 1100 | 20 | --- | --- | 3.5 | electrodes warped |
| 1200 | 160 | --- | --- | 1.6 | electrodes warped badly |
| 1200 | 80 | --- | --- | 1.8 | electrodes warped badly |
| 1200 | 40 | --- | --- | 1.8 | electrodes warped badly |
| 1200 | 20 | --- | --- | 2.0 | electrodes warped badly |
| 1300 | 40 | --- | --- | 1.4 | electrodes warped badly |
| 1300 | 20 | --- | --- | 1.4 | electrodes warped badly |
| 1300 | 40 | --- | --- | 1.6 | electrodes warped badly |
| 1300 | 20 | --- | --- | 1.7 | electrodes warped badly |

Table I-12 Perovskite synthesized with a 800°C secondary sinter, 125-180 micron particles.

| Sintering Temperature (°C) | Compaction Pressure ($kg/cm^2$) | Density ($g/cm^3$) | Porosity (percent) | Resistance (ohms) | Comments |
|---|---|---|---|---|---|
| 1000 | 160 | 2.70 | 55.2 | 4.1 | poor strength, warped slightly |
| 1000 | 80 | 2.32 | 61.5 | 4.4 | poor strength, warped slightly |
| 1000 | 40 | 2.19 | 63.7 | 4.8 | poor strength, warped slightly |
| 1000 | 20 | 2.04 | 66.2 | 5.3 | poor strength, warped slightly |
| 1100 | 160 | --- | --- | 3.0 | electrodes warped |
| 1100 | 80 | --- | --- | 2.7 | electrodes warped |
| 1100 | 40 | --- | --- | 3.0 | electrodes warped |
| 1100 | 20 | --- | --- | 3.3 | electrodes warped |
| 1200 | 160 | --- | --- | 1.4 | electrodes warped badly |
| 1200 | 80 | --- | --- | 1.7 | electrodes warped badly |
| 1200 | 40 | --- | --- | 1.7 | electrodes warped badly |
| 1200 | 20 | --- | --- | 1.9 | electrodes warped badly |
| 1300 | 40 | --- | --- | 1.3 | electrodes warped badly |
| 1300 | 20 | --- | --- | 1.3 | electrodes warped badly |
| 1300 | 40 | --- | --- | 1.6 | electrodes warped badly |
| 1300 | 20 | --- | --- | 1.6 | electrodes warped badly |

Table I-13 Exchange current densities calculated from the polarization data in Figure I-1.

| $O_2$ (%) | $CO_2$ (%) | Flow rate (cc/min) | Temp(°C) | $i_0$ (mA/cm$^2$) |
|---|---|---|---|---|
| 10 | 25 | 100 | 590 | 35.7 |
| 25 | 25 | 100 | 590 | 46.9 |
| 50 | 25 | 100 | 590 | 57.3 |
| 10 | 10 | 100 | 590 | 32.7 |
| 10 | 50 | 100 | 590 | 31.7 |
| 10 | 25 | 200 | 590 | 31.6 |
| 10 | 25 | 400 | 590 | 29.9 |
| 10 | 25 | 100 | 550 | 23.0 |

Table I-14 Exchange Current Densities Calculated from Polarization Data

| $O_2$, % | $CO_2$ % | T, °C | $i_o$, mA/cm$^2$ |
|---|---|---|---|
| 50. | 20. | 590 | 67.0 |
| 10. | 20. | 590 | 52.1 |
| 2. | 20. | 590 | 36.1 |
| 0.5 | 20. | 590 | 23.5 |
| 20. | 50. | 590 | 67.0 |
| 20. | 10. | 590 | 46.9 |
| 20. | 2. | 590 | 28.4 |
| 20. | 0.5 | 590 | 15.6 |
| 15. | 30. | 650 | 145.0 |
| 15. | 30. | 600 | 81.0 |
| 15. | 30. | 590 | 62.0 |
| 15. | 30. | 550. | 35.0 |

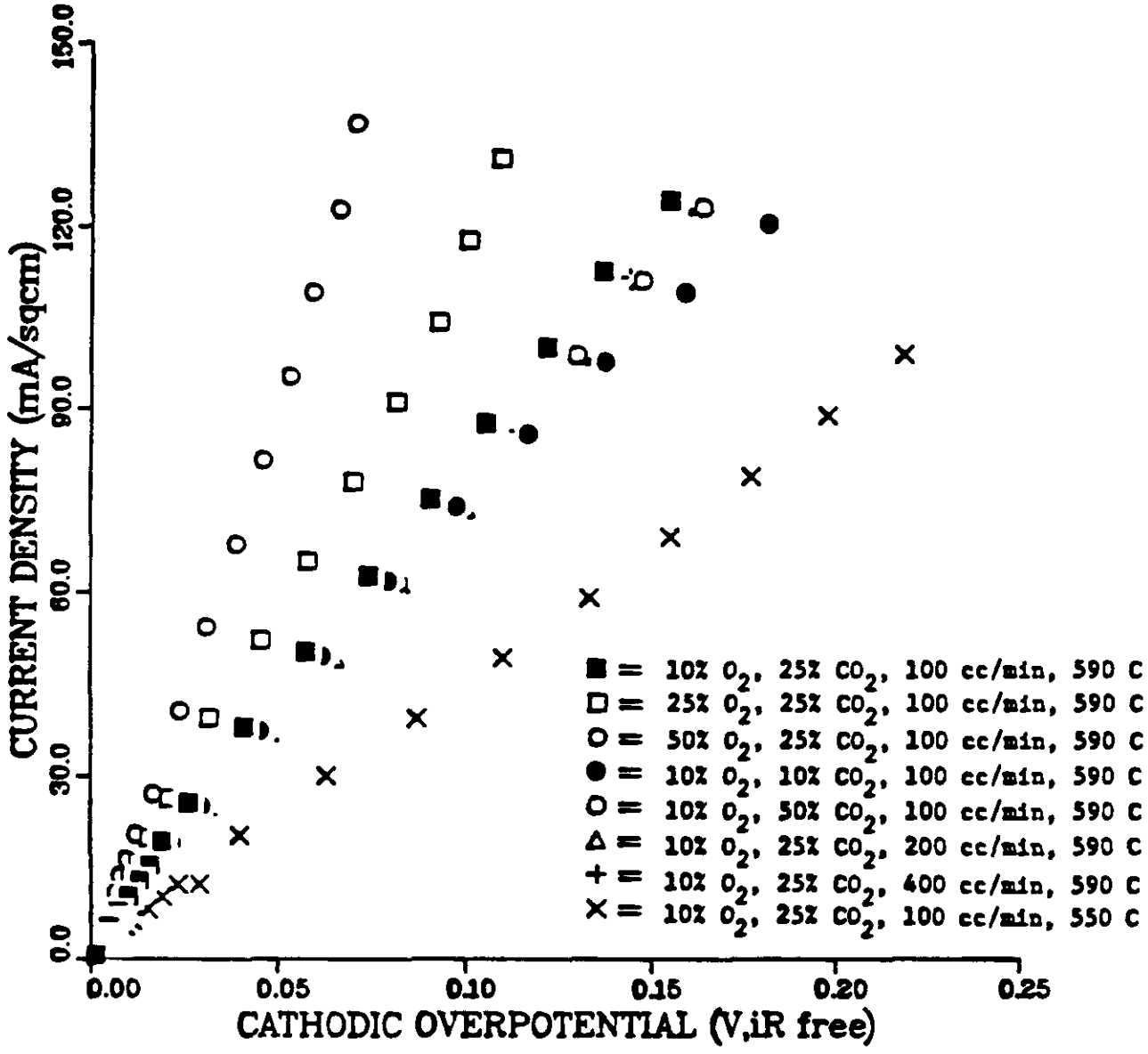


Figure I-1 Cathodic carbonate eutectic polarizations using a porous perovskite electrode.

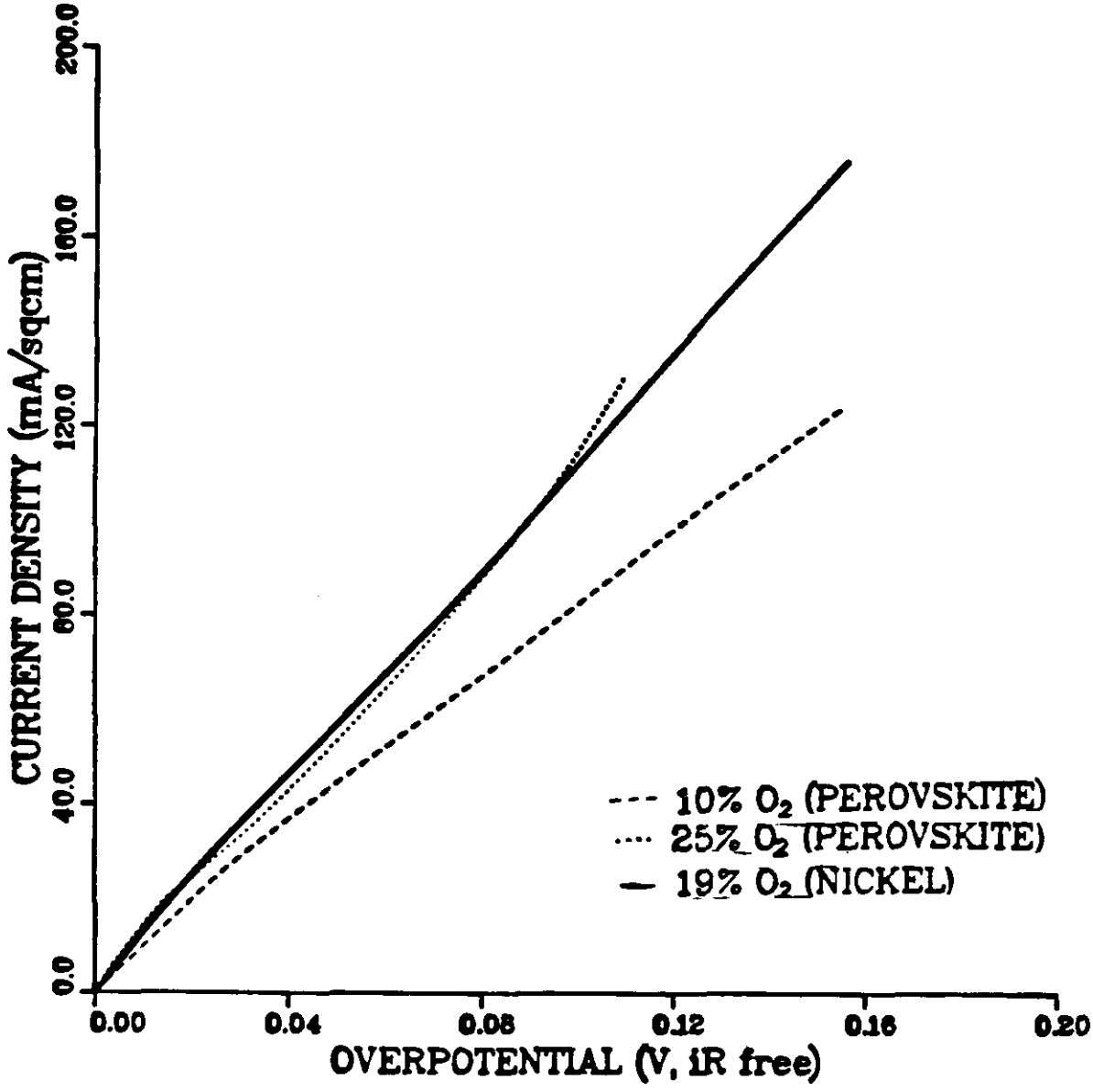


Figure I-2 Comparison of the polarization characteristics of perovskite ($La_{0.8}$ $Sr_{0.2}$ $CoO_3$) and NiO

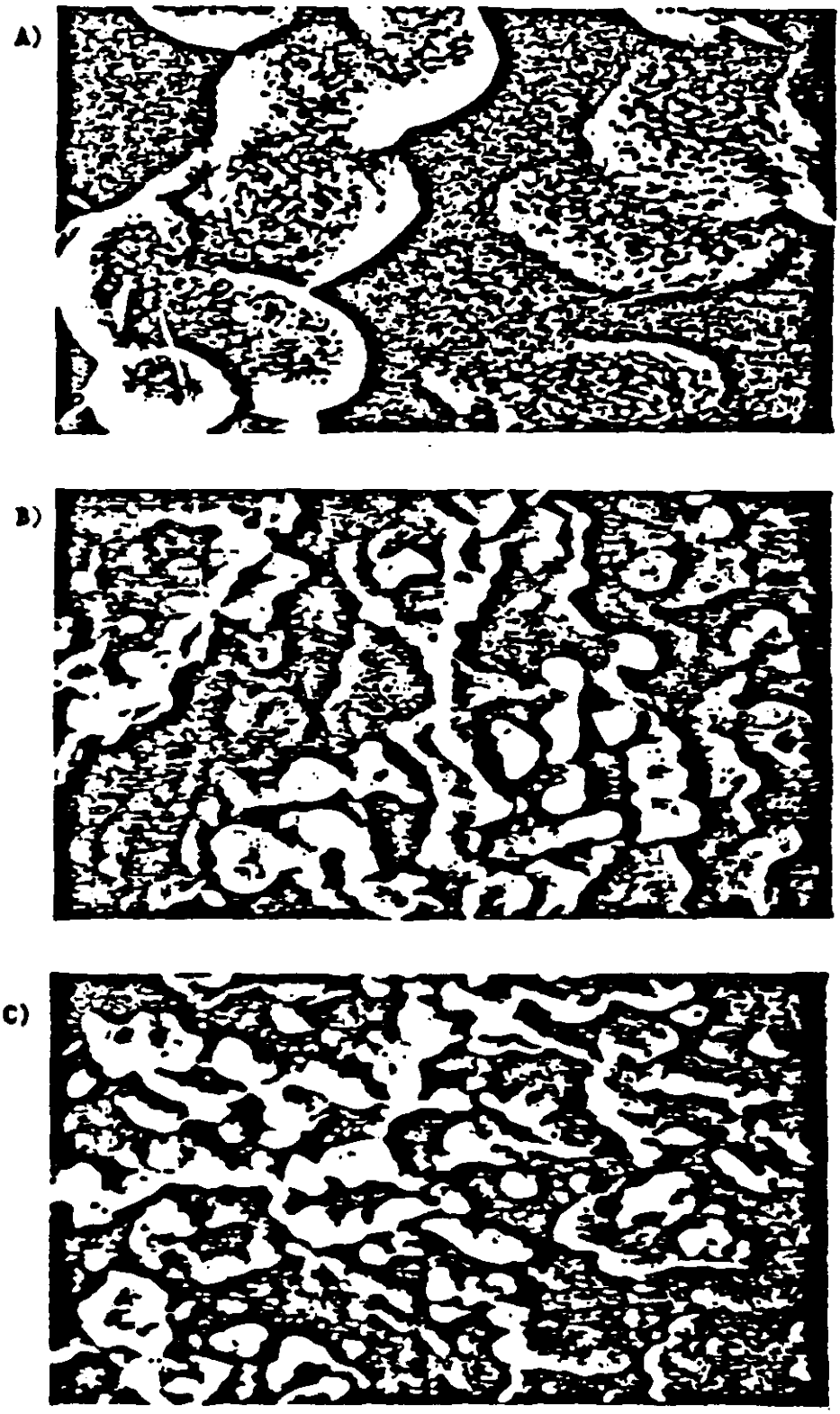


Figure I-3 Electron micrographs of A) perovskite, 63 to 125 micron particles B) perovskite, sub 38 micron particles and C) MiO (Gould Inc.). Magnification is 10,000 X (1 cm. = 1 micron).

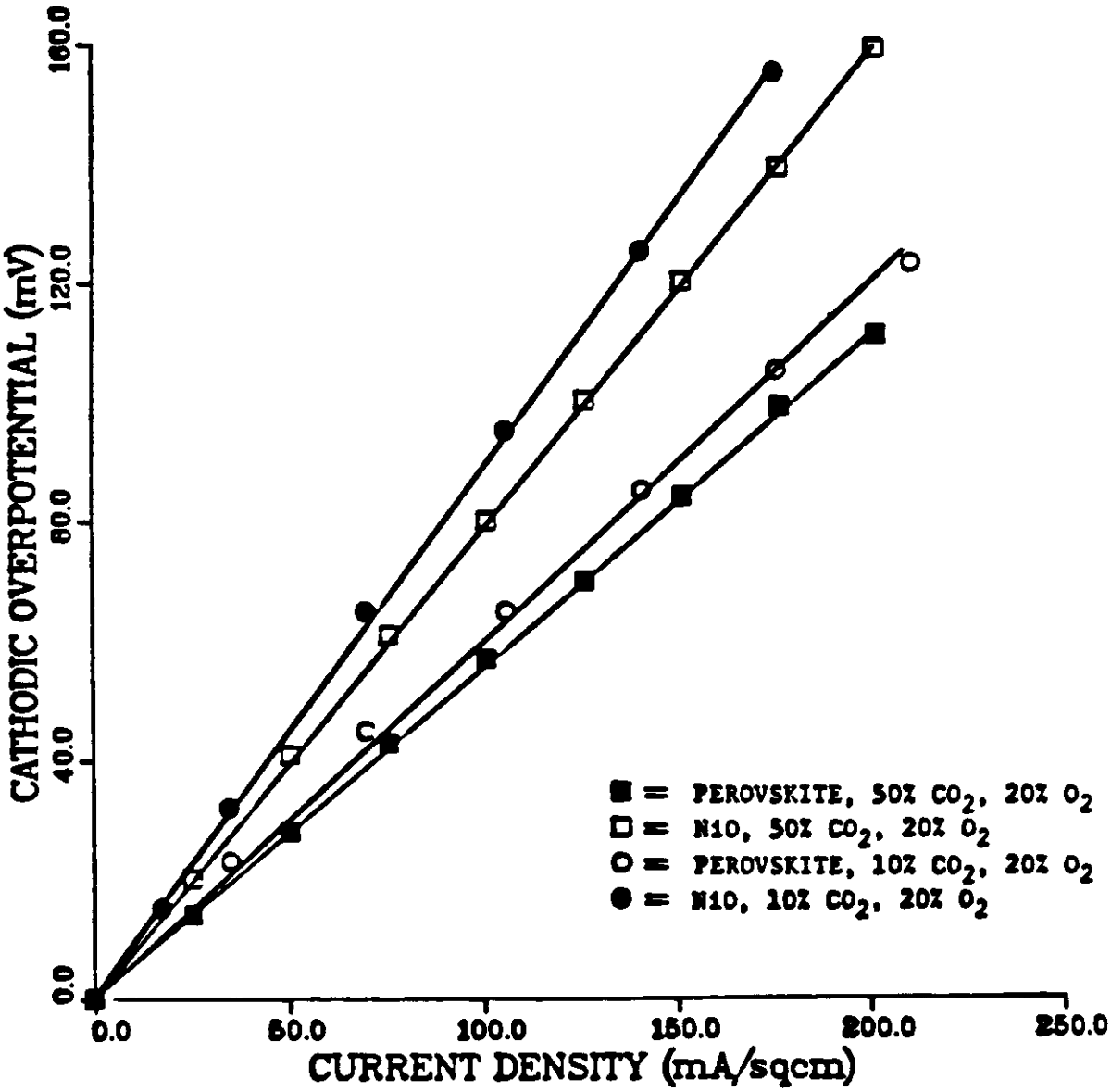


Figure I-4 **IR-free cathodic polarizations at 590°C. NiO polarization data comes from** (Winnick and Ross) J. Electrochem. Soc, 128 (5), 991, 1981.

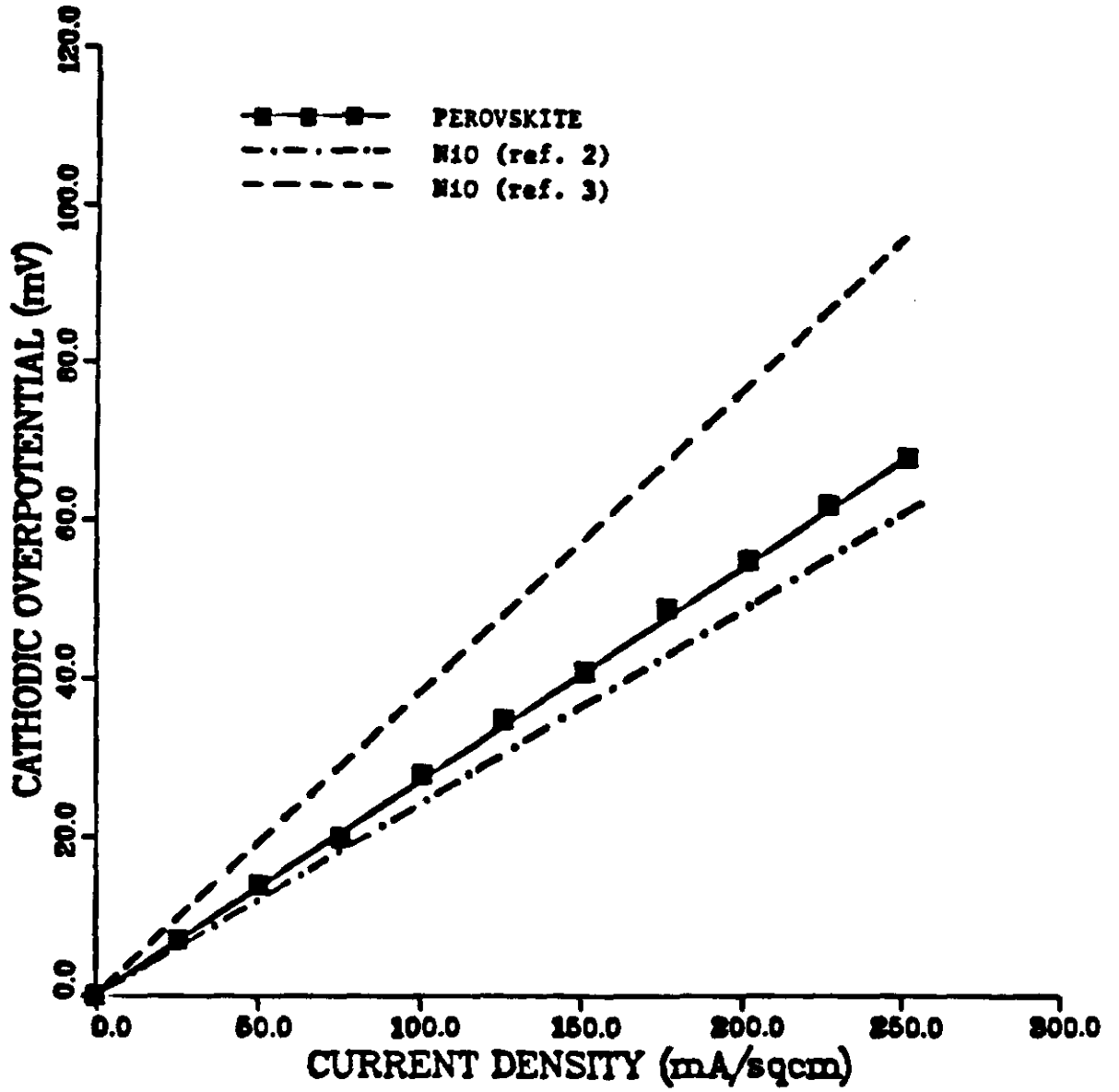


Figure I-5 IR-free cathodic polarizations at 650°C with a standard oxidant gas of 15% $O_2$, 30% $CO_2$ in $N_2$.

II. Electrolyte Membrane

The electrolyte membrane serves the dual purpose of separating the flue gas from the product gas and providing a medium for transport of sulfur oxides. The molten electrolyte is retained by a matrix of particles through capillarity. Since a porons electrode is on each side of the membrane and exerts its own capillarity, membrane capillarity must exceed that of the electrodes. This condition prevents electrolyte from flooding the electrode pores and maintains the available interfacial area. Several matrix materials were used to make a membrane with sufficient capillarity relative to the electrodes.

A. MgO

The early work conducted on the membrane was with MgO as the matrix material. Past studies had indicated MgO is actually a precursor to the true matrix due to the reaction between MgO and the $K_2S_2O_7$ electrolyte base:

$$2MgO + 2\ K_2S_2O_7 \rightarrow K_2Mg_2(SO_4)_3 + K_2SO_4 \qquad (11)$$

so that the $K_2Mg_2(SO_4)_3$ produced becomes the true matrix material. The sulfate produced in the reaction dissolves in the excess electrolyte. Research has shown the optimal fabrication technique for producing the membrane (on the basis of membrane density, strength and texture in the molten state) is as follows.

1. Ball mill 13.0% MgO, 87% electrolyte (99% $K_2S_2O_7$, 1% $V_2O_5$), all weight basis, to a homogeneous powder.
2. React mixture at 400°C overnight.
3. Cool, and then grind and ball mill to a homogeneous powder (particle size <74 $\mu$m).
4. Place 15 grams of powder in a 3 inch diameter die. The die should be equipped with aluminum foil discs to prevent sticking on top and bottom.

5. Heat die and powder to 150°C for 3 hours to drive off any absorbed $H_2O$ from the powder.
6. Press powder in die at 10,000 lbs pressure right after removal from 150°C furnace.
7. Place pressed powder and die, still assembled, in 280°C furnace for 3 to 6 hours.
8. Quickly remove powder and die assembly from furnace and repress at 10,000 lbs pressure.
9. Remove outer ring of the die, then place die top, bottom and pressed membrane in 280°C furnace and allow to cool slowly (3 hours minimum).
10. Remove membrane, peeling aluminum foil from the membrane faces.

The resultant membrane is approximately 1.5 mm thick, nearly 100% dense, and quite strong mechanically. In the molten state, above 280°C, the membrane becomes a paste, with a texture comparable to toothpaste. These attributes are similar to those of commercial molten carbonate membranes used in fuel cells. At this point, the MgO membranes appeared to be ready for use in the electrochemical cell.

B. Glass

Membrane work was also done with a glass as the matrix material. Previous investigations have identified borosilicate as a material which is inert to the corrosive electrolyte, and therefore a suitable matrix material.

Increased amounts of vanadium pentoxide (vanadia) catalyst were added to the electrolyte in order to promote direct, in situ oxidation of $SO_2$ to $SO_3$. The first electrolyte membranes contained one percent vanadia (by weight). By increasing the vanadia content to five percent, we accelerated the rate-determining $SO_2$ oxidation step and thereby eliminated the need for a pre-oxidation catalyst.

matrix to have a particle size near 10 microns.

Reducing the particle size will increase the adhesion - cohesion property of the matrix and, as a result, keep the electrolyte out of the electrode pores. Electrolyte membranes were subsequently manufactured with Corning borosilicate glass particles. The 325 mesh particles have a maximum size of 43 microns with most particles under 4 microns. We have found that this size can be further reduced by milling; when milled for 24 hours, all particles are less than 10 microns and most are fractions of a micron. By using borosilicate particles, we are able to decrease the matrix particle size by at least an order of magnitude compared to the MgO-based matrices.

With the new matrix material, we were forced to develop a new fabrication technique. The previous MgO-based matrix was hot pressed into membranes at 275°C. The new membrane mixture is molten below this temperature. We completed melting point studies of various electrolyte compositions to aid the development of this membrane fabrication technique.

Table II-1 shows the melting point ranges for electrolytes with various levels of vanadia loading. These tests were conducted by mixing the sample in a glass tube and then sealing the tube. By using sealed tubes, we intended to establish an equilibrium between pyrosulfate and sulfate ions in the molten electrolyte by retaining any generated $SO_3$. (Recall that pyrosulfate decomposes to sulfate and sulfur trioxide; sulfate raises the melting point. If a partial pressure of $SO_3$ is not established, sulfate continues

to accumulate). Table II-1 shows that vanadia decreases the melting point of the mixture.

Table II-2 shows the results of another melting point study. Here the mixed samples were dried, melted and further heated to 400°C to drive off $SO_3$. When the samples had cooled, we sealed the end of the tube and checked the melting point. While these results are valid, our membranes exhibit a lower melting point than that found in this study. This could be caused by further evolution of $SO_3$ and $K_2SO_4$, which would raise the melting point in the sealed tubes.

We have developed a membrane fabrication technique to be used with the borosilicate particles. Tnis method yields a membrane with 92% of its theoretical density. With further development, we should reach 99% of theoretical density. Experience with molten carbonate fuel cell membranes shows that this density is needed for full performance.

The process consists of mixing 0.5 grams of $V_2O_5$, 9.5 grams of $K_2S_2O_7$ and 10.0 grams of borosilicate particles in a ball mill for 24 hours. This mixture was pressed into a crude membrane and reacted for three hours at 400°C. This step created an equilibrium composition of pyrosulfate and sulfate by driving off $SO_3$. Since the remainder of this procedure is carried out below 400°C, no $SO_3$ bubbles should form in the membrane.

When cool, this mixture was crushed and milled for another 24 hours. The powder was poured on an aluminum foil layer inside the three inch diameter die, leveled off and covered by another layer

24 hours. This mixture was pressed into a crude membrane and reacted for three hours at 400°C. This step created an equilibrium composition of pyrosulfate and sulfate by driving off $SO_3$. Since the remainder of this procedure is carried out below 400°C, no $SO_3$ bubbles should form in the membrane.

When cool, this mixture was crushed and milled for another 24 hours. The powder was poured on an aluminum foil layer inside the three inch diameter die, leveled off and covered by another layer of foil. The die with powder and the top half of the die were placed in an 150°C oven for three hours to dry the powder. The die was removed, the top piston fitted and then the powder pressed under 9000 psi with a hydraulic press. The die was brought to the final press temperature and held there for three hours. After this, the membrane was pressed at 9000 psi, the outer ring was removed and the pistons and membrane were returned to the oven to cool.

Table II-3 shows the results obtained with this technique. Many of these membranes were molten and flowed out of the die under pressure. Membranes of varying composition have been fabricated, but we have concentrated on membranes having 5 wt.% vanadium pentoxide. This focus has enabled us to improve our fabrication technique to where we can make a near-uniform membrane at a high percentage of its theoretical density.

Several other matrix materials were tested in an attempt to improve the overpotential behavior of the electrochemical membrane. A dry-box was used during the fabrication steps to prevent the

membrane from becoming contaminated with water. Also, organic dispersants were used to discourage aggregation of the dry materials during milling.

C. Other Matrix Powders

We have seen limited improvement with the borosilicate particles but have decided to widen the spectrum of matrix materials. The new materials in Table II-4 hold promise for our membranes because of their small particle size, narrow size distribution and chemical inertness. The materials we have obtained are listed in Table II-4. Also, we have ball milled a sample of our borosilicate glass particles for one week to decrease the particle size and distribution.

1) We have tried regrinding an old MgO-based membrane to decrease the matrix particle size and thereby increase the electrolyte retention. A previously fabricated MgO membrane was crushed, milled, and dried in a vacuum desiccator. The mix was then pressed according to our standard procedure with a final press temperature of 277°C. This was too hot and the molten electrolyte extruded from the die.

2) Borosilicate particles had been milled for six days, reducing their size to the 0.5 - 4 μm range. Twelve grams of this glass and eight grams of 5 wt. % $V_2O_5$ electrolyte were dry-milled overnight and reacted at 400°C, as in previous studies. The resulting mass was milled and pressed into a membrane which had 83% of its theoretical density.

3) We investigated the use of zeolites by a preliminary

screening test. This test consisted of mixing samples of zeolite and electrolyte in a sealed glass tube (Table II-5). Before mixing, all zeolites were placed in a vacuum desiccator for two days to desorb water. The electrolyte was pre-mixed to insure each sample contained the same mixture. A control sample tube of electrolyte was prepared for melting point determinations. All tubes were placed in an oven and brought to 200°C.

At this temperature, the control had melted and the tube containing sample #4 had exploded. The most probable cause of the explosion is off-gassing of adsorbed water and other gases at the elevated temperature (zeolites are highly hygroscopic). When heated to 230°C, the silicalite sample had wet spots of molten electrolyte distributed throughout the mix. All other samples were changing to shades of tan and beige. This behavior continued as the samples were heated to 250, 260 and 270°C. The electrolyte appears to melt and adsorb in the zeolite structure.

The amount of adsorption appears to be directly related to the polar nature of the zeolite matrix. 13X and 4A have a low $SiO_2$:$Al_2O_3$ ratio, making them highly polar. The polar nature of the matrix attracts the electrolyte and permits chemisorption in the pores. Silicalite has a $SiO_2$:$Al_2O_3$ ratio of 280, making it non-polar and thus reducing the chemisorption in the pores.

4) Several of the membranes we made have suffered from inhomogeneities. These are areas of either high particle concentration or high electrolyte concentration. Areas of high particle concentration allow the membrane to dry out during full

cell operation and allow gas to cross over. In areas of high electrolyte concentration, the electrolyte floods the electrode pores upon reaching the melting point. We believe these difficulties are due to electrolyte aggregation during the milling process. To reduce these inhomogeneities, we have begun using a dry-box during all membrane fabrication steps. All membrane components are dried in either a vacuum desiccator or oven before entering the dry-box. Our first attempt with the dry-box consisted of mixing 10 g of electrolyte with 10 g of borosilicate glass which had been milled for six days (Table II-1). This membrane mixture was milled overnight. When the mill was scraped out, we noticed that all of the mix was packed into one corner of the mill. The resulting membrane was at 83% of theoretical density, $\rho_{th}$, with aggregates of glass visible throughout. These inhomogeneities were due to the severe packing of the mixture inside the mill.

Our next attempt with the dry-box used 12 g of electrolyte and 8 g of borosilicate glass (milled six days). The mixture was milled for twelve hours, returned to the dry-box, scraped and milled for another twelve hours. The intermediate scraping was used to decrease inhomogeneities. This membrane was pressed at 210°C and partially extruded from the die, resulting in a wedge-shaped disk at 84% of $\rho_{th}$.

5) With use of the dry box, it was apparent that inhomogeneities were caused by aggregation of the powders inside the mill. To avert this condition, we searched for a suitable organic dispersant. The first chemical we tried was acetone. A MgO-

based membrane with 5.7 wt.% $V_2O_5$ (2.6 g MgO, 17.4 g $K_2S_2O_7$, 1.0 g $V_2O_5$) was milled overnight with 25 ml of acetone. After fabrication at 270°C, the membrane was removed and found to be ashen grey instead of yellow/green. The membrane had a distinct smell of acetates, leading us to believe the electrolyte had reacted with the acetone.

We then tried using hexane and decane as dispersants, with success. We dried 5 g of Silicalite to 210°C and then stirred in 15 g of pre-mixed electrolyte. This mix was cooled in the vacuum desiccator to prevent it from reabsorbing water. The mix was milled with hexane which kept all particles in a thick slurry. Hexane was removed in the dry box entry port by applying vacuum. The resulting powder was very fluffy and uniform in appearance. After processing, the resulting membrane was at 90% of $\rho_{th}$ and visibly homogeneous.

After one successful silicalite membrane, we proceeded with this zeolite as a matrix replacement. Silicalite has an affinity for water and atmospheric gases causing a processing difficulty. To combat this problem, we are storing the silicalite under vacuum for several days before use. However, when the matrix is mixed with electrolyte and heated to 400°C, the resulting molten mass becomes very puffy and loaded with bubbles. These bubbles come from desorbed gases.

6) DuPont's LUDOX silica particles (Table II-4) were also tried as a matrix. A sample of LUDOX silica suspension was dehydrated to form lumpy silica gel. The lumps were crushed in mortar and pestle and milled (dry) overnight. The resulting powder

was fired at 600°C to force out excess water. This process allows any surface OH groups to dehydrogenate and form Si-O-Si bonds. 10 g of these particles were heated to 210° C and mixed with 10 g of electrolyte, which was not enough to wet all particles. Another 40 g of electrolyte was added to form a thick mixture. The mix was then removed, cooled in the vacuum desiccator and milled with approximately 50 ml of hexane and 50 ml of decane. Again, the organic was removed in the evacuated inlet port of the dry box.

7) We tried to make a borosilicate disc by mixing glass particles with LUDOX, dehydrating, pressing and sintering. All attempts failed, with the disc crumbling during sintering. The apparent cause is segregation of particles during dehydration. Borosilicate particles are larger and settle faster, leaving the LUDOX on top. This prevents any bonding by the LUDOX.

D. Glass Discs

In another development, we have received porous glass membranes from Dr. T. Nakashima at the Industrial Research Institute of Miyazaki Prefecture in Japan. These glass membranes have the following properties:

| Average Pore Size (μm) | Pore Volume (cc/g) | Porosity |
|---|---|---|
| 0.46 | 0.50 | 0.531 |
| 0.92 | 0.47 | 0.528 |

The membranes possess a very narrow pore-size distribution as an added advantage. These properties appear to be ideal for our electrolyte membrane. The pores are twenty times smaller than those in the electrodes and therefore should be able to retain the

electrolyte better than the present particle matrices.

To determine if the porous glass would wet with electrolyte, we conducted a simple test. A membrane and some electrolyte were heated in separate petri dishes. When the electrolyte had melted, the glass membrane was dipped into the electrolyte. The membrane readily wetted and formed translucent areas. With the success of this test, we set out to find a way to impregnate the membrane with electrolyte.

We determined how much electrolyte the pores would hold from the weight and pore volume. A sealed glass container was constructed for impregnating the glass. Inlet and outlet tubes allowed us to control the gas environment around the membrane and therefore prevent excess sulfate buildup. The membrane was supported on alumina posts and a measured amount of electrolyte was loaded on top. To establish a strong $SO_3$ environment, a mixture of 10.4% $SO_2$, 21.6% $O_2$ in $N_2$ was passed through the Haldor-Topsoe $SO_2$ oxidation catalyst (at 400°C) and fed to the glass container. Analysis showed 90% conversion of $SO_2$. With this gas flow established, the membrane was slowly heated to 250° C.

At approximately 200° C, the electrolyte began to melt on the surface of the glass membrane and form beads. Further heating would not decrease the surface tension of the melt and allow it to flow into the pores. On cooling, the container was opened and the beads were found to have solid outer shells with molten centers. Postmortem analysis showed the porous glass to be loaded with acid.

From this analysis, we have determined why the membrane would

not fill with electrolyte. The low melting point is due to the presence of bisulfate in the electrolyte. Water reacts with the electrolyte as follows:

$$K_2S_2O_7 + H_2O \Longrightarrow 2\ KHSO_4 \qquad (12)$$

Bisulfate melts at 214°C. This bisulfate then decomposes in reaction (13),

$$2\ KHSO_4 \Longrightarrow K_2SO_4 + H_2SO_4 \qquad (13)$$

with the sulfuric acid going to water and sulfur trioxide at higher temperatures. It is apparent that the porous glass was not thoroughly dry at the start. When heated, this water desorbed and reacted with the $K_2S_2O_7$ to form $K_2SO_4$ and $H_2SO_4$. The sulfuric acid appears to have entered the pores and excluded the molten electrolyte. After washing with distilled water, the membrane was still loaded with acid; boiling distilled water, made basic with NaOH, removed the acid.

The porous glass membranes still hold great promise and testing continues. It appears that all components must be thoroughly dry during processing. To accomplish this, the electrolyte and porous glass must be heated separately and then mixed.

Work on the porous glass membrane shifted to finding a procedure to clean residual electrolyte from the pores. A 0.1 M $K_2CO_3$ solution was prepared for this purpose. The membrane was immersed in this solution and began to produce small bubbles, believed to be $CO_2$. The solution was brought to a boil to enhance the electrolyte removal. The membrane was then thrice rinsed in

boiling distilled water. When cooled, the membrane was rinsed in cold distilled $H_2O$. The clean membrane was dried for a day at 150°C.

After the membrane was cleaned, a different technique was used to impregnate the membrane with electrolyte. The membrane and a quantity of electrolyte powder were placed in separate petri dishes and heated slowly to the electrolyte's melting point, 250° C. This low melting point is due to a small quantity of $KHSO_4$ in the raw $K_2S_2O_7$. With further heating, the bisulfate decomposes to sulfate and water, as mentioned above. The water evaporates in the present setup. The hot membrane was placed on top of the molten electrolyte and proceeded to absorb the electrolyte. Spots of electrolyte were visible on the upper surface. After these areas became significant, the membrane was turned over. The oven temperature was gradually increased during the process to keep the electrolyte in a molten state. The heat was turned off and the membrane was allowed to cool slowly to 240°C. At this temperature, the membrane was removed to the vacuum desiccator to exclude atmospheric water.

Unfortunately, this final cooling caused the membrane to shatter into many little pieces. The fractures are due to either thermal stresses (rapid cooling) or mechanical stresses (expanding gas bubbles under the applied vacuum). On a positive note, this fracturing did allow inspection of the interior of the membrane. We noted that the electrolyte had not thoroughly penetrated the membrane except in a few areas. Much of the interior was untouched by the electrolyte.

This membrane impregnation technique was repeated on a smaller piece of porous glass. When the membrane was placed on top of the molten puddle of electrolyte, a brown spot of electrolyte quickly appeared. This grew and new spots appeared in a short time. However, these spots grew to cover only 30% of the whole top surface. The piece was removed and allowed to cool slowly to room temperature. Excess electrolyte remained on the lower surface of the membrane.

During the above procedure, we noticed that the electrolyte was forming a surface film, probably of higher melting sulfates. The mechanism for sulfate formation is described above. We realized that to prevent the formation of this sulfate film, we would need a faster impregnation method. We decided that the quickest way would be to subject the membrane to a small vacuum and pour the molten electrolyte on the top surface.

We melted the electrolyte inside a narrow test tube. This reduces the exposed surface area, limiting the rate of decomposition for the electrolyte ($K_2S_2O_7 = K_2SO_4 + SO_3$). With a low level of sulfate, the electrolyte does not form the surface film.

A small piece of membrane was encased between layers of aluminum foil and secured on top of a vacuum filtration flask. The foil had open areas to expose the membrane. Vacuum was applied to the flask and the molten electrolyte was poured on top of the hot membrane. The electrolyte proceeded to flow between the layers of foil, circumventing the membrane. Some small areas of the membrane were discolored, showing the presence of electrolyte. The change

in weight of the membrane showed low quantities of electrolyte absorbed in the pores (15% of the theoretical value).

The process was repeated with the foil wrapped around the sides of the piece. The whole assembly was fitted into the filtration flask's neck. This did not provide a better seal, as all of the electrolyte ran around the sides of the membrane through several small leaks. The membrane did not show any weight gain.

The use of a slight vacuum still appears promising for impregnating the membrane. We have made a glass fixture for a whole three inch diameter membrane. The process will be repeated on both a virgin membrane and a pre-cleaned membrane.

E. Summary

The ideal membrane fabrication procedure has not yet been found. Hot-pressing mixtures of matrix and electrolyte has produced the best membranes to date; however, the particle sizes of the matrix materials have been too large for adequate electrolyte retention. New materials, silicone carbide and silicon nitride, made from a new process to yield unprecedented purity and small particle size, have just been made available to us by Phillips Petroleum. These may form more retentive membranes.

Glass discs made in Japan from sub-micron particles may provide a good support for the electrolyte. We are continuing to explore means of loading.

Fibrous glass mats with sub-micron pores show strong electrolyte affinity. Tests with these membranes are now ongoing.

Table II-1: Electrolyte Melting Points

| $V_2O_5$(g) | $K_2S_2O_7$(g) | Vanadia (%) | Melting Point Range (°C) |
|---|---|---|---|
| 0.01351 | 1.33496 | 1.002 | 250 |
| 0.02620 | 1.28554 | 1.997 | 235 - 240 |
| 0.03969 | 0.95239 | 4.001 | 235 - 240 |
| 0.05094 | 0.96728 | 5.003 | 230 - 235 |
| 0.09740 | 0.87554 | 10.011 | 230 |

Table II-2: Electrolylte Melting point for pre-treated electrolyte

| Vanadia (%) | Melting Point Range (°C) |
|---|---|
| 1.095 | 295 - 300 |
| 5.000 | 270 - 275 |

Table II-3: Borosilicate - based membranes

| Weight of components | Percent Vanadia | Processing Steps | Percent of theoret. density |
|---|---|---|---|
| 0.20 g $V_2O_5$<br>5.0 g $K_2S_2O_7$<br>15.0 g borosilicate | 3.9% | 3 hrs. @ 150° C; press; 3 hrs. @ 280° C; press. | 75% |
| 0.50 g $V_2O_5$<br>9.5 g $K_2S_2O_7$<br>10.0 g borosilicate | 5 % | Dry 3 hrs. @ 150° C; react 3 hrs. @ 400° C; mill; dry 3 hrs. @ 150°C; press; 3 hrs. @ 230° C; press. | 92.3% |
| same | 5 % | Dry 3 hrs. @ 150° C; react 3 hrs. @ 400° C; mill; dry 3 hrs. @ 150°C; press; 3 hrs. @ 225° C; press | 90.2% |
| same | 5 % | React 3 hrs. @ 400° C; mill; dry 3 hrs. @ 150° C; press, 4 hrs. @ 220° C; press | 91.3% |
| same | 5 % | React 3 hrs. @ 400° C; mill; dry 3 hrs. @ 150° C; press; 3 hrs. @ 215° C | 89% |
| 1.00 g $V_2O_5$<br>9.5 g $K_2S_2O_7$<br>9.5 g borosilicate | 9.6% | 3 hrs. @ 150° C; press; 3 hrs. @ 230° C; press. | 95% |
| 1.00 g $V_2O_5$<br>7.0 g $K_2S_2O_7$<br>12.0 g borosilicate | 12.5% | 3 hrs. @ 150 ° C; press; 3 hrs. @ 230° C; press. | 87% |

Table II-4: Alternate Matrix Material

| Material | Composition by weight | Particle size, μm | Pore size, Å |
|---|---|---|---|
| borosilicate glass | Corning 7740 | 1 - 30 | ------- |
| Silicalite | $SiO_2:Al_2O_3$ = 280 | 1 - 5 | 5.5 |
| 13X Zeolite | $SiO_2:Al_2O_3$ = 4 | 1 - 5 | 7 |
| 4A Zeolite | $SiO_2:Al_2O_3$ = 1 | 1 - 5 | 4 |
| 5A Zeolite | $SiO_2:Al_2O_3$ = 1 | 1 - 5 | 5 |
| ball milled glass | Corning 7740 | 1 - 5 | ------- |
| LUDOX AS-40 | $SiO_2:Al_2O_3$ = 270 | 22 x $10^{-3}$ | ------- |

Table II-5: Zeolite - Electrolyte Mixture Test Samples

| Sample # | Zeolite | Mix Compositon |
|---|---|---|
| 1 | 13 X | 1.0000 g 13 X<br>0.9968 g electrolyte |
| 2 | Silicalite | 0.9633 g Silicalite<br>0.9583 g electrolyte |
| 3 | 4 A | 0.9564 g 4 A<br>1.0007 g electrolyte |
| 4 | 5 A | 0.9564 g 5 A<br>1.0038 g electrolyte |
| Control | ----- | 0.9903 g electrolyte |

## III. $SO_x$ Removal

### A. Preoxidation Catalyst

The oxidation of $SO_2$ to $SO_3$ is a key step in the electrochemical removal of $SO_2$. Although vanadia, as an electrolyte additive, enhances oxidation, the geometry of the removal cells limited the overall conversion to unacceptably low values. To eliminate the conversion problem, the $SO_2$ can be oxidized in a simple reactor unit just upstream of the electrochemical removal cells.

The catalyst initially chosen to promote the reaction was platinum dispersed on a porous, inert support. This catalyst is reported in literature as the most active toward oxidation. Two types of inert supports were investigated, alumina and silica gel. The alumina was supplied by Alcoa, with a surface area of 150 $m^2/g$ and nominal pore diameter of approximately 400 angstroms. The silica gel was purchased from Davisil, with a surface area of 300 $m^2/g$ and a pore diameter of 150 angstroms. The supports were impregnated with platinum using chloroplatinic acid solutions as follows:

1. 10 to 20 grams of inert support were weighed out.
2. The quantity of distilled water which would saturate the support pores was measured into a graduated cylinder (this quantity was approximately 10% more than the support weight).
3. The desired amount of chloroplatinic acid was dissolved in the distilled water (final catalysts contained from 0.2% to 3.0% platinum by weight).
4. The support and acid solution were then mixed and allowed to sit for at least two hours.

The impregnated supports were then dried at 100°C for 2 to 3 hours and then reduced under flowing hydrogen at 450°C overnight.

The catalysts were tested for activity by flowing an $SO_2$ containing gas through a simple reactor containing catalyst and monitoring the inlet and outlet $SO_2$ concentrations. The reactor was basically a pyrex tube containing a preweighed plug of catalyst situated in a temperature controlled furnace. The results are reported in Table III-1.

Each of the reaction tests utilized approximately 0.6 grams of catalyst so that the conversions of different runs can be compared, representing relative catalytic activity.

The catalyst with the highest activity is clearly the 3.0% platinum on alumina (30 mesh). The conversion, 99% for each condition examined, is equivalent to equilibrium conditions for the $SO_2/SO_3$ gas components (initially 0.3% $SO_2$, 3% $O_2$). Thus, the maximum conversion is achieved using this catalyst. The early $SO_2$ removal studies utilized this catalyst to oxidize the $SO_2$ just prior to being introduced to the electrochemical cells.

## B. Pre-Oxidation Catalyst: Effluent Analysis

As mentioned in the previous section, the oxidation of sulfur dioxide is the rate-limiting step. Early full cell tests used a 2% platinum-on-silica-gel catalyst to oxidize the $SO_2$ before the flue gas entered the removal cell. We then identified and procured a commercially available sulfuric acid catalyst to replace the noble metal catalyst.

This catalyst, from Haldor-Topsoe, Inc., is used in the manufacture of sulfuric acid where concentrated $SO_2$ streams are encountered. Conversion data is unavailable for the low (0.3%) $SO_2$ concentrations in our flue gas. In order to effectively use this catalyst, we must generate a conversion versus flow rate matrix for the range of operating temperatures which could be used in an actual removal process.

We designed and built a reactor to contain the catalyst particles and it is envisioned that a similar reactor could easily be added to a full scale flue gas cleanup process. The reactor, Figure III-1, consists of inert glass beads to distribute the flow, 30 ml of catalyst and another layer of glass beads to reduce gas channelling effects. The body of the reactor is enclosed in a cylindrical heater which permits operation up to 450° C.

The reactor is believed to work well since the $SO_3$ is visually observed and also detected with wet chemical analysis under operating conditions, but problems were encountered in quantitatively analyzing this effluent. The $SO_3$ decreased the sensitivity of the gas chromatograph's thermal conductivity detector (TCD) and caused inaccurate results. The cause is apparent filament corrosion from either $SO_3$ or $H_2SO_4$ since the sulfur trioxide may combine with trace quantities of water to form sulfuric acid:

$$SO_3 + H_2O \rightarrow H_2SO_4 \qquad (14)$$

or oleum:

$$2\ SO_3 + H_2O \rightarrow H_2S_2O_7 \qquad (15)$$

To resolve this problem, we attempted to do the analysis on the gas chromatograph's flame photometric detector (FPD). The FPD is sulfur specific and we hoped to be able to simultaneously analyze both $SO_2$ and $SO_3$ with this method.

The operation of the detector is quite involved because the detector burns a fuel-rich flame of hydrogen in an oxygen enriched air environment and the response of the detector is a strong function of the fuel to oxygen ratio and the total mass flow rate through the detector. Basically, hydrogen acts to reduce the sulfur compounds to free, gaseous sulfur and the sulfur atoms then combine to create an electronically excited $S_2$ molecule. This molecule returns to its ground state, emitting light at 3940 Å. The FPD has a filter that permits only this wavelength to enter the photomultiplier tube, where a current is produced to drive the GC's integrator.

Figure III-2 shows a typical calibration curve for our FPD. It is quite apparent that the response, GC Area, is non-linear over the range of sulfur input. However, it appears that a linear dynamic range exists in the higher sulfur concentrations. These results are similar to those seen in the literature.

C. Effluent Analysis

Despite the apparent success of the FPD, the GC does not give a clear separation between $SO_2$ and $SO_3$. The concentration of $SO_3$ in the anode and cathode outlet streams must be monitored by a simple method. Since the boiling point of $SO_3$ is 41° C, condensation makes $SO_3$ analysis by gas chromatography difficult and unreliable. The

modified cell permits the exit gasses to be contacted with distilled water just after exiting the cell. Two methods were found to be effective in monitoring $SO_3$ concentrations. Both methods involve absorption of the $SO_3$ into distilled water where the reaction:

$$H_2O + SO_3 \rightarrow H_2SO_4 \qquad (14)$$

takes place rapidly and the pH of the solution is a function of the amount of $SO_3$ absorbed. The first method involves passing the $SO_3$ containing gas over a distilled water reservoir. Here, care is taken to contact the gas and water immediately after the gas exits the furnace so that no $SO_3$ condenses before contact with the reservoir. A large contact area is also required so that no $SO_3$ escapes without undergoing reaction. The second method involves completely condensing the $SO_3$ and collecting the condensate in a distilled water receptacle. In this case the gas exiting the furnace is given a large amount of time before contacting the distilled water so that the $SO_3$ has completely condensed.

Table III-2 gives results of the first method to monitor $SO_3$ concentration. The calibration data show that the $SO_3$ exiting the cell/furnace is completely absorbed in the distilled water reservoir and the resulting sulfuric acid completely dissociates to sulfate and hydrogen ions.

$$H_2SO_4 \rightarrow 2H^+ + SO_4^{2-} \qquad (16)$$

Thus, one $SO_3$ absorbed corresponds to two $H^+$ ions formed in solution. The sampling times in this method are kept short, 5 minutes since the condensate is not collected in a steady stream

but in periodic drops. The data shows the experimentally measured pH deviates slightly from the calculated value, especially at lower pH. The deviation is due to incomplete dissociation of the sulfuric acid at higher acid concentrations:

$$H_2SO_4 \rightarrow H^+ + HSO_4^- \quad (17)$$

so that less than two hydrogen ions are formed for each $SO_3$ absorbed in this case. This postulate is confirmed by the data in Table III-4 where increments of sulfuric acid were added to distilled water with the pH being monitored after each increment. The experimental and calculated pH values deviate as above in the lower pH region. The activity coefficient for hydrogen ion, derived from the data in Table III-4, is plotted versus total sulfur in the distilled water. The final column in Table III-3 represents the calculated pH for each case, corrected by using the appropriate activity coefficient. The experimental and calculated (with activity taken into account) values of pH in Table III-3 correspond well.

Preliminary tests were conducted to examine $SO_3$ removal in electrolytes with various sulfate concentrations and no applied currents to the cell. Previous electrochemical studies of the electrolyte have shown sulfate is the main product at the cathode, where $SO_x$ removal occurs. Pyrosulfate is regenerated in the removal reaction:

$$SO_3 + SO_4^{2-} \rightarrow S_2O_7^{2-} \quad (18)$$

Table III-5 shows the results for $SO_3$ removal in three different electrolytes. Essentially complete removal of $SO_3$ was achieved in

both (94% $K_2S_2O_7$, 5% $K_2SO_4$, 1% $V_2O_5$) and (89% $K_2S_2O_7$, 10% $K_2SO_4$, 1% $V_2O_5$). These results indicate $SO_2$ oxidation kinetics were a limiting factor on $SO_x$ removal in previous cells. The present cell alleviates this limitation and much higher removal is observed.

A simple run was conducted to test for NO removal in the new cell. The result is shown in Table III-5; essentially no NO was removed.

D. Free Electrolyte Study: $SO_x$Removal

The experiments on $SO_x$ removal in free electrolyte concluded this phase of research. The results, shown in Figures III-3 and III-4, are consistent with earlier results. Figure III-3 shows how $SO_x$ removal varies with sulfate concentration in the electrolyte, for an inlet $SO_2$ concentration of 0.3%. As the sulfate concentration increases, the removal increases quickly and above approximately 4.0% sulfate, >99% $SO_x$ removal is achieved. It is also seen that at a fixed sulfate concentration, $SO_x$ removal increases as the gas flow rate through the cell decreases. This indicates that mass transfer is the limiting factor in the present configuration. Figure III-4 displays very similar results, but in this case the inlet $SO_2$ concentration is 1.0%. The same trends for $SO_x$ removal with sulfate concentration and flow rate are observed.

Three conclusions regarding the $SO_x$ removal process can be drawn from the free electrolyte tests. First $SO_2$ oxidation to $SO_3$ is key step in the mechanism. Second, the main removal reaction

$$SO_3 + SO_4^{2-} \rightarrow S_2O_7^{2-} \quad (19)$$

depends on the availability of sulfate and regeneration of pyrosulfate in the electrolyte. Lastly, if mass transfer limitations are removed, greater than 99% $SO_x$ removal can be achieved even at low sulfate concentrations.

## E. $SO_2$ Removal without Pre-Oxidation Catalyst: Full Cell

The free electrolyte studies in Section D showed that the following reactions occur at the cathode of the removal cell:

$$2\ S_2O_7^{2-} + 2\ e^- \rightarrow 3\ SO_4^{2-} + SO_2 \quad (20)$$

$$2\ SO_2 + O_2 \rightarrow 2\ SO_3 \quad (21)$$

$$2\ SO_3 + 2\ SO_4^{2-} \rightarrow 2\ S_2O_7^{2-} \quad (22)$$

These reactions yield an overall cathodic reaction of:

$$SO_2 + O_2 + 2\ e^- \rightarrow SO_4^{2-} \quad (23)$$

The free electrolyte studies also showed that the oxidation of sulfur dioxide (reaction (21)) is the rate limiting step.

We have run the flue gas desulfurization cell using the standard electrolyte tile of composition 86 wt. % $K_2S_2O_7$, 13 wt. % MgO and 1 wt. % $V_2O_5$ without the pre-oxidation catalyst in order to determine the $SO_2$ removal under normal operating conditions. Figure III-5 shows that, at 365°C, there is a net generation of $SO_2$ at a rate proportional to the applied current. The oxidation is incapable of keeping up with the electrolysis at this temperature.

Figure III-6, for the cell at 390°C, again shows a net

generation of $SO_2$, but to a lesser extent. Figure III-7 shows overall removal of $SO_2$ in the cathode stream. The cell was operated at 400°C and at this temperature, the oxidation reaction converts all of the $SO_2$ generated by electrolysis. We know that as the temperature increases, so do the $SO_2$ oxidation kinetics.

Figure III-8 shows the greatest removal of all four runs. This is because the operating temperature of 445°C enables $SO_2$ oxidation to occur at a higher rate. This run was carried out at a higher flow rate to reduce any possible mass transfer resistances which might have occurred from the increased $SO_2$ removal. Table III-6 elaborates on the operating conditions of all four runs.

In summary, the experiments without a pre-oxidation catalyst again confirm that the oxidation of sulfur dioxide to sulfur trioxide is the rate limiting step. This is seen from the net generation of $SO_2$ at lower operating temperatures and net removal at higher temperatures. Since the oxidation kinetics improve with rising temperature and the rate of the electrolysis reaction is directly proportional to the current flow, we see that removal increases with increasing temperature. We also see that at high temperatures, the oxidation is rapid enough to remove all of the generated $SO_2$, with a weak dependence on applied current.

F. $SO_2$ Removal without Pre-oxidation Catalyst: Full Cell

A full cell study was conducted for a membrane containing 5 wt.% $V_2O_5$ in $K_2S_2O_7$ electrolyte with an equal weight of borosilicate added. This study was conducted for several reasons: first, to determine the effect of the higher vanadia loading on the $SO_2$

oxidation; second, to see if the current efficiency was equal to or better than that obtained with the old MgO-based membrane and finally to determine the effect of the reduced particle size on the electrolyte retention and hence polarization performance. The membrane used in this study was at 92% of its theoretical density and nearly homogeneous.

This study was carried out under conditions similar to the study discussed in the previous section. In section E, a full-cell study was carried out with a 1% vanadia electrolyte membrane and no pre-oxidation catalyst at 365, 380, 400 and 445°C. The lower temperatures confirmed that the oxidation of sulfur dioxide to sulfur trioxide is the rate limiting step. Recall that one of the steps in the reaction mechanism involves the generation of $SO_2$ through the electrolysis reaction:

$$2\ S_2O_7^{2-} + 2\ e^- \quad \longleftrightarrows \quad 2\ SO_2 + 2\ SO_4^{2-} + O_2^{2-} \qquad (24)$$

The electrolysis is directly proportional to the current flow. This $SO_2$, along with that in the feed gas, must be converted to $SO_3$ for removal. At higher temperatures, the vanadia oxidizes the $SO_2$ from the electrolysis step. This allows the cell to have a net removal with increasing temperature.

We concluded that it is possible to remove $SO_2$ in the cell without the pre-oxidation catalyst; however, we also realized that we would not reach our design specification level of 80% removal with the 1% vanadia electrolyte membrane. The results of the previous section are included with our present findings for comparison. Numerical values are given in Table III-7.

Figure III-10 shows sulfur oxide removal at 365°C. It is immediately seen that the 5% vanadia electrolyte removes $SO_x$ while the 1% electrolyte has a net generation with applied current. It is apparent that the added vanadia provides sufficient catalytic sites for the oxidation reaction at this flow rate. Note that the flow rate in the present study is 30% higher than in the previous study. Figure III-11 provides the details of the runs at 380°C. Again, the new membrane shows removal with applied current while the old membrane shows generation. The new membrane had an 84% current efficiency at 10 mA compared to the value of 36% for the old membrane.

Figure III-12 reveals interesting results. Here we see similar $SO_x$ removals for both electrolyte compositions at 400°C. This phenomenon is best explained through reaction kinetics. At this temperature, the oxidation occurs so quickly that the 1% vanadia is capable of reacting all generated $SO_2$. While it would appear that there are sufficient reaction sites in both membranes, the current efficiency data are quite different. At 10 mA applied current, the new membrane has a 99% efficiency while the old membrane has a 54% efficiency (Table III-7). Recall that the present flow rate is 30% higher.

These results show that a 5 wt.% vandia electrolyte is better than a 1 wt.% vanadia membrane for a no-pre-oxidation removal cell. Our studies showed net removals at all temperatures for the 5% electrolyte while the 1% electrolyte had net generation at low temperatures. The current efficiencies emphasize this improvement.

$$2\ S_2O_7^{2-} + 2\ e^- \rightarrow 2\ SO_2 + 2\ SO_4^{2-} + O_2^{2-} \quad (24)$$

$$SO_2 + O_2^{2-} \rightarrow SO_4^{2-} \quad (25)$$

$$2\ SO_2 + 2\ SO_4^{2-} \rightarrow 2\ S_2O_6^{2-} \quad (26)$$

$$2\ S_2O_6^{2-} \rightarrow 2\ SO_3 + 2\ SO_3^{2-} \quad (27)$$

$$2\ SO_3^{2-} + O_2 \rightarrow 2\ SO_4^{2-} \quad (28)$$

$$2\ SO_3 + 2\ SO_4^{2-} \rightarrow 2\ S_2O_7^{2-} \quad (29)$$

Reactions (24) through (29) give a net cathodic reaction of:

$$SO_2 + O_2 + 2\ e^- \rightarrow SO_4^{2-} \quad (30)$$

At the anode,

$$SO_4^{2-} \rightarrow SO_3 + \tfrac{1}{2}\ O_2 + 2\ e^- \quad (31)$$

Earlier research showed that one electron transport is possible through the following mechanism:

$$2\ S_2O_7^{2-} + e^- \rightarrow 2\ SO_2 + 2\ SO_4^{2-} + O_2^- \quad (32)$$

$$2\ SO_2 + 2\ SO_4^{2-} \rightarrow 2\ S_2O_6^{2-} \quad (33)$$

$$2\ SO_2 + O_2^- \rightleftharpoons SO_3 + SO_3^- \quad (34)$$

$$SO_3^- + \tfrac{1}{2}\ O_2 + e^- \rightleftharpoons SO_4^{2-} \quad (35)$$

$$2\ S_2O_6^{2-} \rightleftharpoons 2\ SO_3 + 2\ SO_3^{2-} \quad (36)$$

$$2\ SO_3^{2-} + O_2 \rightleftharpoons 2\ SO_4^{2-} \quad (37)$$

$$3\ SO_3 + 3\ SO_4^{2-} \rightleftharpoons 3\ S_2O_7^{2-} \quad (38)$$

Reactions (32) through (38) yield a net cathodic reaction of

$$2\ SO_2 + 3/2\ O_2 + 2\ e^- \rightleftharpoons S_2O_7^{2-} \quad (39)$$

The corresponding anodic reaction is

$$S_2O_7^{2-} \rightleftharpoons 2\ SO_3 + \tfrac{1}{2}\ O_2 + 2\ e^- \quad (40)$$

The choice of removal pathways appears to be determined by the

acidity of the gas stream. At low $SO_3$ concentrations, the removal follows the two electron path. At high $SO_3$ concentration, the removal is a simple acid-base reaction to form pyrosulfate. This forces the removal to the one electron pathway. Either removal pathway gives an overall cell reaction of

$$SO_2 + \tfrac{1}{2} O_2 \longleftrightarrows SO_3 \qquad (41)$$

Current efficiencies are plotted in Figure III-13. Note that for each applied current value, the 5% vanadia electrolyte outperforms the 1% electrolyte at the same temperature. Also, the 5% vanadia has a higher efficiency at 380° C than the 1% vanadia at 400° C.

The current efficiency is greater than 100% for three cases with -5mA applied: 1% $V_2O_5$ at 400° C; 5% $V_2O_5$ at 380° C; 5% $V_2O_5$ at 400° C. At these operating conditions, $SO_2$ is rapidly converted to $SO_3$ , creating a relatively high $SO_3$ gas concentration. It is probable that the removal mechanism changes to the one electron pathway. This has the effect of arithmetically doubling the current efficiency.

At -10 mA applied current, efficiencies are less than 100%. At this current level, $SO_x$ removal is increased and therefore $SO_3$ gas concentration is reduced. With the reduced $SO_3$ level, the mechanism shifts back to the two electron pathway.

The most impressive case, 10 mA at 400° C, shows that the cell is approaching the design criteria of 80% $SO_x$ removal. The 55.3% removal was limited by the applied current. Our cell experienced

gas crossover before we could complete the study to the 100% removal current limit (≈18 mA). We ran another study under similar conditions in order to duplicate the present findings and continue the study to a 100% removal current limit. We also investigated higher flow rates to determine the diffusional or oxidation limitations. These results are presented in a later section.

Our final interest in this study was to determine the effect of the reduced particle size on electrolyte retention. We can not conclusively show that the borosilicate particles are better than the MgO-based matrix. The cathodic polarization reached values of -0.75 V versus reference. The anodic polarization reached values greater than +1.0 V. There are several possible causes for this high polarization, one of which is a concentration potential. Another cause is the fact that the anode was in three pieces when installed and the area was somewhat reduced. Also, during the warmup period, inadvertent extreme voltages caused partial oxidation of the perovskite electrodes.

In summary, the results of this task show that $SO_x$ removal in the full cell follows the reaction stoichiometry found in the free electrolyte studies. Investigation of the use of a $SO_2$ pre-oxidation catalyst showed that 98% of influent $SO_x$ could be removed when a platinum-on-silica-gel catalyst is used. Without this catalyst, removal is limited to 66% with a 5 wt.% $V_2O_5$ electrolyte. This result proved that a pre-oxidation catalyst is required to meet the design. A commerical sulfuric acid catalyst has been identified for this use.

Table III-1: $SO_2$ Oxidation Test Results

| Support Material | Particle size | Pt. loading (%) | Temperature (°C) | Gas Flowrate (cc/min) | Conversion% |
|---|---|---|---|---|---|
| silica gel | 35-40 mesh | 0.5 | 400 | 50 | 70 |
| silica gel | 35-60 mesh | 0.5 | 450 | 50 | 70 |
| silica gel | 35-60 mesh | 0.5 | 450 | 100 | 60 |
| alumina beads | 3mm diameter | 0.2 | 450 | 50 | 75 |
| alumina beads | 3mm diameter | 0.2 | 400 | 50 | 70 |
| alumina beads | 3mm diameter | 0.2 | 400 | 100 | 65 |
| alumina | 30 mesh | 3.0 | 400 | 50 | 99 |
| alumina | 30 mesh | 3.0 | 400 | 100 | 99 |
| alumina | 30 mesh | 3.0 | 400 | 25 | 99 |

Table III-2: $SO_3$ Effluent Analysis: Comparison of Experimental and Theoretical pH values - Gas contacting water

| Gas Composition(%) | | Flow Rate (cc/min) | Sample Time (min) | Experimental pH | Calculated pH |
|---|---|---|---|---|---|
| $SO_2$ | $O_2$ | | | | |
| 0.3 | 3.0 | 10 | 2.5 | 4.21 | 4.21 |
| 0.3 | 3.0 | 20 | 2.5 | 3.93 | 3.91 |
| 0.3 | 2.0 | 40 | 2.5 | 3.63 | 3.61 |
| 0.3 | 3.0 | 10 | 5.0 | 3.92 | 3.91 |
| 0.3 | 3.0 | 20 | 5.0 | 3.64 | 3.61 |
| 0.15 | 1.5 | 20 | 2.5 | 4.22 | 4.21 |
| 0.15 | 1.5 | 40 | 2.5 | 3.92 | 3.91 |
| 0.15 | 1.5 | 20 | 5.0 | 3.94 | 3.91 |
| 0.075 | 0.75 | 40 | 2.5 | 4.23 | 4.21 |

*Each gas stream was contacted with 100 ml of distilled water, with the cell operating at 400°C without any electrolyte

Table III-3: $SO_3$ Effluent Analysis:- Condensate contacting water

| Gas Composition (%) $SO_2$ | Gas Composition (%) $O_2$ | Flow Rate (cc/min) | Sample Time (hr) | Experimental pH | Calculated pH | Calculated pH (Including Activity) |
|---|---|---|---|---|---|---|
| 0.3 | 3.0 | 10 | 12 | 1.90 | 1.75 | 1.88 |
| 0.3 | 3.0 | 10 | 28.5 | 1.60 | 1.38 | 1.57 |
| 0.3 | 3.0 | 10 | 16 | 1.79 | 1.63 | 1.78 |
| 0.3 | 3.0 | 20 | 12 | 1.64 | 1.45 | 1.62 |
| 0.15 | 1.5 | 10 | 12 | 2.15 | 2.05 | 2.14 |
| 0.15 | 1.5 | 10 | 8 | 2.30 | 2.23 | 2.30 |



* Condensate was collected in 100 ml of distilled water, with the cell operating at 400°C without any electrolyte

Table III-4: Deviation of pH from theory at low pH

| cc $H_2SO_4$ added | mole (H) added | Experimental pH | Calculated pH |
|---|---|---|---|
| 0.02 | .00075 | 3.13 | 3.13 |
| 0.05 | .00187 | 2.73 | 2.73 |
| 0.10 | .00373 | 2.47 | 2.43 |
| 0.20 | .00747 | 2.21 | 2.13 |
| 0.30 | .01120 | 2.05 | 1.95 |
| 0.40 | .01494 | 1.95 | 1.83 |
| 0.50 | .01867 | 1.86 | 1.73 |
| 1.00 | .03734 | 1.61 | 1.43 |



* Incremental additions of $H_2SO_4$ to 1000 ml of distilled water (done with micro-syringes)

Table III-5: $SO_x$ Removal with differing electrolyte compositions

| Gas Composition (%) | | | Sulfate Concentration(%) | Flow Rate (cc/min) | Contact Time (min) | pH | % Removal |
|---|---|---|---|---|---|---|---|
| $SO_2$ | $O_2$ | NO | | | | | |
| 0.3 | 3.0 | -- | 10.0 | 10 | 5 | 4.97 | > 99 |
| 0.3 | 3.0 | -- | 5.0 | 10 | 5 | 4.90 | > 98 |
| 0.3 | 3.0 | -- | 0.0 | 10 | 720 | 1.94 | > 10 |
| -- | -- | 0.09 | 10.0 | 20 | 20 | -- | 0 |

Table III-6: Operating Conditions for Figures III-5 through III-8

| Run # | Cell Temperature (°C) | Flow Rate (cc/min) | Current (mA) | $SO_2$ Outlet Conc. (mole %) | % Removal |
|---|---|---|---|---|---|
| 1 | 365 | 36.5 | 0 | 0.180 | 40.0 |
| | | | 5 | 0.200 | 34.0 |
| | | | 10 | 0.236 | 22.0 |
| 2 | 380 | 36.5 | 0 | 0.203 | 32.6 |
| | | | 5 | 0.220 | 26.9 |
| | | | 10 | 0.228 | 24.2 |
| 3 | 400 | 36.5 | 0 | 0.155 | 48.5 |
| | | | 5 | 0.145 | 51.8 |
| | | | 10 | 0.137 | 54.5 |
| | | | 15 | 0.130 | 56.8 |
| 4 | 445 | 55.0 | 0 | 0.180 | 40.2 |
| | | | 5 | 0.170 | 43.5 |
| | | | 10 | 0.154 | 48.8 |

Inlet Gas composition:
0.301 % $SO_2$, 3.00 % $O_2$, Balance $N_2$

Table III-7: Data for Figure III-10 through Figure III-12

| Temp., (°C) | % $V_2O_5$ | Current (mA) | $SO_2$ Removal (%) | Current Efficiency (%) |
|---|---|---|---|---|
| 365 | 1.0 | 0. | 41.5 | -- |
| | | 5. | 33.7 | 96. |
| | | 10. | 20.8 | 30. |
| | 5.0 | 0. | 33.6 | -- |
| | | 10. | 36.9 | 66. |
| 380 | 1.0 | 0. | 32.0 | -- |
| | | 5. | 26.2 | 76. |
| | | 10. | 25.1 | 36. |
| | 5.0 | 0. | 44.0 | -- |
| | | 5. | 44.2 | 161. |
| | | 10. | 47.0 | 84. |
| 400 | 1.0 | 0. | 48.6 | -- |
| | | 5. | 51.9 | 147. |
| | | 10. | 54.3 | 77. |
| | | 15. | 56.8 | 54. |
| | 5.0 | 0. | 49. | -- |
| | | 5. | 53. | 190. |
| | | 10. | 55.3 | 99. |

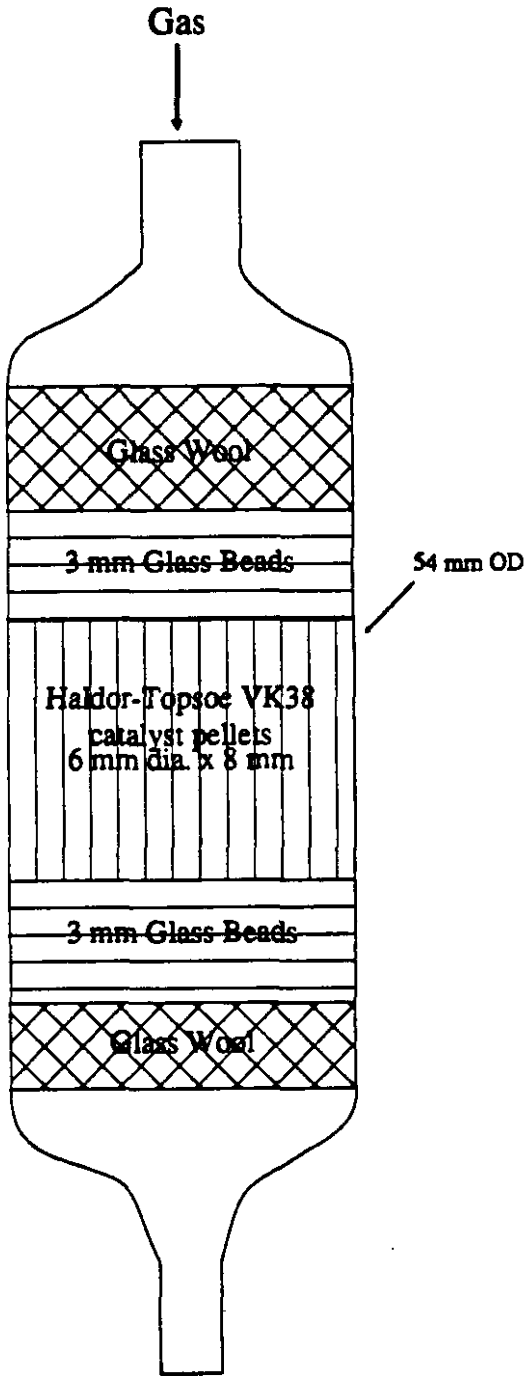


Figure III-1. Pre-Oxidation Reactor

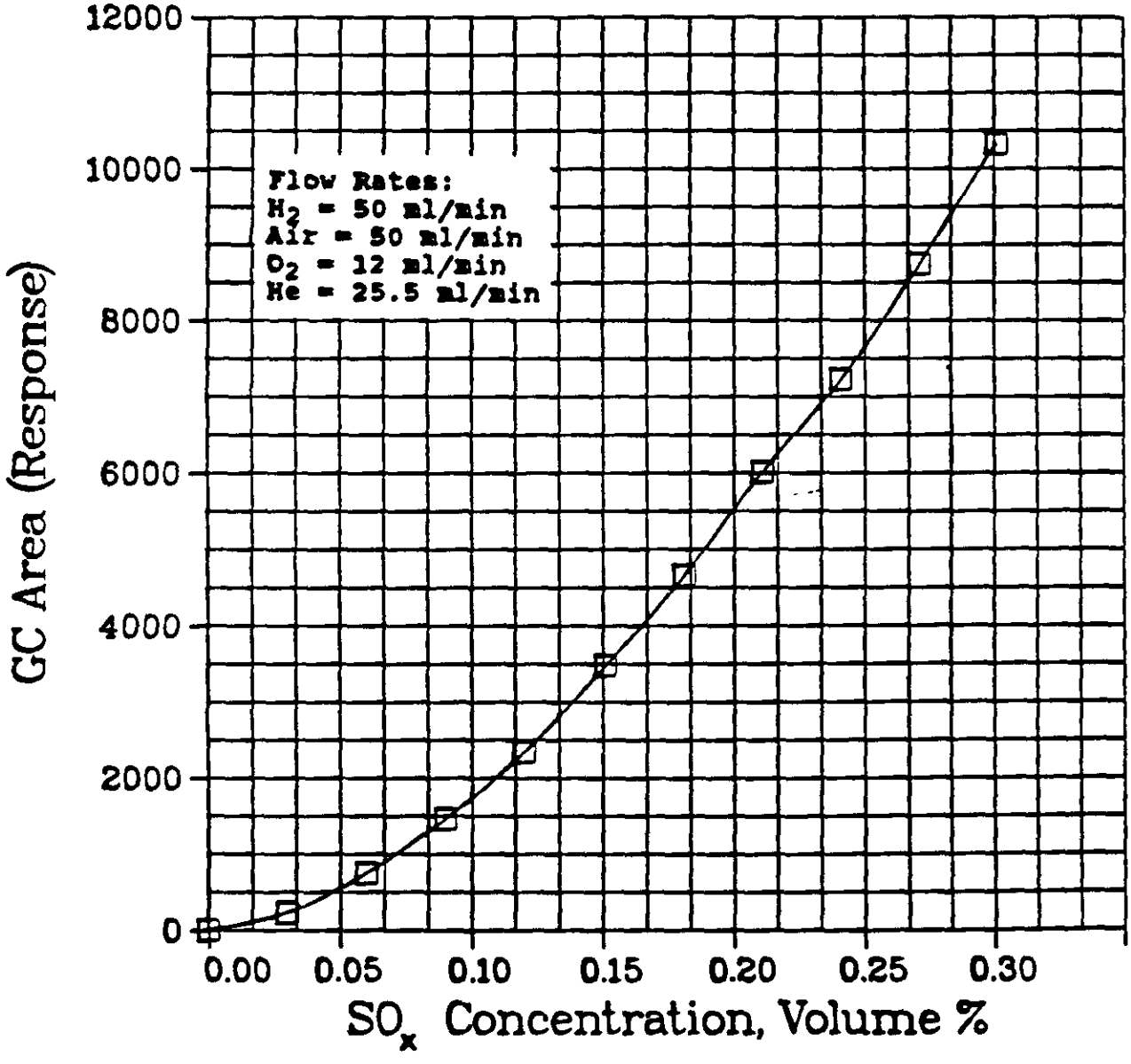


Figure III-2 Typical FPD Response Curve

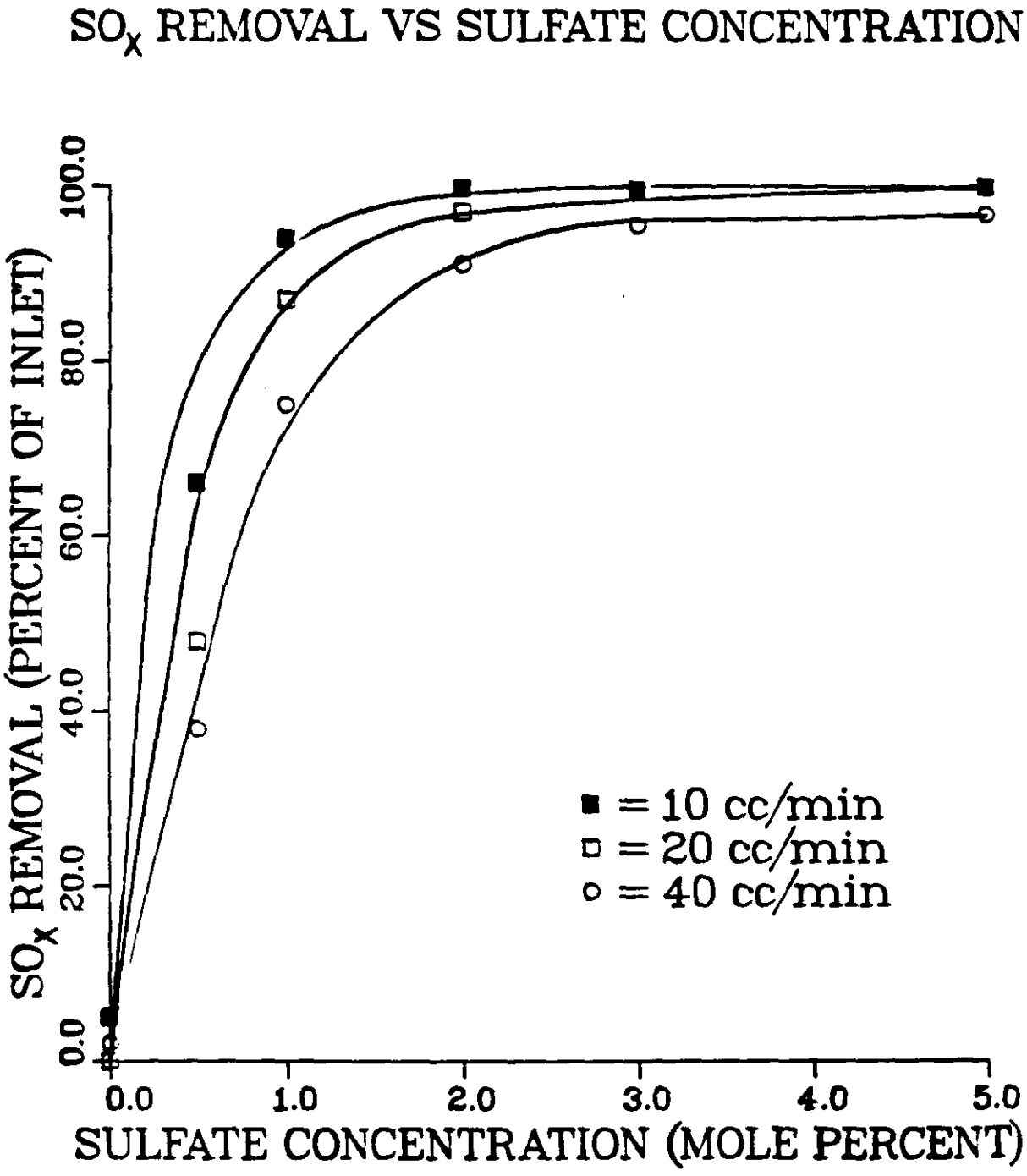


Figure III-3 $SO_x$ removal in free electrolyte, gas is 0.3% $SO_2$, 3.0% $O_2$ in $N_2$, all $SO_2$ is oxidized to $SO_3$ prior to entering cell, 400 C.

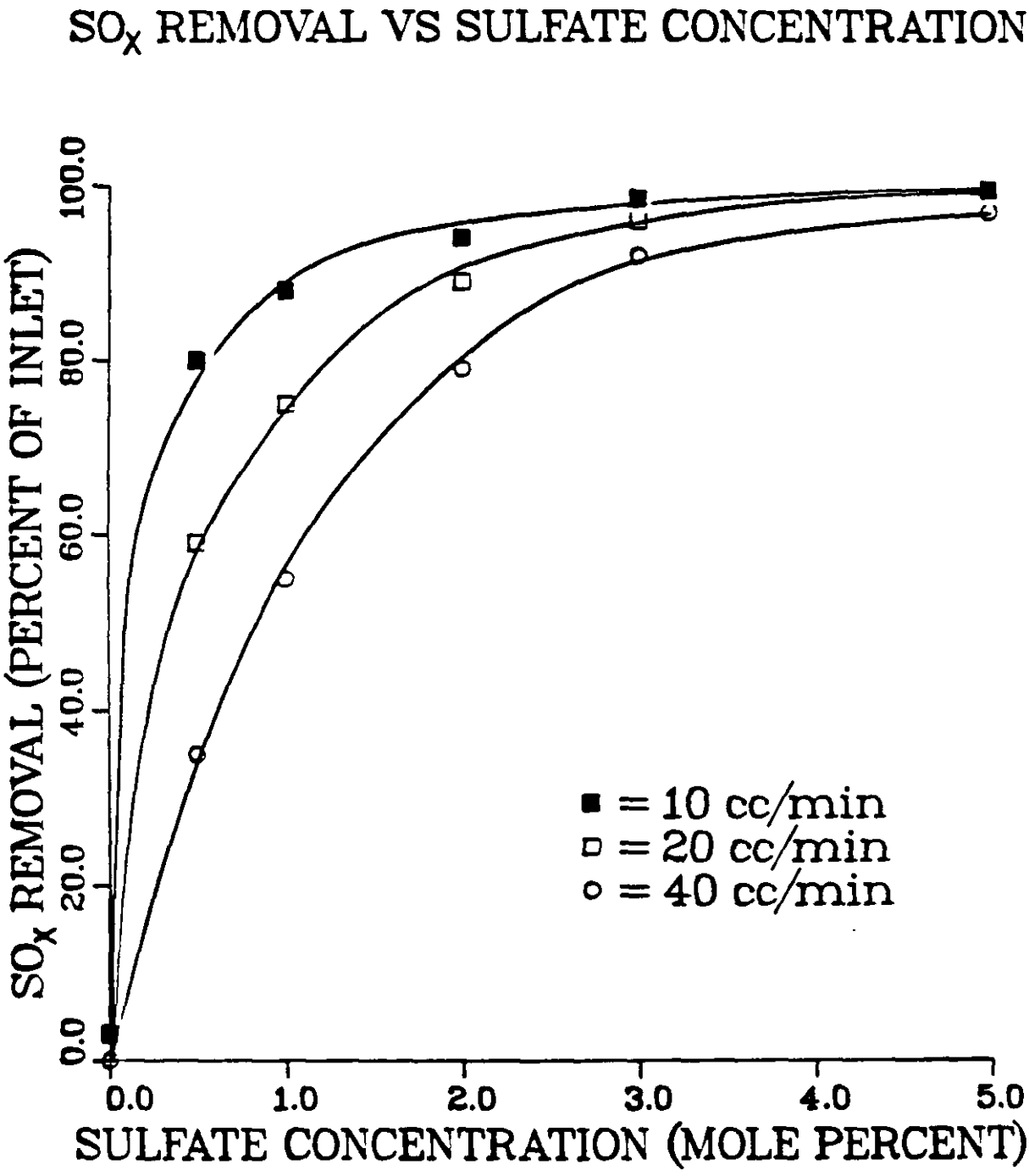


Figure III-4 $SO_x$ removal in free electrolyte, gas is 1.0% $SO_2$, 10.0% $O_2$ in $N_2$, all $SO_2$ is oxidized to $SO_3$ prior to entering the cell, 400 C.

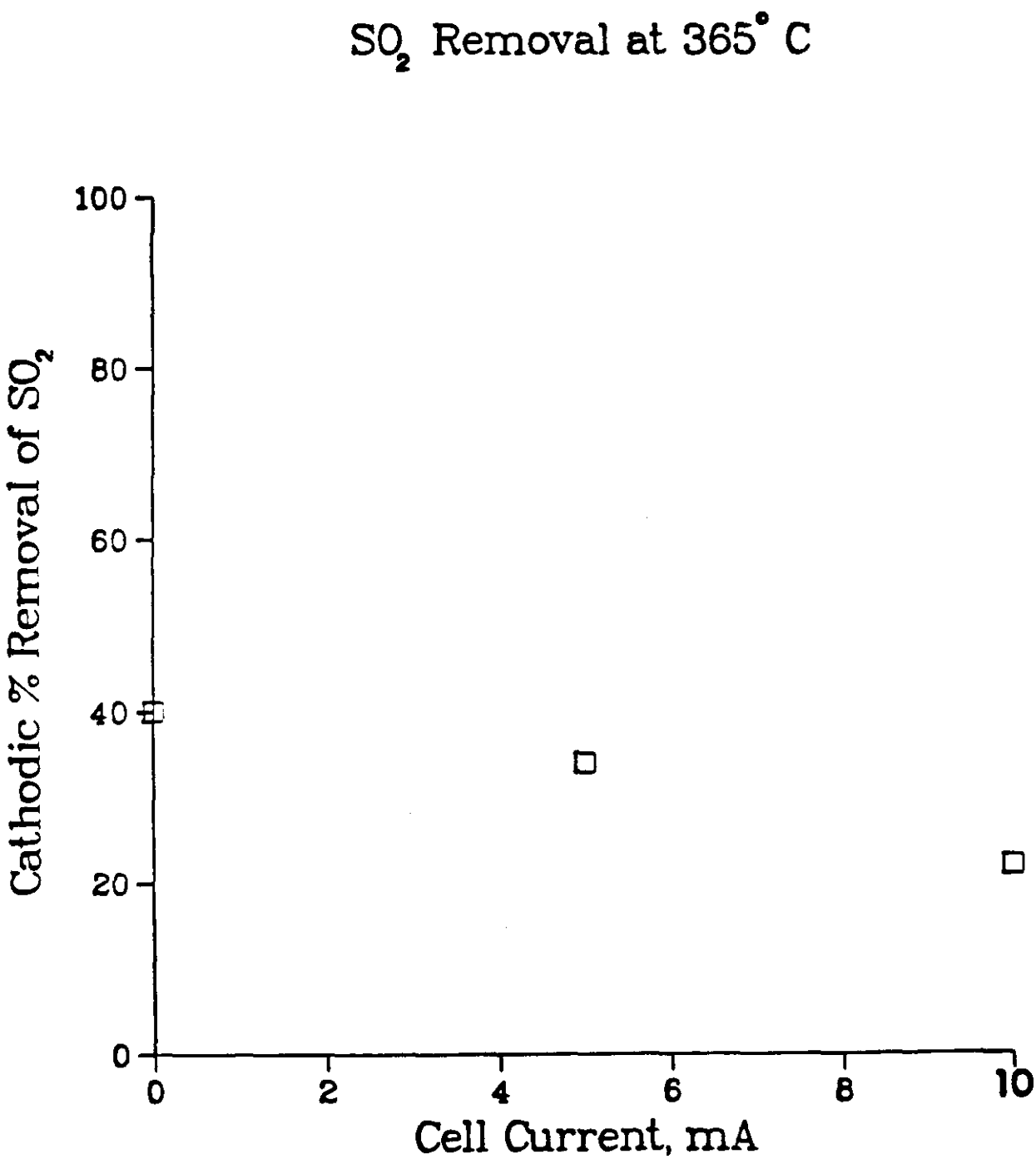


Figure III-5 $SO_2$ Removal at 365°C, 1 wt. % $V_2O_5$ No pre-oxidation catalyst

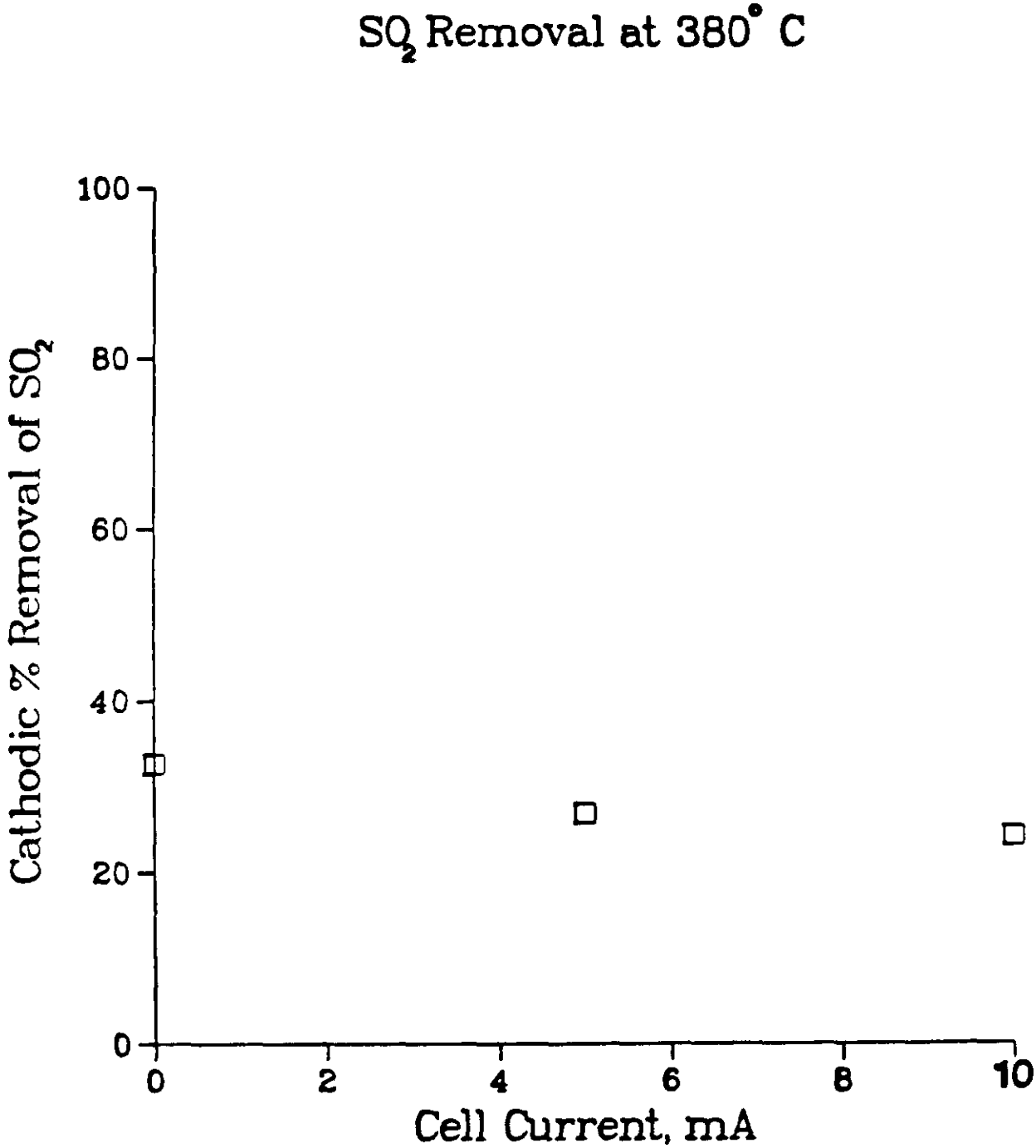


Figure III-6 $SO_2$ Removal at 380°, 1 wt. % $V_2O_5$, No pre-oxidation catalyst.

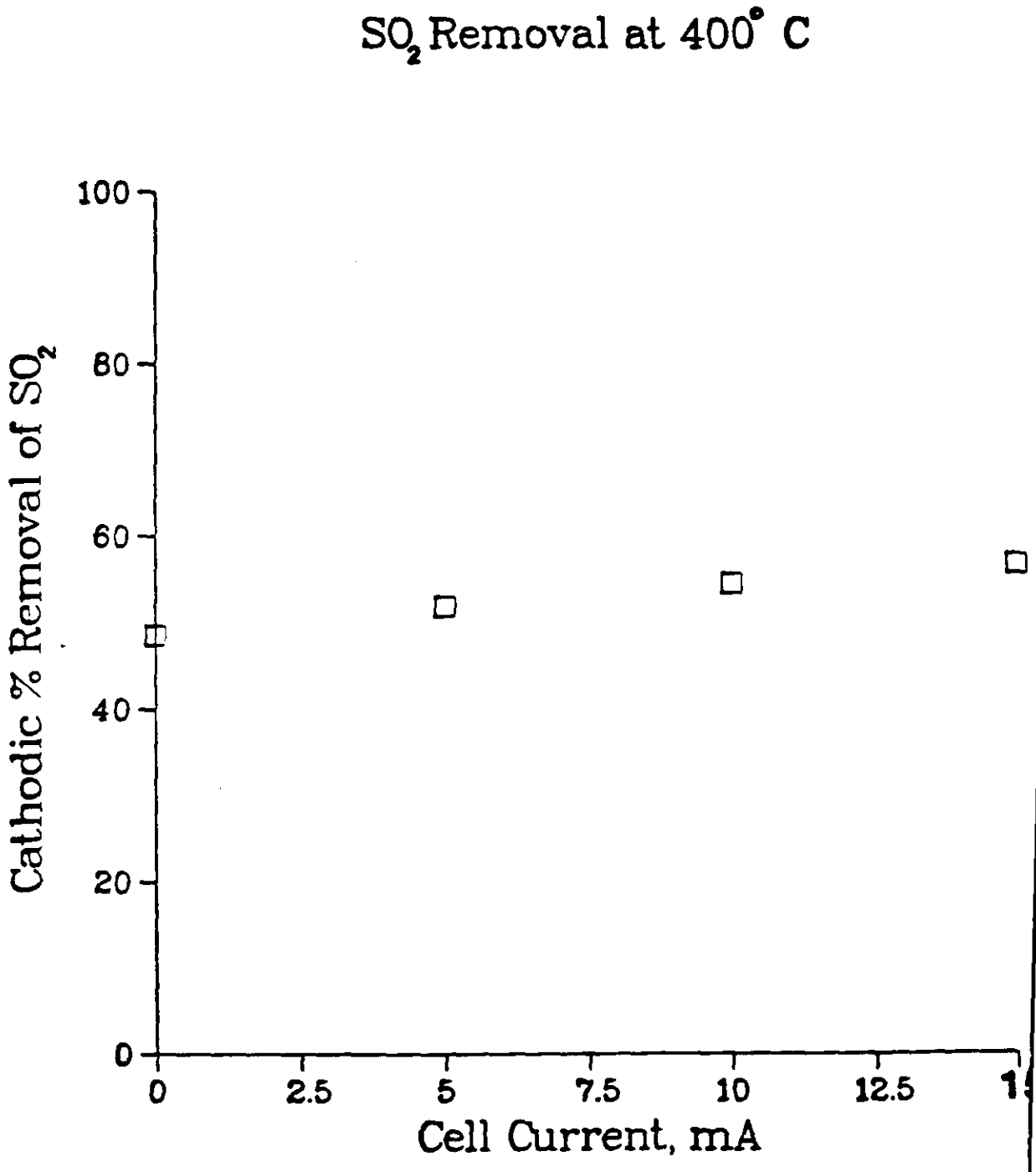


Figure III-7 $SO_2$ Removal at 400°C, 1 wt. of $V_2O_5$, no pre-oxidation catalyst

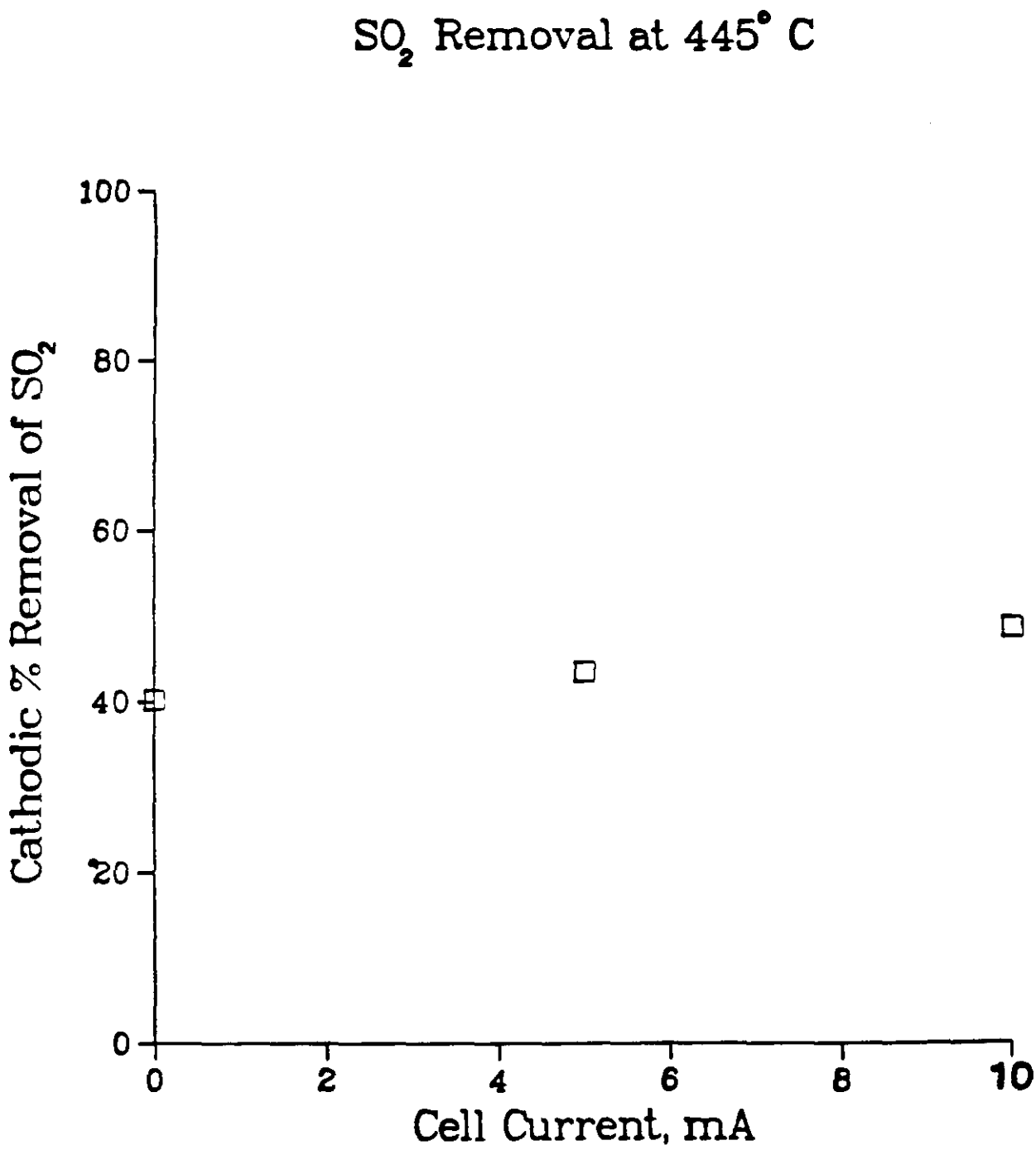


Figure III-8 $SO_2$ Removal at 445°C, 1 wt. of $V_2O_5$, No pre-oxidation catalyst

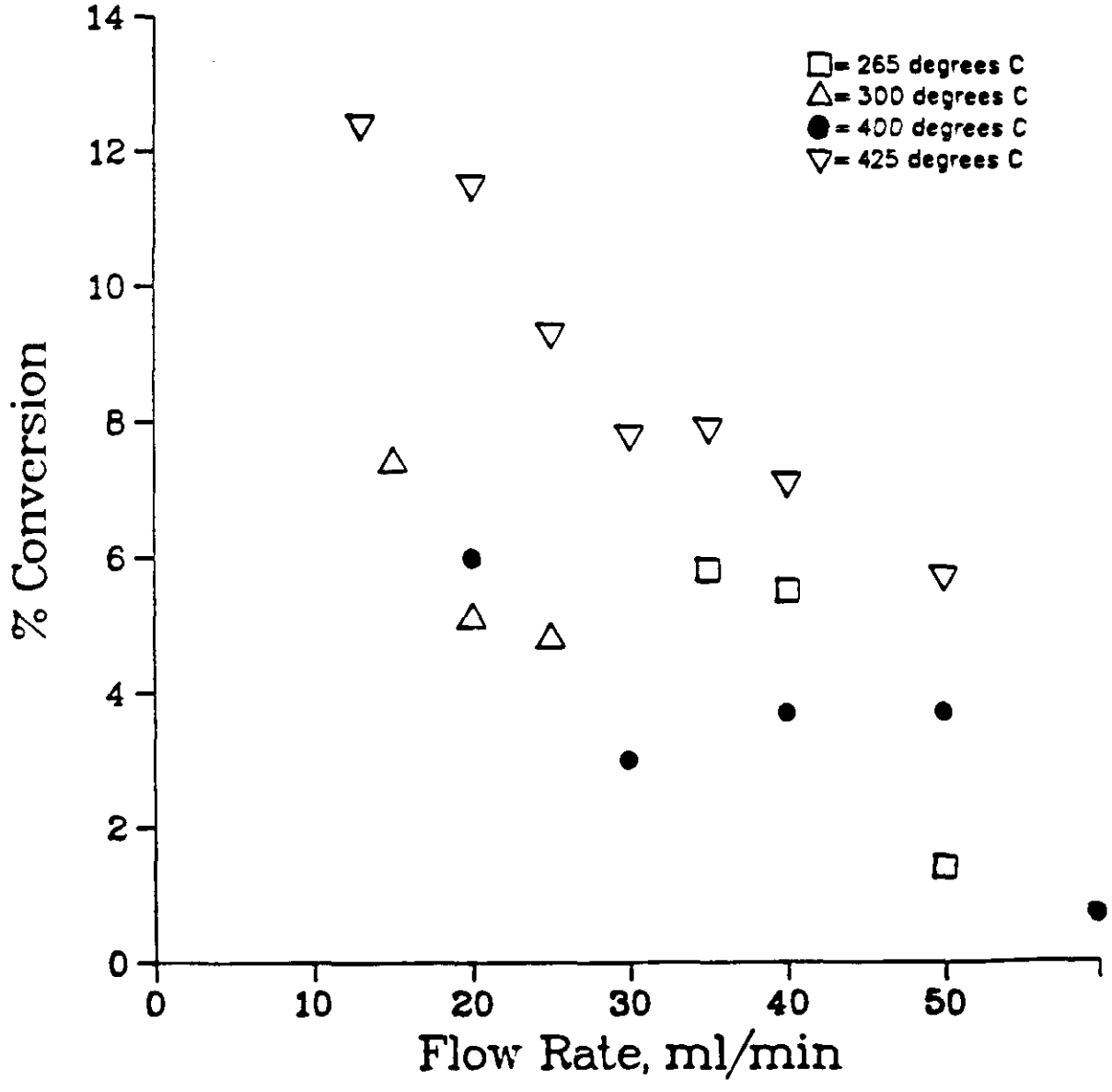


Figure III-9 Haldor-Topsoe VK38 Catalyst $SO_2$ Conversion

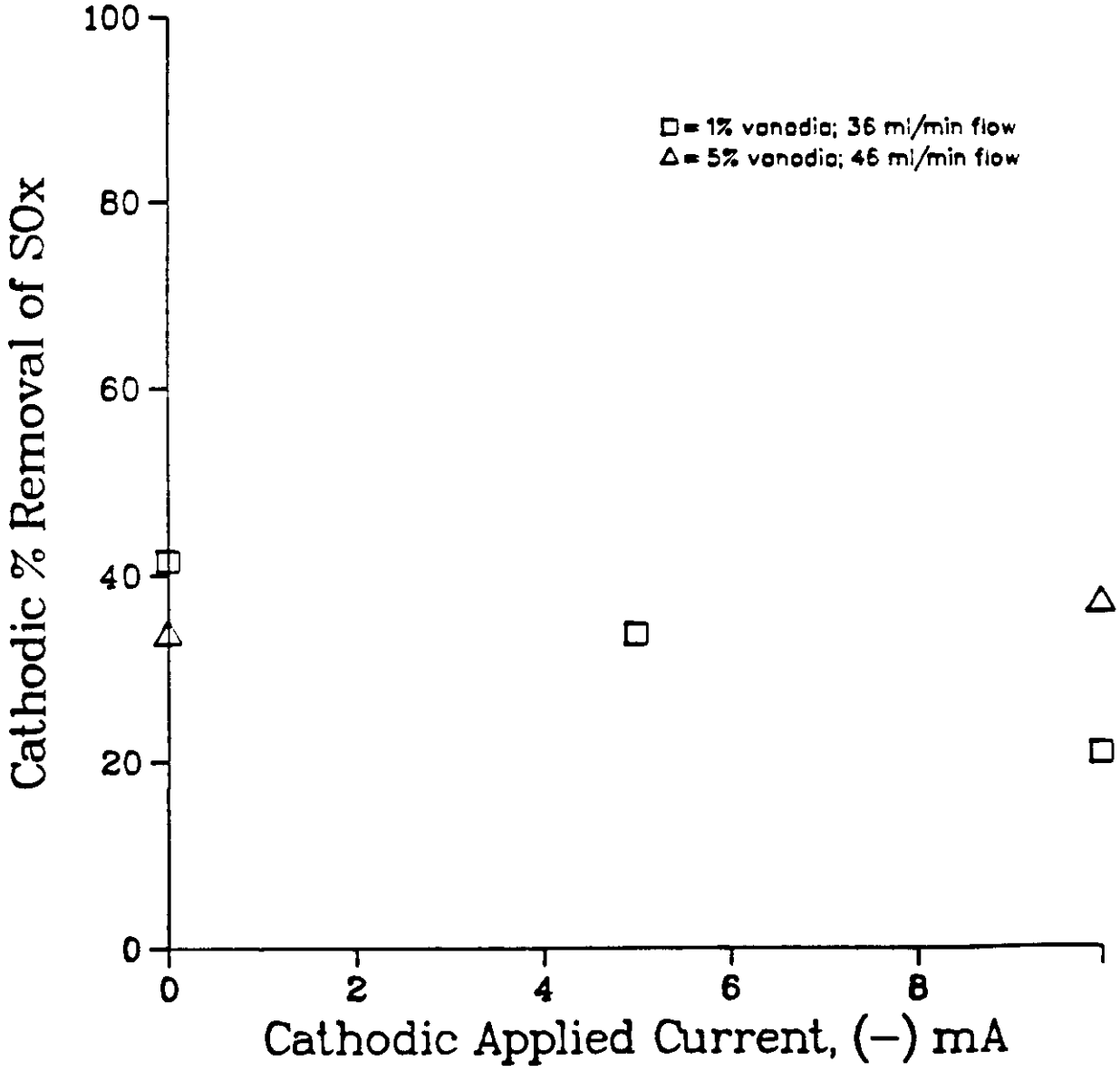


**Figure III-10** $SO_x$ **Removal at 365° C**

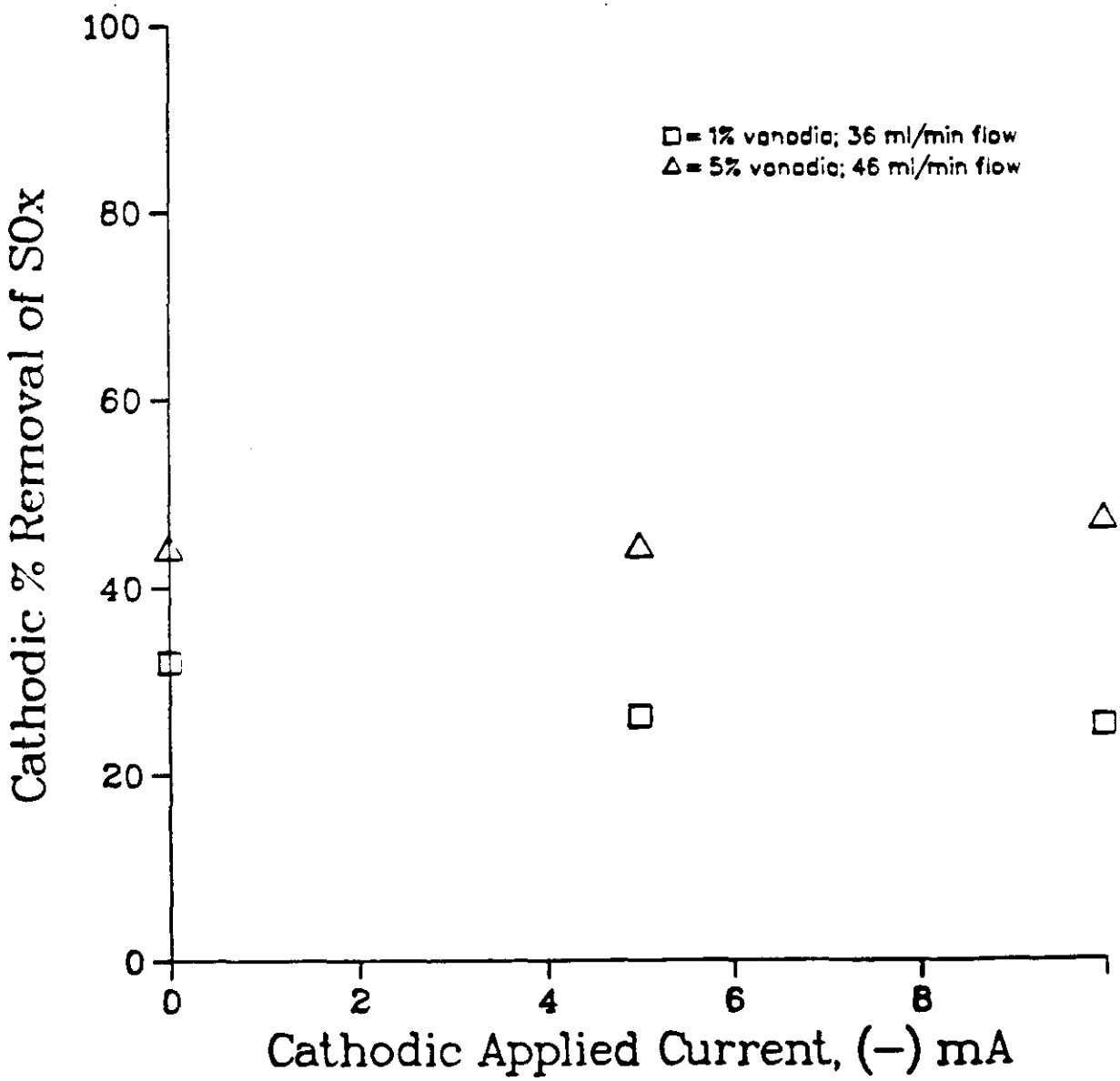


Figure III-11 $SO_2$ Removal at 380° C

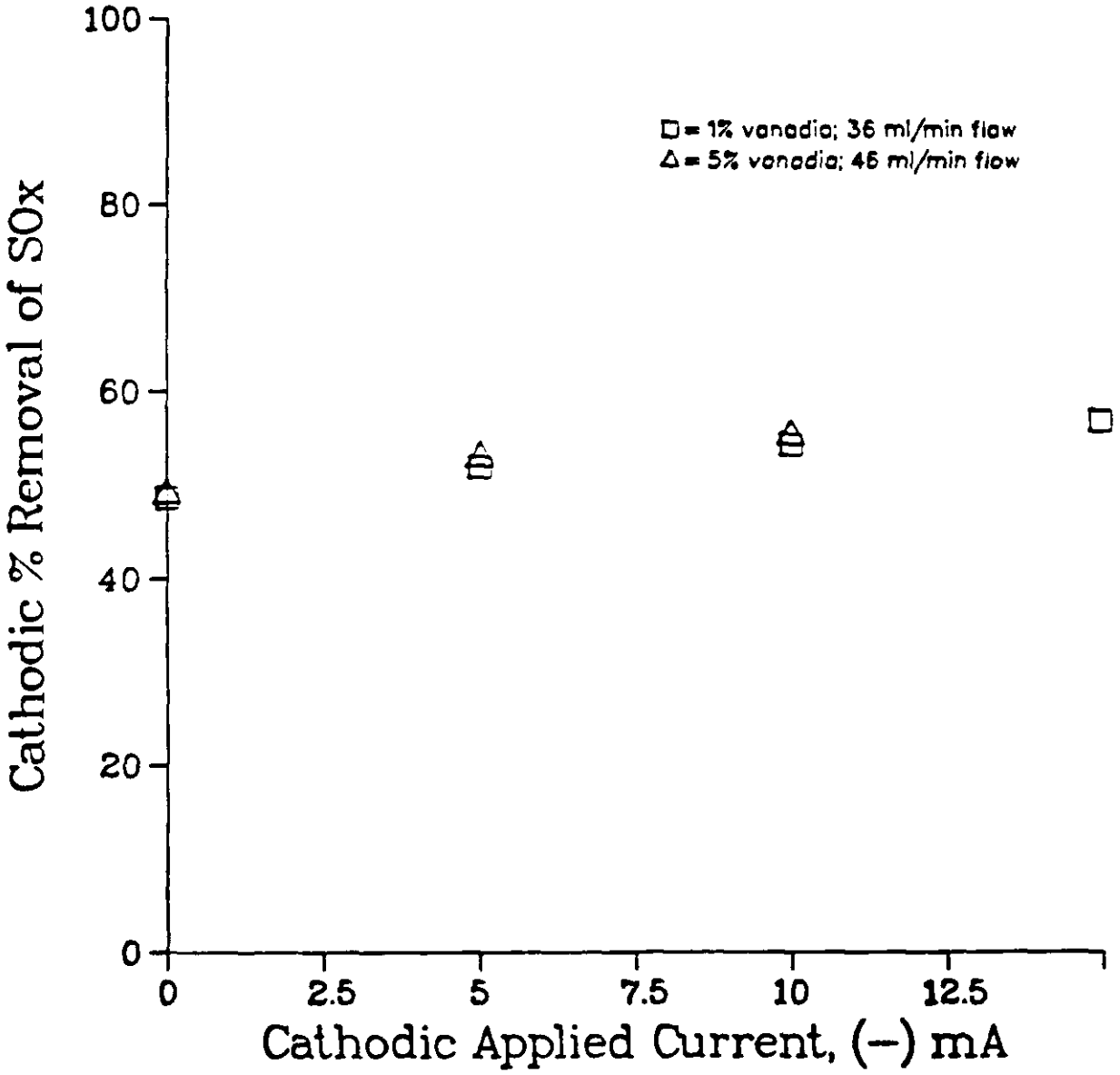


**Figure III-12 $SO_2$ Removal at 400° C**

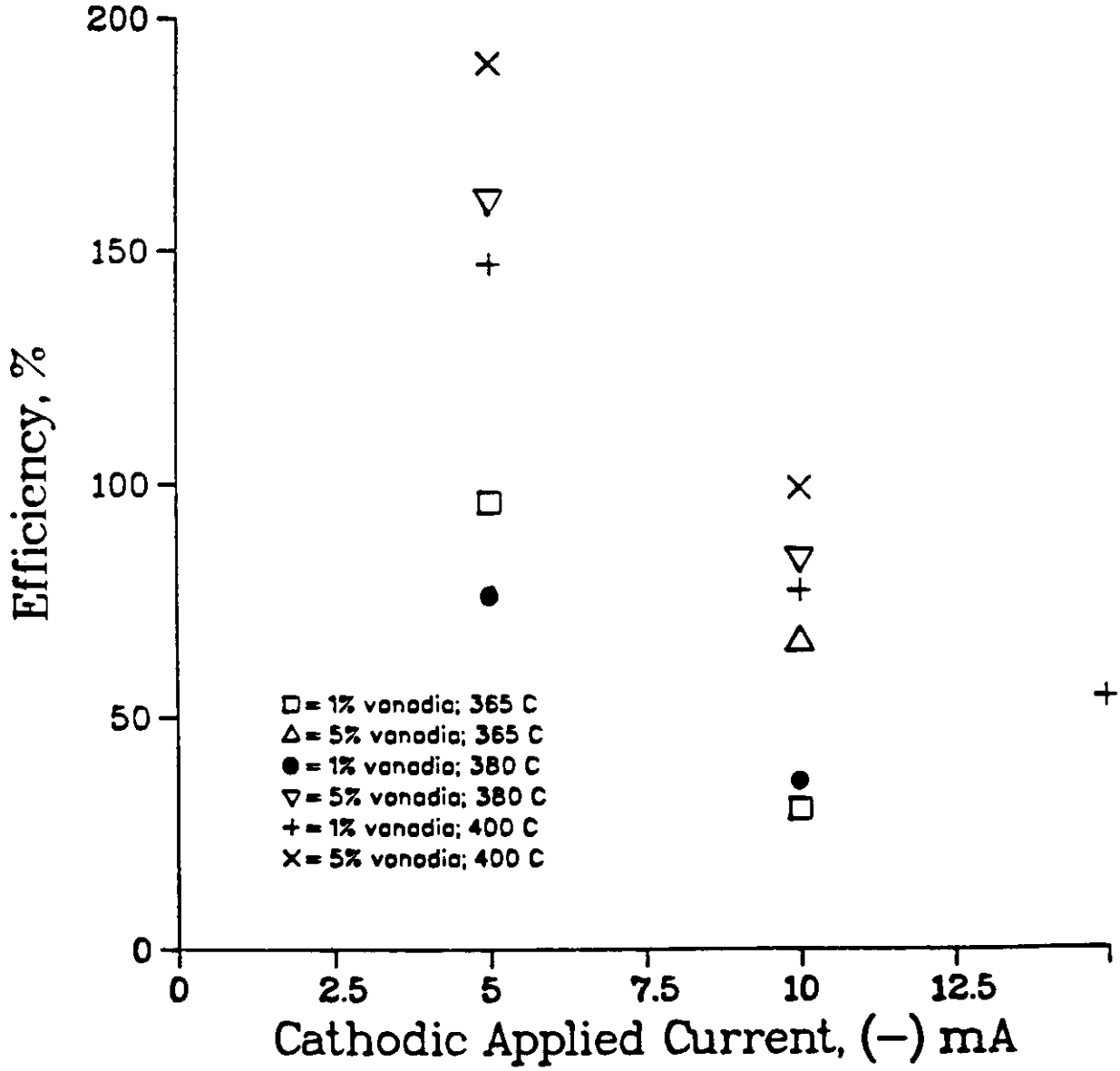


**Figure III-13 Cathodic Current Efficiency**

## IV. $NO_x$ Removal

### A. Free Electrolyte

Preliminary $NO_x$ tests showed significant removal of $NO_x$ through a $K_2S_2O_7/K_2SO_4/V_2O_5$ mechanism. The cell was constructed of pyrex and included three gas inlet/outlet tubes. Generally, the inlet gas was introduced to the cell through a tube containing provisions for a catalyst plug (platinized silica-gel) and bubbled through the electrolyte. The gas exited through one of the other tubes while the third was usually plugged. Teflon tubing was utilized for all connections due to its inertness to $SO_x$ and $NO_x$ gases. The cell schematic is presented in Figure IV-1.

Six different runs were conducted, each intended to help isolate an electrolyte component and determine its role in the $NO_x$ removal process. The first was a blank run, consisting of an empty cell held at 400°C. The blank run serves as a basis to compare all future runs. In the second and third runs powdered $K_2SO_4$ and $V_2O_5$ were added to the cell respectively. In the fourth run, the effect of platinized silica-gel was examined. This catalyst is often used in other cells to promote oxidation of $SO_2$. The fifth run examined $NO_x$ removal in the electrolyte (89% $K_2S_2O_7$, 10% $K_2SO_4$, 1% $V_2O_5$). The final run also examined $NO_x$ removal in electrolyte, but without any added sulfate (99% $K_2S_2O_7$, 1% $V_2O_5$).

Within each run six different gas environments were investigated. These were:

1. 530 ppm NO in $N_2$
2. 530 ppm NO in $N_2$ plus 20 cc/min air
3. 530 ppm NO in $N_2$ plus 20 cc/min (1% $SO_2$, 10% $O_2$ in $N_2$)
4. 565 ppm $NO_2$ in $N_2$

5. 565 ppm $NO_2$ in $N_2$ plus 20 cc/min air
6. 565 ppm $NO_2$ in $N_2$ plus 20 cc/min (1% $SO_2$, 10% $O_2$ in $N_2$)

Thus, gas environments 1-3 examine NO removal and the effect of $O_2$ and $SO_2$. Similarly, gas environments 4-6 examine $NO_2$ removal and effect of $O_2$ and $SO_2$.

Two equilibria will influence the composition of test gases exiting the removal cell. The first equilibrium involves NO, $O_2$ and $NO_2$:

$$NO + 1/2\ O_2 \quad \overset{K_1}{<=>} \quad NO_2 \qquad (42)$$

where the equilibrium constant, $K_1$, is 3.55 at 400°C.[4] Although the oxidation is favored thermodynamically, the kinetics are very slow without a promoter. The other equilibrium involves a redox reaction between NO, $NO_2$, $SO_2$ and $SO_3$:

$$NO_2 + SO_2 \quad \overset{K_2}{<=>} \quad NO + SO_3 \qquad (43)$$

where nitrogen is reduced from the +4 state to the +2 state and sulfur is oxidized from the +4 state to the +6 state. The equilibrium constant, $K_2$, is 167 at 400°C. The value of $K_1$ is calculated and reported in the data tables where possible (It cannot be determined for gas 1 because no $O_2$ is in the system). The effect of $K_2$ is described qualitatively in the discussions which follow but cannot actually be calculated because of the lack of information on $SO_2$ and $SO_3$ concentrations.

---

[4]Smith, J.M. and Van Ness, H.C., Introduction to Chemical Engineering Thermodynamics, 3rd Ed., McGraw-Hill, NY, 1975.

Table IV-1 gives the data generated from the blank run. The results of gases 1-3 show that NO is unaffected by additions of $O_2$ and $SO_2$. The added streams containing these components served only to dilute the NO base gas and did not chemically interact to any measurable extent. The addition of $O_2$ did not oxidize the NO as in equation (42), indicating the kinetics are extremely slow without a catalyst. The $NO_2$ based gas streams showed definite chemical changes going through the cell. The results of gases 4 and 5 show that $NO_2$ dissociates as in equation (42). However, the dissociation is slow and equilibrium is not achieved even at the lowest flow rates as indicated by the $K_1$ values. The results for gas 6 show the strong reducing powers of $SO_2$ on $NO_2$, as in equation (43). At the lowest flow rates the $NO_2$ is almost completely reduced to NO, shifting the calculated value of $K_1$ below the equilibrium value. This indicates equilibrium reaction (43) influences the gas composition when $SO_2$ is present.

Table IV-2 displays the data generated when powdered sulfate ($K_2SO_4$) was added to the cell. This data is virtually identical to that in Table IV-1. Thus, sulfate did not influence either equilibrium, nor did it promote any $NO_x$ removal. Although solid potassium sulfate appears inert to both NO and $NO_2$, sulfate ions will also exist in electrolyte. The possibility of sulfate ion being involved in the removal process is explored later.

Table IV-3 shows the results when vanadia powder is added to the cell. Like potassium sulfate, vanadia does not promote any $NO_x$ removal. However, vanadia does possess catalytic activity,

resulting in a shift in the $NO_2/NO$ ratio closer to equilibrium as indicated by the $K_1$ values. Streams 2 and 5 are virtually at equilibrium while streams 3 and 6 have calculated $K_1$ values slightly below the equilibrium value due to the added reducing power of $SO_2$.

Table IV-4 exhibits the removal results when platinized silica gel is incorporated in the cell. Platinized silica gel catalyzes the oxidation of $SO_2$ to $SO_3$. Two effects of the catalyst are apparent. First, the $K_1$ values are all very close to the theoretical value, indicating platinized silica gel is a good promoter of equation (42). Second, significant $NO_x$ removal occurs when $SO_3$ is added to either NO or $NO_2$ base gas. The results indicate $NO_2$ is the component which is actually being removed. However, in excess $SO_3$, NO is oxidized to $NO_2$ as in equation (43), and is therefor indirectly removed.

Several possibilities exist as to the actual removal mechanism. One possibility is the gas phase reaction between $SO_3$ and $NO_2$ in the cell. The reaction could be either a $SO_3$ catalyzed decomposition of $NO_2$ to $N_2$ and $O_2$, or an association reaction producing some type of sulfur-nitrogen-oxide. Another possibility is an interaction between $NO_2$ and condensed $SO_3$ in the outlet tubes from the cell to the $NO_x$ analyzer. This interaction could be either a reaction or simple absorption.

Additional experimentation indicates $NO_2$ absorption in condensed $SO_3$ is the true removal mechanism. For example, cleaning the connecting tubing between the cell and the analyzer (thus

removing condensed $SO_3$) resulted in a change in $NO_x$ removal from 84% to 12% in one test. A permanent cell tube protruding about six inches from the furnace contained condensed $SO_3$ and could not be cleaned. This residual $SO_3$ could account for the 12% removal subsequent to cleaning. Continued operation of the cell resulted in a gradual increase in $NO_x$ removal as $SO_3$ visibly condensed on the cleaned tube walls. During tube cleaning, an orange-brown gas cloud emerged from the tube. This is indicative of $NO_2$ and further substantiates the absorption mechanism.

Table IV-5 displays the $NO_x$ removal data when the cell is charged with a high sulfate electrolyte (89% $K_2S_2O_7$, 10% $K_2SO_4$, 1% $V_2O_5$). An important property of sulfate is its high affinity for $SO_3$. Thus, sulfate acts to absorb any free $SO_3$ within the electrolyte and virtually no $SO_3$ leaves the cell with the exiting gas stream. As a consequence, no $SO_3$ was observed condensing in the connecting tubes, and no $NO_x$ removal was achieved.

Table IV-6 also exhibits $NO_x$ removal data for an electrolyte charged cell, but no sulfate was added (99% $K_2S_2O_7$, 1% $V_2O_5$) for these tests. Because pyrosulfate dissociates according to the equilibrium ($K_{eq} = 2 \times 10^{-6}$ at 400°C):

$$S_2O_7^{2-} \rightarrow SO_4^{2-} + SO_3 \qquad (44)$$

and no sulfate was added to counter the equilibrium, some free $SO_3$ is contained in the electrolyte. Gases passing through the system gradually picked up the free $SO_3$ and carried it out of the cell where $SO_3$ once again was observed condensing inside the connecting tubing. The condensed $SO_3$ provided a NO oxidizer and $NO_2$ absorbent,

resulting in good removal results for all gases tested. Generally 80 to 90 percent $NO_x$ removal could easily be achieved at lower flow rates.

The test which most closely resembles a true flue gas (composition-wise), is gas 3 at a total flow rate of 40 cc/min. The inlet composition in this test was 0.028% NO, 0.50% $SO_2$, 5.0% $O_2$, 7.5% $CO_2$ with the balance $N_2$. In this test 75% $NO_x$ removal was achieved, limited only by mass transfer.

The $NO_x$ removal mechanism thus seems to involve an interaction between $NO_2$ and $SO_3$. The evidence suggests the interaction is $NO_2$ absorption in condensed $SO_3$ in the outlet tubes of the cell. No interactions between $NO_x$ and $K_2S_2O_7$, $K_2SO_4$ or $V_2O_5$ were observed.

B. <u>$NO_x$ Removal: Full Cell</u>

Our standard membrane cell was assembled from the following components. The porous, gas-diffusion electrodes are made from a perovskite-type compound, $La_{0.8}Sr_{0.2}CoO_3$ using the optimized technique in Section I. The electrolyte membrane was made from equal weights of borosilicate glass matrix particles and electrolyte. The electrolyte was a mixture of 95 wt% $K_2S_2O_7$, 5 wt% $V_2O_5$. A schematic of this arrangement, including the overall $SO_2$ removal chemistry, is presented in Figure IV-2. The MACOR housings are excluded from the drawing for clarity.

A stream of 0.3% $SO_2$, 3% $O_2$ and $N_2$ was fed to the cathode of the removal cell during all studies, as required by the $SO_2$ removal chemistry. During startup, a similar gas stream was used at the

anode. After the cell stabilized, the working electrode's gas stream was augmented with NO, available at 893 ppm in $N_2$. This may be further diluted by the other gas streams. Details of the experiments are given below.

The electrode under investigation is herein called the working electrode. This is a cathode when reducing (negative) current is applied and an anode under oxidizing (positive) current. The following runs used both types of current.

Figure IV-3 shows that NO is removed from the gas stream with current (+10 mA) at the working electrode. A small quantity of $NO_2$ is generated with applied current. This is to be expected on account of the following reaction:

$$NO + 1/2\ O_2 \ <==>\ NO_2 \qquad (42)$$

whose equilibrium constant is $K_1 = 3.55$ at 400° C.

When oxygen is absent, reaction (42) moves to equilibrium and the $NO_2$ level approaches zero. When $O_2$ is added, its partial pressure is many times greater than NO and $NO_2$ and the reaction moves far to the right. At 400° C, the kinetics of this reaction should limit the approach to equilibrium. No attempt was made to determine if this occurs without applied current.

Figure IV-4 depicts another run where nitric oxide is supplied to the working electrode, at 425° C. At time zero, only NO and $N_2$ flow to the electrode. A small decrease in NO concentration occurs with oxidizing current. When $O_2$ is added to this gas, the $NO_x$ levels drop to near zero. Increasing the NO flow rate has a minimal effect on the outlet $NO_x$ concentration. When the current is removed, the

gas concentrations increase. When the oxygen is shut off, the gas phase concentrations rapidly rise. This shows that $NO_x$ removal is strongly dependent on $O_2$ level. When reducing current (-10 mA) is applied, the $NO_x$ levels increase to the starting value.

In the $SO_2$ removal cell, the flue gas passes over the cathode where the $SO_2$ is selectively removed. To keep the $SO_x/NO_x$ design the same, it was necessary to investigate the use of current for NO removal in different gas atmospheres. Figure IV-5 displays the results of applying reducing current with different gas atmospheres at 425° C. At the start, the $SO_2/O_2/N_2$ simulated flue gas and the NO mix (893 ppm) enter the cell. When the reducing current (-10 mA) is started, the NO level increases slightly - removal is hindered. The $SO_2$ mix was then replaced with pure oxygen. Immediately the $NO_x$ level increases, showing that NO is oxidized to $NO_2$. The $NO_x$ level shown includes NO. However, the total $NO_x$ increases from the starting point. Apparently the $O_2$ is reacting with adsorbed $N_2$ from either previously decomposed NO or gaseous nitrogen.

When the oxygen is shut off, the NO and $NO_x$ levels return to their previous values. Adding the $SO_2/O_2/N_2$ simulated flue gas appears to push the $NO_x$ levels higher, but they soon return to the starting level. This action can not be explained yet. Water was added to the gas stream and may account for some of this behavior.

The oxidizing current removal mechanism is unknown. It is possible that the NO is being removed by contributing to the oxidation of $SO_2$, via:

$$SO_2 + NO \text{ <==> } SO_3 + 1/2\ N_2 \qquad (45)$$

with

$K_{eq} = 3.5 \times 10^{8}$ at 700K [5]

with the assistance of the $V_2O_5$ catalyst in the electrolyte.

C. Possible Mechanisms

At least four possibilities exist as $NO_x$ removal mechanisms.

1) the $NO_x$ may combine with $SO_x$, through a reaction mechanism similar to the chamber process for sulfuric acid production.

2) the $SO_2$ may act as a reductant for NO in the presence of $V_2O_5$.

3) the $NO_x$ may be removed through a reduction pathway using electrochemically produced oxygen atoms; and

4) removal of $NO_x$ via oxidation and combination with water to produce nitric acid.

The four possible mechanism are described below.

1. $NO_x$ removal through $S_xN_yO_z$ formation.

Before invention of the contact process, sulfuric acid was made commercially by the chamber process[6]. In the chamber process, sulfur dioxide reacts with air, oxides of nitrogen and water. The oxides of nitrogen transfer oxygen in the air to the sulfur dioxide so that it forms sulfur trioxide, at the same time acquiring water to form sulfuric acid. The chamber process operates at atmospheric pressure and 111° C.

The oxides of nitrogen are not consumed in the production of

---

[5] JANAF Thermochemical Tables, Third Ed., ACS, 1985.

[6] Riegel's Industrial Chemistry, J. A. Kent, ed., Reinhold, New York, 1962, p. 67.

sulfuric acid; rather they are catalytic in nature. The reaction pathway is given below.

$$H_2O + SO_3 + NO \rightarrow [H_2SO_4]NO \quad (46)$$

$$2\ SO_5NH + SO_2 + 2\ H_2O \rightarrow 2\ [H_2SO_4]NO + H_2SO_4\ (\ell) \quad (47)$$

$$2\ [H_2SO_4]NO + NO_2 \rightarrow 2\ SO_5NH + H_2O + NO \quad (48)$$

$$NO + 1/2\ O_2 \rightarrow NO_2 \quad (42)$$

$[H_2SO_4]NO$ is known as violet acid; $SO_5NH$ is nitrosyl sulfuric acid. These intermediates are recycled back to the chambers in the commercial process.

In our flow-through process, these intermediates are not recycled. If water vapor is present, this mechanism is a possibility for the observed removal of $NO_x$. The reactions may be enhanced by the electrode surface and the higher operating temperature.

2. $SO_2$ as reductant for NO on $V_2O_5$.

The ideal NO removal mechanism for the $SO_x/NO_x$ removal cell is for $SO_2$ to act as a reductant for NO. The simple reaction is

$$SO_2 + NO \rightarrow SO_3 + 1/2\ N_2 \quad (45)$$

$$K_{eq} = 3.5 \times 10^8 \text{ at } 700\ K$$

These other possibilities are present:

$$SO_2 + NO_2 \rightarrow SO_3 + NO \quad (43)$$

$$NO + 1/2\ O_2 \leftrightarrow NO_2 \quad (42)$$

Also, the $SO_3$ present at the anode may act as a catalyst for the decomposition of NO. $SO_3$ condenses in the outlet tubes of the cell and is responsible for a low level of removal. This residual removal is discriminated from that due to current when the current

is removed.

3. $NO_x$ reduction mechanism.

During combustion of fossil fuels, $NO_x$ is formed through reaction of atomic oxygen with molecular nitrogen in the air[7]. The mechanism is a homogeneous, gas-phase, free radical chain reaction,

$$O + N_2 == NO + N \quad (49)$$

$$N + O_2 == NO + O \quad (50)$$

In our removal cell, atomic oxygen is generated at the anode as part of the $SO_2$ removal mechanism. This electro-oxidatively generated oxygen will not desorb directly. However, many reactants are present which may react with this oxygen. A proposed mechanism is given.

$$SO_4^{2-} == SO_3 + O_{ad} + 2\ e^- \quad (51)$$

$$O_{ad} + NO == O_2 + N_{ad} \quad (52)$$

$$N_{ad} + NO == N_2 + O_{ad} \quad (53)$$

With these competing reactions:

$$2\ O_{ad} == O_2 \quad (54)$$

$$O_{ad} + SO_2 == SO_3 \quad (55)$$

$$O_{ad} + N_{ad} == NO \quad (56)$$

$$N_{ad} + N_{ad} == N_2 \quad (57)$$

This mechanism can account for the dependence of removal with current.

4. Oxidation of NO to $HNO_3$

In an oxidizing environment, the oxidation of $NO_x$ is highly

---

[7]Y. B. Zeldovich, Acta Physicochim., USSR 21 (1946), p.557

probable. This mechanism would consist of the following reactions:

$$NO + O_{ad} == NO_2 \quad (58)$$

$$NO_2 + O_{ad} == NO_3 \quad (59)$$

$$NO_2 + NO_3 == N_2O_5 \quad (60)$$

$$N_2O_5 + H_2O == 2\ HNO_3 \quad (61)$$

The chemiluminescent $NO_x$ analyzer will identify NO and $NO_2$. Its ability to detect other $NO_x$ species is unknown. If this mechanism is followed in the observed removal, the products may not be detected. This mechanism is easily manipulated via the water content.

Table IV-1: $NO_x$ Removal in Blank Cell

| Gas | Flow Rate (cc/min) | Outlet Concentrations NO (ppm) | $NO_2$ (ppm) | $K_1$ | $NO_x$ Removal (Percent) |
|---|---|---|---|---|---|
| 1 | 80 | 539 | 0 | - | --- |
| | 40 | 529 | 0 | - | --- |
| | 20 | 525 | 0 | - | --- |
| | 10 | 519 | 0 | - | --- |
| 2 | 100 | 435 | 0 | 0 | --- |
| | 60 | 350 | 0 | 0 | --- |
| | 40 | 260 | 0 | 0 | --- |
| | 30 | 175 | 0 | 0 | --- |
| 3 | 100 | 435 | 0 | 0 | --- |
| | 60 | 354 | 0 | 0 | --- |
| | 40 | 264 | 0 | 0 | --- |
| | 30 | 175 | 0 | 0 | --- |
| 4 | 80 | 33 | 537 | 4006 | --- |
| | 40 | 54 | 510 | 1817 | --- |
| | 20 | 76 | 480 | 1024 | --- |
| | 10 | 93 | 460 | 725 | --- |
| 5 | 100 | 22 | 430 | 95 | --- |
| | 60 | 25 | 350 | 53 | --- |
| | 40 | 25 | 240 | 30 | --- |
| | 30 | 24 | 160 | 18 | --- |
| 6 | 100 | 37 | 428 | 82 | --- |
| | 60 | 138 | 239 | 9.5 | --- |
| | 40 | 204 | 77 | 1.7 | --- |
| | 30 | 180 | 6 | 0.1 | --- |

Blank run with empty cell, 400°C, gases are: 1) NO in $N_2$: 2) NO in $N_2$ plus 200 cc/min air; 3) NO in $N_2$ plus 20 cc/min (1.0% $SO_2$, 10.0% $O_2$ in $N_2$), 4) $NO_2$ in $N_2$; 5) $NO_2$ in $N_2$ plus 20 cc/min air; 6) $NO_2$ in $N_2$ plus 20 cc/min (1.0% $SO_2$, 10.0% $O_2$ in $N_2$), $K_1$ is calculated from $[NO_2]/[NO]/[O_2]^{1/2}$

Table IV-2: $NO_x$ Removal with $K_2SO_4$

| Gas | Flow Rate (cc/min) | Outlet Concentrations NO (ppm) | $NO_2$(ppm) | $K_1$ | $NO_x$ Removal (Percent) |
|---|---|---|---|---|---|
| 1 | 80 | 535 | 0 | - | 0.7 |
| | 40 | 521 | 0 | - | 1.5 |
| | 20 | 529 | 0 | - | -0.8 |
| | 10 | 519 | 0 | - | 0.0 |
| 2 | 100 | 430 | 0 | 0 | 1.2 |
| | 60 | 342 | 0 | 0 | 2.3 |
| | 40 | 265 | 0 | 0 | -2.0 |
| | 30 | 180 | 0 | 0 | -2.9 |
| 3 | 100 | 435 | 0 | 0 | 0.0 |
| | 60 | 350 | 0 | 0 | 1.1 |
| | 40 | 255 | 0 | 0 | 3.4 |
| | 30 | 170 | 0 | 0 | 2.9 |
| 4 | 80 | 35 | 530 | 3620 | 0.9 |
| | 40 | 52 | 513 | 1934 | -0.2 |
| | 20 | 69 | 491 | 1211 | -0.8 |
| | 10 | 86 | 469 | 832 | -0.4 |
| 5 | 100 | 26 | 430 | 81 | -0.9 |
| | 60 | 32 | 340 | 58 | 0.8 |
| | 40 | 25 | 250 | 45 | -4.0 |
| | 30 | 25 | 155 | 24 | 3.9 |
| 6 | 100 | 29 | 436 | 106 | 0.0 |
| | 60 | 136 | 244 | 9.8 | -0.8 |
| | 40 | 200 | 75 | 1.7 | 2.1 |
| | 30 | 175 | 10 | 0.2 | 0.6 |

Cell contains $K_2SO_4$ powder, 400°C, gases are: 1) NO in $N_2$: 2) NO in $N_2$ plus 20 cc/min air; 3) NO in $N_2$ plus 20 cc/min (1.0% $SO_2$, 10.0% $O_2$ in $N_2$), 4) $NO_2$ in $N_2$; 5) $NO_2$ in $N_2$ plus 20 cc/min air; 6) $NO_2$ in $N_2$ plus 20 cc/min (1.0% $SO_2$, 10.0% $O_2$ in $N_2$), $K_1$ is calculated from $[NO_2]/[NO]/[O_2]^{1/2}$

Table IV-3: $NO_x$ Removal with $V_2O_5$

| Gas | Flow Rate (cc/min) | Outlet Concentrations NO (ppm) | $NO_2$(ppm) | $K_1$ | $NO_x$ Removal (Percent) |
|---|---|---|---|---|---|
| 1 | 80 | 520 | 16 | --- | 0.6 |
| | 40 | 510 | 20 | --- | -0.2 |
| | 20 | 515 | 25 | --- | -3.0 |
| | 10 | 495 | 30 | --- | -1.2 |
| 2 | 100 | 343 | 84 | 1.2 | 1.8 |
| | 60 | 232 | 113 | 1.8 | 1.4 |
| | 40 | 163 | 107 | 2.0 | -1.9 |
| | 30 | 91 | 81 | 2.4 | 1.7 |
| 3 | 100 | 414 | 6 | 0.1 | 3.4 |
| | 60 | 349 | 6 | 0.1 | -0.3 |
| | 40 | 252 | 8 | 0.2 | 1.5 |
| | 30 | 168 | 11 | 0.3 | -2.3 |
| 4 | 80 | 190 | 385 | 208 | -0.8 |
| | 40 | 287 | 287 | 83 | -3.5 |
| | 20 | 342 | 228 | 51 | -2.5 |
| | 10 | 378 | 182 | 35 | -1.3 |
| 5 | 100 | 141 | 314 | 11 | -0.7 |
| | 60 | 180 | 197 | 4.1 | -0.5 |
| | 40 | 152 | 128 | 2.6 | -5.7 |
| | 30 | 77 | 98 | 3.4 | 4.9 |
| 6 | 100 | 361 | 89 | 1.7 | 3.2 |
| | 60 | 311 | 59 | 1.0 | 1.9 |
| | 40 | 248 | 27 | 0.5 | 2.2 |
| | 30 | 170 | 10 | 0.2 | 3.3 |

Cell contains $V_2O_5$ powder, 400°C, gases are: 1) NO in $N_2$: 2) NO in $N_2$ plus 20 cc/min air; 3) NO in $N_2$ plus 20 cc/min (1.0% $SO_2$, 10.0% $O_2$ in $N_2$), 4) $NO_2$ in $N_2$; 5) $NO_2$ in $N_2$ plus 20 cc/min air; 6) $NO_2$ in $N_2$ plus 20 cc/min (1.0% $SO_2$, 10.0% $O_2$ in $N_2$), $K_1$ is calculated from $[NO_2]/[NO]/[O_2]^{1/2}$

Table IV-4: $NO_x$ Removal with Platinized silica-gel

| Gas | Flow Rate (cc/min) | Outlet Concentrations NO (ppm) | $NO_2$(ppm) | $K_1$ | $NO_x$ Removal (Percent) |
|---|---|---|---|---|---|
| 1 | 80 | 530 | 0 | --- | 1.7 |
| | 40 | 533 | 0 | --- | -0.8 |
| | 20 | 520 | 0 | --- | 1.0 |
| | 10 | 520 | 0 | --- | -0.2 |
| 2 | 100 | 264 | 161 | 3.0 | 2.3 |
| | 60 | 182 | 168 | 3.5 | 0.0 |
| | 40 | 127 | 138 | 3.4 | -2.0 |
| | 30 | 78 | 92 | 3.2 | 2.9 |
| 3 | 100 | 300 | 7 | --- | 29.5 |
| | 60 | 196 | 5 | --- | 43.2 |
| | 40 | 112 | 3 | --- | 56.4 |
| | 30 | 50 | 2 | --- | 70.0 |
| 4 | 80 | 550 | 23 | 2.5 | -0.5 |
| | 40 | 545 | 22 | 2.4 | -0.8 |
| | 20 | 543 | 22 | 2.4 | -1.9 |
| | 10 | 538 | 22 | 2.4 | -1.5 |
| 5 | 100 | 267 | 183 | 3.3 | 0.4 |
| | 60 | 183 | 194 | 4.0 | -0.5 |
| | 40 | 123 | 137 | 3.4 | 2.0 |
| | 30 | 74 | 103 | 3.7 | 3.8 |
| 6 | 100 | 286 | 4 | --- | 37.6 |
| | 60 | 170 | 3 | --- | 54.1 |
| | 40 | 93 | 2 | --- | 66.2 |
| | 30 | 45 | 2 | --- | 74.7 |

Cell contains plantinized silica gel, 400°C, gases are: 1) NO in $N_2$: 2) NO in $N_2$ plus 20 cc/min air; 3) NO in $N_2$ plus 20 cc/min (1.0% $SO_2$, 10.0% $O_2$ in $N_2$), 4) $NO_2$ in $N_2$; 5) $NO_2$ in $N_2$ plus 20 cc/min air; 6) $NO_2$ in $N_2$ plus 20 cc/min (1.0% $SO_2$, 10.0% $O_2$ in $N_2$), $K_1$ is calculated from $[NO_2]/[NO]/[O_2]^{1/2}$

Table IV-5: $NO_x$ Removal with Electrolyte (89% $K_2S_2O_7$-10% $K_2SO_4$-1% $V_2O_5$)

| Gas | Flow Rate (cc/min) | Outlet Concentrations NO (ppm) | $NO_2$(ppm) | $K_1$ | $NO_x$ Removal (Percent) |
|---|---|---|---|---|---|
| 1 | 80 | 540 | 0 | - | -0.2 |
| | 40 | 535 | 0 | - | -1.0 |
| | 20 | 520 | 0 | - | 1.0 |
| | 10 | 525 | 0 | - | -1.2 |
| 2 | 100 | 424 | 0 | 0 | 2.0 |
| | 60 | 353 | 0 | 0 | -1.0 |
| | 40 | 265 | 0 | 0 | -2.0 |
| | 30 | 171 | 0 | 0 | 2.3 |
| 3 | 100 | 430 | 0 | 0 | 1.1 |
| | 60 | 348 | 0 | 0 | 1.7 |
| | 40 | 260 | 0 | 0 | 1.6 |
| | 30 | 179 | 0 | 0 | -2.3 |
| 4 | 80 | 86 | 484 | 858 | 0.0 |
| | 40 | 155 | 410 | 198 | -0.2 |
| | 20 | 225 | 330 | 138 | 0.2 |
| | 10 | 304 | 256 | 68 | -1.2 |
| 5 | 100 | 57 | 388 | 33 | 1.5 |
| | 60 | 86 | 284 | 12 | 1.9 |
| | 40 | 86 | 179 | 6.4 | 0.0 |
| | 30 | 55 | 120 | 5.8 | 4.9 |
| 6 | 100 | 206 | 246 | 8.4 | 2.8 |
| | 60 | 267 | 105 | 2.2 | 1.3 |
| | 40 | 247 | 33 | 0.6 | 0.3 |
| | 30 | 172 | 5 | 0.1 | 4.8 |

Cell contains electrolyte ($K_2S_2O_7$ with 10.0% $K_2SO_4$ and 1.0% $V_2O_5$), 400°C, gases are: 1) NO in $N_2$: 2) NO in $N_2$ plus 20 cc/min air; 3) NO in $N_2$ plus 20 cc/min (1.0% $SO_2$, 10.0% $O_2$ in $N_2$), 4) $NO_2$ in $N_2$; 5) $NO_2$ in $N_2$ plus 20 cc/min air; 6) $NO_2$ in $N_2$ plus 20 cc/min (1.0% $SO_2$, 10.0% $O_2$ in $N_2$), $K_1$ is calculated from $[NO_2]/[NO]/[O_2]^{1/2}$

Table IV-6: $NO_x$ Removal with Electrolyte (99% $K_2S_2O_7$., 1% $V_2O_5$)

| Gas | Flow Rate (cc/min) | Outlet Concentrations NO (ppm) | $NO_2$(ppm) | $K_1$ | $No_x$ Removal (Percent) |
|---|---|---|---|---|---|
| 1 | 80 | 507 | 6 | -- | 4.9 |
| | 40 | 452 | 5 | -- | 13.5 |
| | 20 | 359 | 3 | -- | 31.0 |
| | 10 | 280 | 3 | -- | 45.5 |
| 2 | 100 | 206 | 12 | -- | 49.8 |
| | 60 | 108 | 7 | -- | 67.1 |
| | 40 | 52 | 3 | -- | 78.8 |
| | 30 | 24 | 2 | -- | 85.1 |
| 3 | 100 | 236 | 13 | -- | 42.7 |
| | 60 | 120 | 6 | -- | 64.4 |
| | 40 | 63 | 4 | -- | 74.6 |
| | 30 | 24 | 4 | -- | 79.4 |
| 4 | 80 | 157 | 11 | -- | 70.5 |
| | 40 | 81 | 7 | -- | 84.6 |
| | 20 | 39 | 5 | -- | 92.2 |
| | 10 | 24 | 4 | -- | 94.9 |
| 5 | 100 | 99 | 9 | -- | 76.2 |
| | 60 | 47 | 6 | -- | 85.8 |
| | 40 | 24 | 4 | -- | 89.8 |
| | 30 | 12 | 3 | -- | 91.8 |
| 6 | 100 | 131 | 13 | -- | 69.1 |
| | 60 | 70 | 7 | -- | 79.6 |
| | 40 | 42 | 3 | -- | 84.0 |
| | 30 | 22 | 2 | -- | 87.1 |

Cell contains electrolyte ($K_2S_2O_7$ with 1.0% $V_2O_5$), 400°C, gases are: 1) NO in $N_2$: 2) NO in $N_2$ plus 20 cc/min air; 3) NO in $N_2$ plus 20 cc/min (1.0% $SO_2$, 10.0% $O_2$ in $N_2$), 4) $NO_2$ in $N_2$; 5) $NO_2$ in $N_2$ plus 20 cc/min air; 6) $NO_2$ in $N_2$ plus 20 cc/min (1.0% $SO_2$, 10.0% $O_2$ in $N_2$), $K_1$ is calculated from $[NO_2]/[NO]/[O_2]^{1/2}$

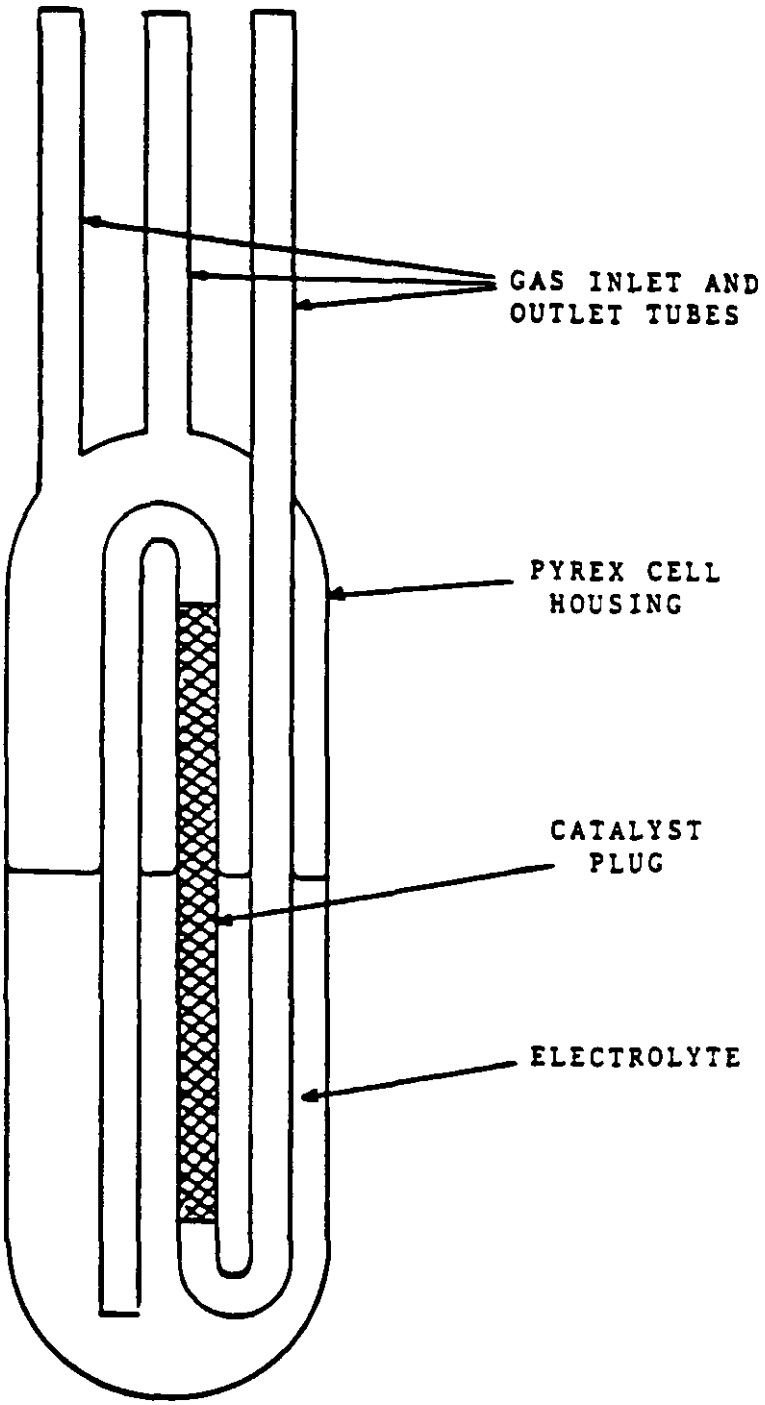


Figure IV - 1. Cell used in Effluent Analysis Experiments

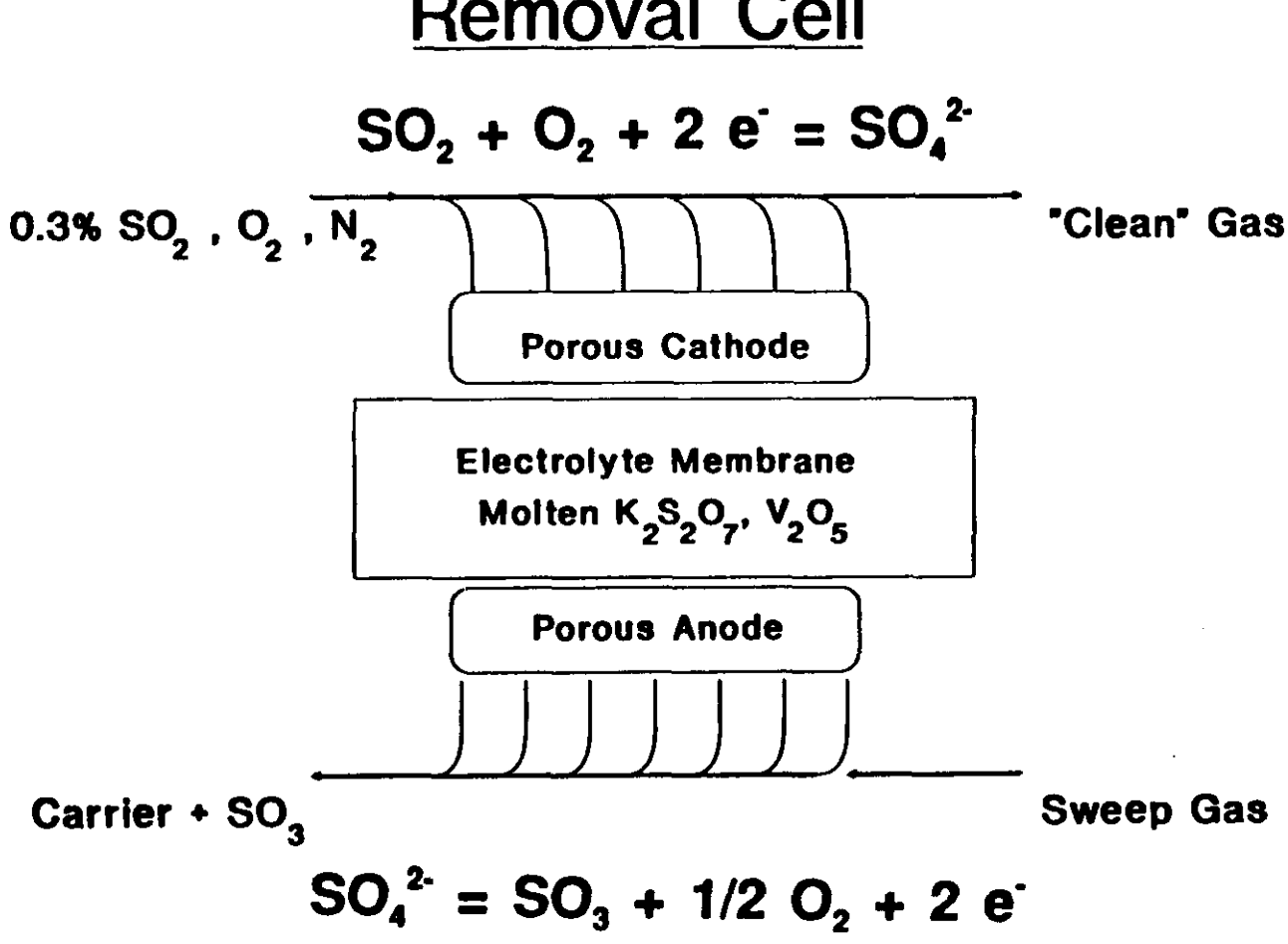


Figure IV-2 Schematic of Removal Cell

# NOx Study, Oxidizing Current

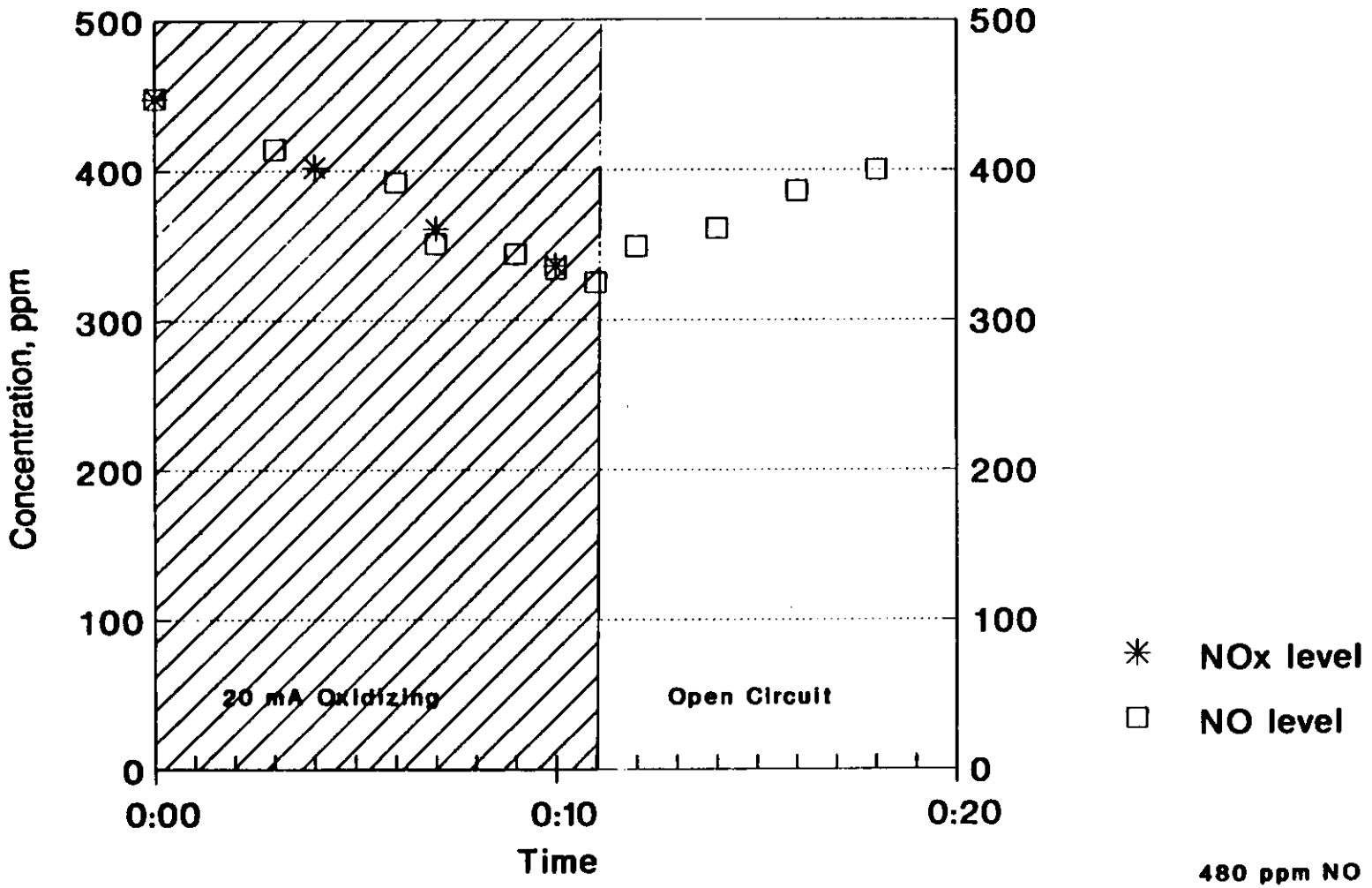


Figure IV-3.

# NOx Study, Oxidizing and Reducing Current

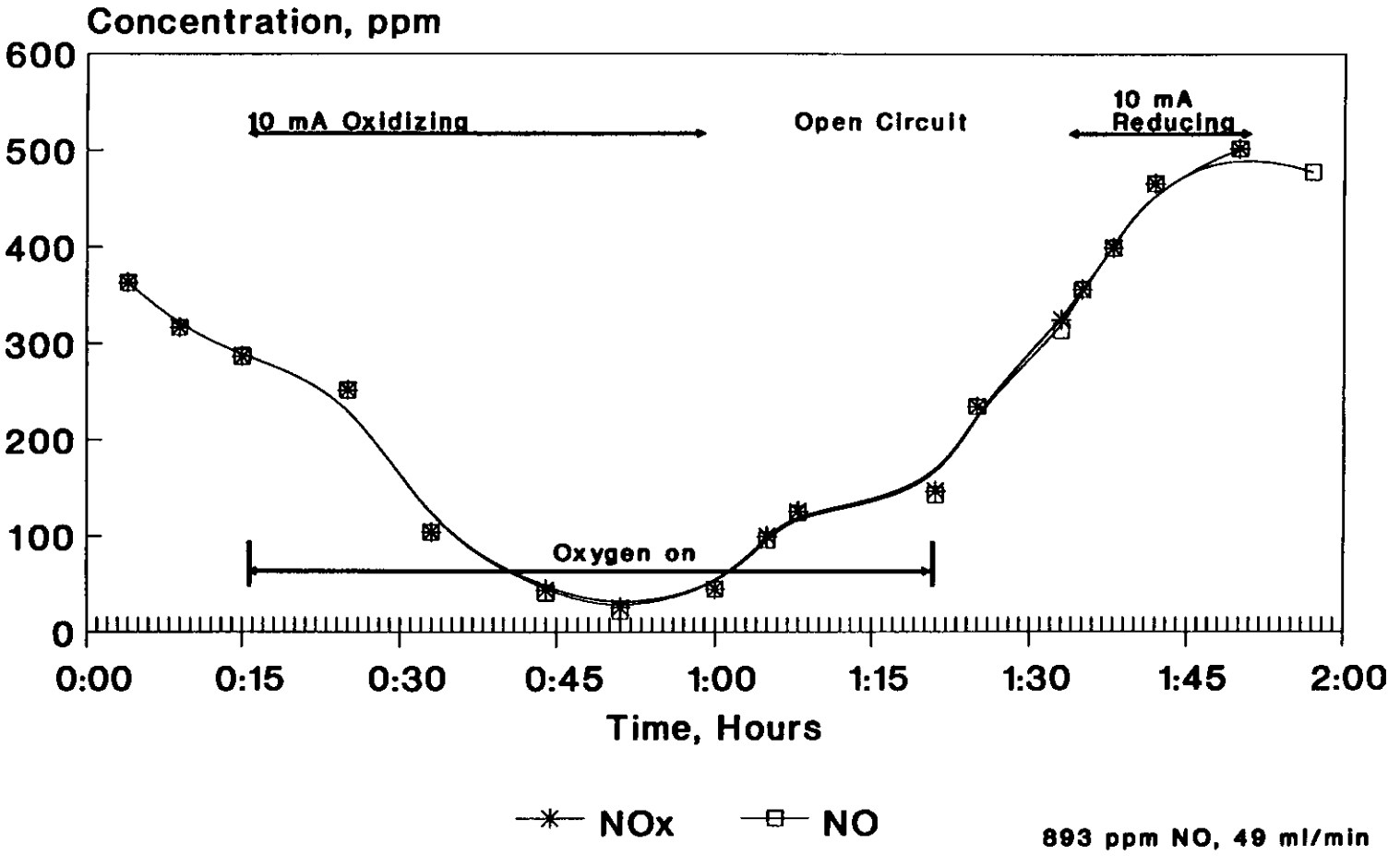


Figure IV-4. 425 degrees C.

# NOx Study, Reducing Current

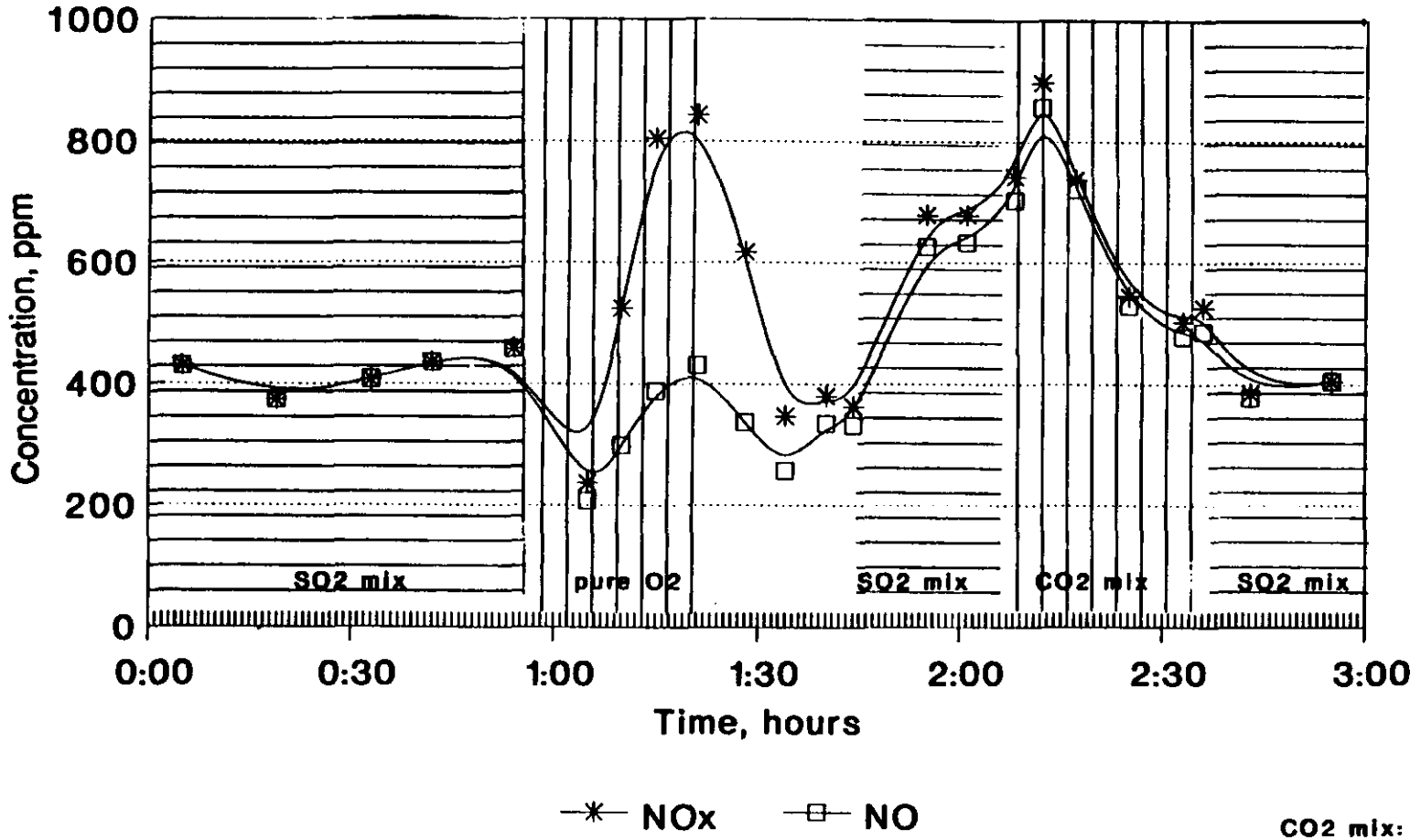


SO2 mix:
0.298% SO2
3.0% O2
Bal. N2
46 ml/min

CO2 mix:
0.301% SO2
3.0% O2
15% CO2
Bal. N2
68 ml/min

893 ppm NO; 44 ml/min
NO humidified before cell

Figure IV-5. 425 degrees C.
10 mA Reducing Current

## V. Simultaneous $SO_x/NO_x$ Removal

### A. Cell Performance Testing

#### 1. Membrane: 1 wt.% $V_2O_5$; MgO-based matrix; pre-oxidation Catalyst.

A diagram of the bench scale cell is shown in Figure V-I. The porous electrodes are made of the perovskite type compound, $La_{0.8}Sr_{0.2}CoO_3$. Detailed fabrication procedures utilized in making the electrodes are detailed in Section I. The perovskite electrodes have a superficial surface area of 20 $cm^2$, a thickness of 1.0 mm, a conductivity of 0.3 $(ohm\text{-}cm)^{-1}$, and are approximately 65% porous. The various electrolyte membranes were fabricated by the procedure outlined in Section II.

The free electrolyte studies, Section III, have helped to decipher the $SO_2$ removal mechanism at the cathode as follows:

$$2SO_2 + O_2 \rightarrow 2SO_3 \quad (21)$$

$$2S_2O_7^{2-} + 2e^- \text{ ---> } 3SO_4^{2-} + SO_2 \quad (20)$$

$$2SO_3 + 2SO_4^{2-} \text{ ---> } 2S_2O_7^{2-} \quad (22)$$

Thus, the overall cathodic reaction is:

$$SO_2 + O_2 + 2e^- \text{ ---> } SO_4^{2-} \quad (23)$$

At the anode sulfate is oxidized to the thermodynamically favored $SO_3$:

$$SO_4^{2-} \text{ ---> } SO_3 + 1/2\ O_2 + 2e^- \quad (31)$$

Comparing equations (23) and (31) one sees that the overall net cell reaction is zero but mass is selectively transferred from the cathode gas stream to the anode gas stream under the influence of an applied potential:

$$(SO_2 + O_2)\text{cathode} \text{ ---> } (SO_3 + 1/2\ O_2)\ \text{anode} \quad (62)$$

Vanadia in the electrolyte promotes the oxidation of $SO_2$, reaction (21). So that this reaction would not be a limiting factor a plug of platinized silica gel catalyst was placed in the cell inlet tubes to assure complete oxidation of the inlet $SO_2$. Otherwise, the small bench-scale cell we use has a very short contact time between the gas and electrolyte and reaction (21) becomes the limiting factor for $SO_x$ removal. The results presented in Figures V-2, V-3 and V-4, discussed below, are all at 400°C where complete oxidation of $SO_2$ to $SO_3$ occurs. Thus, all $SO_x$ removal is actually $SO_3$ removal.

Figure V-2 displays $SO_3$ removal results at the cathode. Initially, the electrolyte membrane contained a significant amount of sulfate, formed during synthesis of the membrane material. Thus, in the early stages of cell operation a large quantity of $SO_3$ was removed under conditions of zero current due to the removal reaction, equation (22). However, as time progressed, less and less sulfate remained in the membrane and open-circuit removal decreased. This trend is exhibited in Figure V-2 where removal at open-circuit is a maximum in trial 1 (conducted first chronologically) and gradually decreases to zero open-circuit removal in trial 4 (conducted last chronologically). The straight lines in Figure V-2 represent the ideal $SO_3$ removal versus current calculated from the stoichiometry of the overall cathodic reaction, equation (23).

A number of important conclusions can be drawn from the cathodic $SO_3$ removal data. First, the cell displayed the

capability of routinely removing 98 or 99% of the $SO_3$ and the removal was found to be a linear function of current. The relationship was found to correspond nearly precisely with the ideal stoichiometry of reaction (23). Current efficiencies were near 100% up to 95% $SO_3$ removal. Above 95% removal, mass transfer effects became significant and current efficiencies dropped below 100%.

Figure V-3 displays $SO_x$ concentration results at the anode (simulated flue gas also flowed through the anode compartment). Similar to the data in Figure V-2, open-circuit $SO_3$ removal decreased during cell operation as available sulfate was consumed. The straight lines in Figure V-3 correspond to the ideal evolution which is calculated from the stoichiometry of equation (31).

Similar to the cathode results, a linear relationship is observed between $SO_3$ concentration and applied current at the anode. However, the relationship is opposite to that of the cathode, precisely following the ideal concentration calculated from the stoichiometry of equation (31). Current efficiencies at the anode were at all times found to be near 100%.

Figure V-4 shows combined cathode and anode results of a single run. Once again, the results show that $SO_3$ is removed at the cathode and evolved at the anode. The amount of removal and evolution are proportional to the current and coincide precisely with the stoichiometry of the mechanism described above, equations (23) and (31). This indicates current efficiencies were once again near 100%. At 40 mA, over 98% of the $SO_3$ was removed at the

cathode and concentrated to about 1.0% in the anode gas. The concentration at the anode was limited only by the anode gas flow rate.

The effect of temperature was examined in a series of tests. Figure V-5 exhibits cathodic cell performance data at 375°C. At this temperature, the kinetics of reaction (21) are more sluggish. Under these conditions, approximately 95% oxidation was achieved in the cell. The results show $SO_3$ removal was again proportional to current and closely followed the stoichiometry of reaction (23). At currents above 8 mA, about 99% $SO_3$ removal was observed. The results also show that the $SO_2$ outlet concentration was unaffected by current until $SO_3$ removal was near its maximum. At this point a small decrease in $SO_2$ was observed (2.5% of the inlet $SO_x$). Two possible explanations exist which could explain the apparent $SO_2$ removal; either 1) the $SO_2$ reacted with or was absorbed by the electrolyte, or 2) the removal of $SO_3$ shifted the equilibrium and enhanced oxidation. The first explanation is unlikely. Electrolyte studies indicate $SO_2$ solubility is extremely low and reactions, to form sulfite or other lower oxidation state sulfur oxides, are virtually precluded by thermodynamics. Thus, the second interpretation appears to be correct. As current is increased and the $SO_3$ concentration becomes low, the equilibrium between $SO_2$, $O_2$ and $SO_3$ is shifted in favor of increased oxidation. However, only a small increase in oxidation is observed due to the flue gas/electrolyte contacting restrictions described earlier.

The results displayed in Figure V-6 are similar to those in

Figure V-5. In this case, the cell operating temperature is 350°C and approximately 70% oxidation is achieved in the cell. Once again, $SO_3$ removal is proportional to current and reflects the stoichiometry of reaction (23). About 98% $SO_3$ removal was observed at 10 mA. Furthermore, the outlet $SO_2$ concentration remained unchanged until the applied current removed the majority of $SO_3$. The subsequent decrease in $SO_2$ concentration was small (4.3% of the inlet $SO_x$), apparently due to the enhanced catalytic oxidation conditions at very low $SO_3$ concentrations.

The cell performance results were very encouraging for $SO_3$ removal. In all tests $SO_3$ removal was proportional to current, very closely following the stoichiometry of the removal reaction, equation (23). Therefore, current efficiencies were always near 100% in $SO_3$ removal, with virtually no unwanted side reactions occurring. Overall, the process demonstrated the ability to remove in excess of 98% of the $SO_x$ without any problem at 400°C. The results also showed the catalytic oxidation of $SO_2$ to $SO_3$ is a critical step in the $SO_x$ removal mechanism. This underlines the importance of vanadia in the electrolyte and indicates higher vanadia loadings may be beneficial. Cell performance did not decline at lower temperatures with respect to $SO_3$ concentrations. The only effect of temperature seems to be on the oxidation kinetics of reaction (21), at least in the temperature range of 350-400°C.

2. Glass Matrix; 5 wt.% $V_2O_5$; no Pre-Oxidation Catalyst.

This full cell study involved an $SO_2$ removal study to replicate previous results. Figure V-7 shows our findings at 400° C and those of an earlier run. Neither study used a pre-oxidation catalyst. Also included in the plot is the baseline study, a 1% vanadia electrolyte membrane. The removal values are similar in both 5 wt. % vanadia membranes and are slightly higher than that found for the 1 wt. % vanadia membrane. Percent removal is defined as:

$$\%SO_x \text{ Removal} = \frac{(\text{Inlet } SO_x - \text{Outlet } SO_x) \times 100}{\text{Inlet } SO_x}.$$

The increased removal in the present case can be attributed to the approach to open-circuit equilibrium. As the cell approaches equilibrium, the open-circuit $SO_2$ removal decreases to zero. The difference between the runs is due to the time allowed for equilibrium approach.

More important is the increasing removal with applied current. Unfortunately, the polarization of the cell would not permit steady-state application of -15 mA. We expect that the removal would follow the trend of the other studies and result in a removal of approximately 63%. Current efficiencies, also plotted in Figure V-7, are equally promising. The current efficiencies are still low at -15 mA applied so several polarization studies were performed to determine the cause of the low current efficiency.

3. $NO_x$ Removal - Reducing Current.

This full cell study investigated the ability of our

electrochemical membrane to remove nitric oxide from the working electrode gas stream. The membrane was 5 wt. % $V_2O_5$ and 95 wt. % $K_2S_2O_7$ electrolyte at 94% theoretical density. When the NO was first added to the flue gas (0.3% $SO_2$, 3.0% $O_2$, balance $N_2$), a minor amount of removal occurred. This removal is believed to result from adsorption of NO on all surfaces of the cell housing and supply tubes. An equilibrium was established after several hours and reducing current was applied. We observed no removal with reducing current. This was expected since the electrolyte is similar to that of previous NO removal studies (c.f. September 2, 1987 Quarterly Progress Report) which found no $NO_x$ removal with current. All $NO_x$ removal during that period was attributed to absorption in $SO_3$ which had condensed in the tubing. One shortcoming of this study is that we did not investigate the effect of oxidizing current on $NO_x$ removal.

4. $NO_x$ Removal - Oxidizing and Reducing Currents with varied gas mixtures.

An extensive $NO_x$ removal study was performed with various gas compositions and applied currents. Difficulties with the analysis procedure prevented us from making a quantitative analysis of this flue gas. However, the data do show a qualitative removal of NO and $NO_x$ under certain conditions. All results are presented and discussed in general terms. The electrode exposed to the simulated flue gas is herein denoted the working electrode.

The removal cell was built with our standard perovskite electrodes and a new electrolyte membrane containing 1 wt. % $FeSO_4$,

5 wt. % $V_2O_5$ and 94 wt. % $K_2S_2O_7$ and an equal part of glass matrix particles.

Figure V-8 shows that NO is removed from the gas by an oxidizing current. A small quantity of $NO_2$ is generated with applied current. This is to be expected because of the following reaction:

$$NO + 1/2\ O_2 \ <==>\ NO_2 \qquad (42)$$

whose equilibrium constant $K_{eq}$ = 3.55 at 400° C. This reaction could be enhanced by the oxidation current.

Figures V-9 and V-10 show a similar trend with lower oxidizing currents. In these three cases, both $SO_2$ and $O_2$ were included in the entering flue gas. While the oxidizing current removal mechanism is unknown, it is possible that NO is being removed by contributing to the oxidation of $SO_2$, via:

$$SO_2 + NO \ \rightarrow\ SO_3 + 1/2\ N_2 \qquad (45)$$

with the assistance of the vanadia ($V_2O_5$) catalyst. At 700K, the $K_{eq}$ for this reaction is $3.5 \times 10^8$, showing that a strong thermodynamic possibility exists for this mechanism. This scenario assumes that $SO_2$ is a suitable reductant in our cell environment. Several researchers have studied the reduction of NO by $NH_3$ over $V_2O_5$ catalysts.

Notice that when the current is shut off, the $NO_x$ level slowly returns to the initial value instead of overshooting. An overshoot would be characteristic of an accumulation of $NO_x$ in the electrolyte during the time of applied current. Several complex sulfur-nitrogen molecules may be able to accumulate in the electrolyte.

Therefore, on a qualitative basis, we believe the NO is being removed by a mechanism we have yet to determine.

In Figure V-11, we changed the inlet gas from NO to $NO_2$. This test was conducted with a constant reducing current and differing oxygen flow rates. It is apparent that $NO_x$ is being removed in the presence of oxygen. If reaction (42) were the sole reaction, the $NO_x$ level (NO level + $NO_2$ level) would stay constant. The presence of oxygen may cause an equilibrium shift but it does not account for the overall removal of $NO_x$. Some reaction is removing most of the $NO_x$ from the gas stream, with reducing current.

When oxidizing current is applied in Figure V-12, we see very interesting behavior. With no supplied $O_2$, the $NO_x$ levels decrease rapidly; when $O_2$ is added, the NO level stays low but the $NO_x$ increases, probably on account of reaction (42). When $SO_2/O_2$ flue gas is sent to the cell with the $NO_2$, the partial pressure of $O_2$ decreases, allowing reaction (42) to proceed towards the left. Also, the partial pressure of $SO_2$ increases, enhancing reaction (45), if it occurs, reducing the $NO_x$.

At the end of the run depicted in Figure V-12, the current is stepped to a reducing current. Immediately the NO and $NO_x$ increase. At the end of the run, all the $NO_x$ is present as NO, suggesting that the reducing current forces reaction (42) to the left.

Nitric oxide is supplied to the working electrode in Figure V-13 along with oxidizing current. When the run begins, only NO and $N_2$ are supplied and the $NO_x$ level decreases as in Figures V-8,

V-9, and V-10. When $O_2$ is added, the $NO_x$ drops even further. When the oxidizing current is removed, $NO_x$ increases, and when reducing current is applied, the $NO_x$ returns to the inlet value.

It is important to remember that both oxygen and sulfur oxides are present in the cell environment from several of the electrochemical reaction steps. These trace quantities are insignificant when the gases are supplied directly to the working electrode inlet.

5. $NO_x$ Removal Study -Oxidizing Current

The membrane used in this $NO_x$ removal study contained 1% $TiO_2$ and 1% $FeSO_4$ in addition to the normal 5% $V_2O_5$, $K_2S_2O_7$ and borosilicate particles (85% theoretical density). The $Fe^{2+}$ ions and the $TiO_2$ were added to enhance the $NO_x$ removal. These materials have been used by other researchers in their $NO_x$ removal work.

When NO is added to the working electrode gas supply, the mass balance does not close. The outlet level is 12% lower than the inlet at open circuit. We have observed this in all subsequent $NO_x$ studies. As the gas continues to flow, this level becomes the steady-state value. We have been unable to determine if the NO is condensing on the tubing or if it is heterogeneously decomposing on the surface of the electrodes and cell housing. Voorhoeve, Remeika and Trimble[8] have shown NO decomposition over reduced

---

[8]. R. J. H. Voorhoeve, J. P. Remeika and L. E. Trimble, "Nitric Oxide and Perovskite-Type Catalysts: Solid State and Catalytic Chemistry," The Catalytic Chemistry of Nitrogen Oxides, Klimisch and Larson, eds., Plenum Press, NY, 1975.

perovskites and Hightower and Leirsburg[9] have cited examples where decomposition is possible on alumina and quartz. We have been unable to determine if our immediate removal is due to condensation or decomposition but have taken steps to determine this in the next $NO_x$ run.

As ten milliamps of oxidizing current is applied to the working electrode, the NO level decreases, as in previous experiments. Figure V-14 shows how the removal changes over time. We are confident that the observed removal is due to a chemical reaction, for there is no overshoot in NO level when the current is turned off, as would be seen if the NO was accumulating in the electrolyte. NO may be removed by the reaction:

$$SO_2 + NO \quad <==> \quad SO_3 + 1/2\ N_2 \qquad (45)$$

To investigate reaction (45), $SO_2$ and NO were supplied to the working electrode and a potentiostatic experiment was performed. Potentiostatic operation allows us to determine when reactions begin and how fast they proceed by monitoring the current flow. Figure V-15 shows the progress of the experiment. Note that the cell configuration has been changed (working electrode made from 40 mesh particles) to reduce the effects of concentration over-potential.

Figure V-16 shows the relationship between NO % removal and cell current for this study. Extrapolating, the apparent open

---

[9]. J. W. Hightower and D. A. van Leirsburg, "Current Status of the Catalytic Decomposition of NO," The Catalytic Chemistry of Nitrogen Oxides, Klimisch and Larson, eds., Plenum Press, NY, 1975.

circuit removal is five per cent. Moles removed, based on inlet level, are plotted against current in Figure V-17. Calculations on this data showed that approximately 4 moles of electrons are required for each mole of NO removed under oxidizing current. We have not been able to determine the exact removal mechanism. However, this finding points towards the formation of $HNO_3$ at the anode, as proposed in section IV-C-4.

6. Cell Polarization.

While the above $NO_x$ studies were performed, we also studied the cell potential over time. These studies showed that the cell polarization is reversible, but the cell requires a long time to return to the rest potentials. We interpret this as a sulfate ion buildup in the electrodes due to the pore flooding. With flooded pores, the effective surface area of the electrodes is reduced. This prevents $SO_2$ and $SO_3$ from diffusing to the sulfate. The sulfate will eventually accumulate to a level such that the melting point of the electrolyte reaches the operating temperature. This further increases the cell polarization and resistance. The reference electrode, a gold wire, also may be incapable of maintaining the $SO_2/SO_3$ equilibrium, thus not providing a thermodynamic reference voltage.

To correct this last problem, a platinum reference electrode was used, bathed in $SO_2$ and $O_2$ (0.298 and 3.01%, respectively). To prevent the local buildup of sulfate ions, the $SO_2/O_2$ mix is preoxidized to $SO_3$ by a platinum coated gas supply tube. Concentric mullite supply tubes permit the gas to pass through the

annulus and over the platinum surface. A platinum wire runs down the interior of the inner tube and contacts the electrolyte. This setup keeps the reference at a stable potential by maintaining it in pyrosulfate ions.

To alleviate electrolyte flooding, one electrode was made from larger particle perovskite and hence has larger pores. The perovskite was processed as usual but a section of 40 mesh (300 - 425 μm) particles were selected, pressed and sintered as usual. The normal electrode production method uses the 50 mesh (150 - 300 μm) particles to produce a fine porous structure compared to the 40 mesh particles. The effect of this change was very pronounced during the full cell study. There is a trade-off between lower surface area and lower capillary action towards the electrolyte.

The data in Figure V-18 were collected soon after the cell was assembled and brought to operating temperature. This plot shows the different performance of the two electrodes as the current was changed in sign and magnitude. The table to the right of the plot gives the average values of the slope of the curves after they became linear. It is apparent that the counter electrode, made of 40 mesh particles, gives a flatter response to applied current. This shows that the larger pores are less subject to concentration overpotential caused by pore flooding, as would be expected, due to their reduced capillarity. Figure V-19 shows the improvement in polarization achieved to date. The old MgO - based membrane has a steeper curve than the silicalite membrane.

Quantitatively, the plot shows that we can push three times

as much current through the silicalite matrix membrane as through the MgO-based membrane. Further improvement is required to reach the process design specifications.

B. Alternate Matrix Material Performance

This section focuses on the performance of several membranes made with the alternate matrix materials found in Table V-1. The properties of these membranes may be found in Table V-2.

1. Full cell test of borosilicate-based membrane

One of two full cell studies used a glass particle membrane. Cell polarization was studied eight hours into the run. With -20 mA applied to the working electrode, the anodic potential increased and then reached a constant level of about 0.55 V vs. reference (see Figure V-20). The cathodic potential did not reach a steady-state level, but performed better than in previous studies.

Twenty-four hours after start-up, -20 mA was applied again as shown in Figure V-21. Similar behavior is seen here, with the cathodic potential beginning to level off. These results show some improvement in the cell behavior, with fewer pores flooding. However, the following day, the cell had a higher polarization with half as much current applied (see Figure V-22). This deterioration continued on the following day. However, compared with previous studies, there is moderate improvement.

2. Full cell test of Silicalite-based membrane

A Silicalite-based membrane appears to be even more promising based on results obtained in the full cell. A full cell study was performed with the Haldor-Topsoe $SO_2$ oxidation catalyst installed

before the removal cell. The pre-oxidation reactor operated at 400° C to convert all of the influent $SO_2$ to $SO_3$. As the removal study progressed, we noticed that the reactor was not at steady-state, but rather was accumulating sulfur oxides. This lack of reactant severely limited cathodic performance in the cell.

However, Figure V-23 shows remarkable results at the anode. Data gathered for the Silicalite-based membrane are compared with an MgO-based membrane. The anodic overpotential (defined as potential with current applied minus equilibrium potential) is small and constant, approximately 0.17 V. Unfortunately, the cathode was highly diffusion-limited by the lack of reactant. This prevented continuation of the study for more than fifteen minutes. The lower overpotential shows there is less flooding of the electrode pores. When the pores flood, sulfate ions accumulate, causing a concentration polarization effect. This polarization shows up as overpotential in an electrochemical process.

3. Higher mass % of Silicalite.

This full cell study used a normal cell configuration with an electrolyte membrane fabricated from 8.0 g Silicalite and 12.0 g of 5 wt% $V_2O_5$ electrolyte. This cell was not conductive at temperatures up to 400° C. Measured resistances were on the order of 150 Ω. This appears to be due to either of the following conditions:

1. Minimal electrical contact between the electrodes and the electrolyte membrane. The electrodes used in this study were broken into pieces, limiting the conduction through

the cell.

2. Insufficient electrolyte in the membrane for ionic conduction across the membrane. This would be due to an overloading of the electrolyte with zeolite particles.

4. Repeat of 2. (above).

This full cell study used a normal perovskite counter electrode and a large pore working electrode. The membrane in this study contained 5 g Silicalite and 15 g of the 5 wt.% $V_2O_5$ electrolyte.

The cell was heated to 400° C and gas flows were stabilized to require ~18 mA for 100% theoretical removal. The cell showed stable behavior up to -30 mA, as shown in Figure V-24. These results are further compared to those of the old MgO-based membrane in Figure V-25. Here we see that the new cell is capable of passing twice the current with equal overpotential at the cathode (working electrode).

The anode shows great improvement, and is able to handle five times the current with the same overpotential. Recall that the counter electrode (anode) was a standard perovskite electrode. This means that all of the improvement is due to the membrane. The silicalite retains the electrolyte better than the MgO particles. However, the polarization, characterized by the overpotential, increased over the next few days, showing that electrolyte is slowly leaking from the membrane. The improvement at the cathode may be limited by the oxidation of $SO_2$ to $SO_3$, since the $V_2O_5$ has limited exposure to the gas stream.

5. Repeat of 4. (above).

In Figure V-26, we see that the electrolyte is conductive at 325° C. The anodic potential stabilizes near +1.1 Volts vs. reference. However, the cathode is not stable and continues to proceed negative over time. This is due to the slow $SO_2$ oxidation kinetics on $V_2O_5$ at 325° C. The cathodic behavior should improve with increasing temperature.

At 400° C, the $SO_2$ oxidation on $V_2O_5$ increases. Open circuit gas analysis shows that the $V_2O_5$ is capable of oxidizing 60% of the inlet $SO_2$. Under these conditions, -20 mA were applied to the cathode. This current corresponds to 100% theoretical removal. Figure V-27 shows the anode to be stable over long times. The potential stays at +0.335 Volts vs. reference. Additionally, the cathode is relatively stable, showing only a slow drift over time.

Figure V-28 displays the cathodic $SO_x$ levels over the duration of the run presented above. There is a slight increase in the outlet $SO_2$ level, due to the inability of the $V_2O_5$ to oxidize all of the electrochemically generated $SO_2$. Although there is a slight increase in the outlet $SO_3$ rate, these values differ by the experimental error, negating this trend. Throughout the duration of this run the $SO_x$ mass balance does not close, due in part to a leak of 15% of the inlet gas out of the cell. The remainder is due to non-steady-state operation of the cell. Some of the $SO_3$ is reacting with residual $SO_4^{2-}$ in the membrane.

Figure V-29 presents the anodic $SO_x$ levels during the same run. Here we see that no $SO_2$ exits from the cell; that is, the

platinum-on-silica-gel catalyst oxidizes all of the inlet $SO_2$. Secondly, we see that the outlet $SO_3$ level is low. It is expected that the $SO_3$ would be higher than the inlet level due to the removal mechanism. However, the cell was leaking 25% of the inlet flow and residual sulfate still exists, as noted above.

On the following day, the gas flow rates were adjusted such that 18 mA are required to reach 100% theoretical removal. The cell was stable for two hours with -30 mA applied to the cathode. When the potentials became too large, the current was decreased to -20 mA for the duration, as shown in Figure V-30. The cause of the high anodic overpotential appears to be electrode pore flooding with subsequent sulfate ion buildup.

Figure V-31 shows the response of the cathodic $SO_x$ flow rates over the run. The outlet $SO_2$ concentration remains constant during the run while the outlet $SO_3$ concentration drops slightly. The mass balance does not close, but there is some leakage through the seal.

The anodic $SO_x$ levels are presented in Figure V-32. We immediately notice that the outlet $SO_3$ rate increases rapidly after an initiation period. This will be described below. Our gas chromatograph detected some $SO_2$ in the outlet gas. We have no explanation for the increase in $SO_2$ from the zero-level on the previous day, unless gas was crossing the membrane from the cathode compartment.

Figure V-33 displays a combination of these results. Focusing on the $SO_3$ curves, it is seen that the anodic $SO_3$ does not increase until the potential reaches 1 Volt. Several possibilities exist as

causes for this phenomenon. This initiation period may be due to establishing vapor-liquid equilibrium in the cell outlet tubes. Some liquid $SO_3$ is always present in the outlet tubes of both sides of the cell at all times. It is possible that the anodic electrochemical reaction requires this overpotential for activation. Also, the overpotential may not be a cause of the $SO_3$ increase, but rather an effect. The $SO_3$ comes from oxidation of the $S_2O_7^{2-}$ and $SO_4^{2-}$ ions. Any excess sulfate ions would react with $SO_3$ to reform pyrosulfate, pushing the potential more positive. Therefore, it would seem that the $SO_3$ reacts with $SO_4^{2-}$ until the potential indicates equilibrium. At this time, the electrochemically generated $SO_3$ is free to exit the cell. This appears to be the most likely explanation.

While this full cell study proved quite interesting and successful, lack of cathodic pre-oxidation catalyst did not allow us to determine whether the low electrode surface area (due to pore flooding) or the low $SO_2$ oxidation is limiting the performance of the electrolyte membrane. All runs in this section were conducted at currents equal to 100% theoretical removal. However, the removal is limited to 66%. This corresponds closely to the amount of $SO_2$ oxidized by the $V_2O_5$ catalyst in the electrolyte at open circuit. With no current applied, 60% of the inlet $SO_2$ is oxidized to $SO_3$. This level of oxidation increases when current is applied, as gaseous $SO_3$ is removed by the electrolyte.

The cathodic electrochemical reaction mechanism generates $SO_2$. This $SO_2$ must be oxidized to $SO_3$ for removal. Note that in the

figures for this section, the cathodic $SO_2$ level remains constant over time. All electrochemically generated $SO_2$ appears to be oxidized. Over the duration of the last run, we see that the cathodic level of $SO_3$ decreases as the run proceeds. However, not all of the $SO_3$ is removed, for the following reason. If the electrode pores are flooded, the amount of interfacial area is greatly reduced. This in turn limits the amount of exposed sulfate ions ($SO_4^{2-}$) which can react with the gaseous $SO_3$. Hence, not all of the $SO_3$ is removed.

In summary, $SO_2$ removal is limited by two factors. First, without a suitable pre-oxidation catalyst, removal does not exceed 66% at 400°C, relative to inlet concentrations. However, when this catalyst is included in the inlet gas tubes of the cell, removal reaches 98+%. The second limitation is due to partially flooded pores. At the end of this run, the electrodes were removed from the cell and scraped to remove excess electrolyte. The electrodes each gained 2.5g or 50% of their starting weight. This equals 1.08 $cm^3$ of electrolyte in the pores, or, the pores are 60-70% full of electrolyte. Further membrane development will reduce this level of pore flooding, allowing operation at high current densities and low overpotential.

Table V-1: Alternate Matrix Materials

| Material | Composition by weight | Particle size, μm | Pore size, A° |
|---|---|---|---|
| borosilicate glass | Corning 7740 | 1 - 30 | ------ |
| Silicalite | $SiO_2:Al_2O_3$ = 280 | 1 - 5 | 5.5 |
| 13X Zeolite | $SiO_2:Al_2O_3$ = 4 | 1 - 5 | 7 |
| 4A Zeolite | $SiO_2:Al_2O_3$ = 1 | 1 - 5 | 4 |
| 5A Zeolite | $SiO_2:Al_2O_3$ = 1 | 1 - 5 | 5 |
| ball milled glass | Corning 7740 | 1 - 5 | ------- |
| LUDOX AS-40 | $SiO_2:Al_2O_3$ = 1 | $22^{*}10^{-3}$ | ------- |

Table V-2: Properties of Membranes made from alternate matrices

| Matrix | Composition | % $\rho_{th}$ |
|---|---|---|
| Borosilicate | 8. g glass, milled 6 days<br>12. g 5 wt. % $V_2O_5$ eletrolyte | 84. |
| Silicalite | 5. g Silicalite<br>15. g 5 wt. % $V_2O_5$ electrolyte | 90. |
| Silicalite | 8. g Silicalite<br>12. g 5 wt. % $V_2O_5$ electrolyte | 86. |
| Silicalite | 5. g Silicalite<br>0.75 g $V_2O_5$<br>14.25 g $K_2S_2O_7$ | 89. |
| Silicalite | 4.5 g Silicalite<br>0.77 g $V_2O_5$<br>14.75 g $K_2S_2O_7$ | 83. |

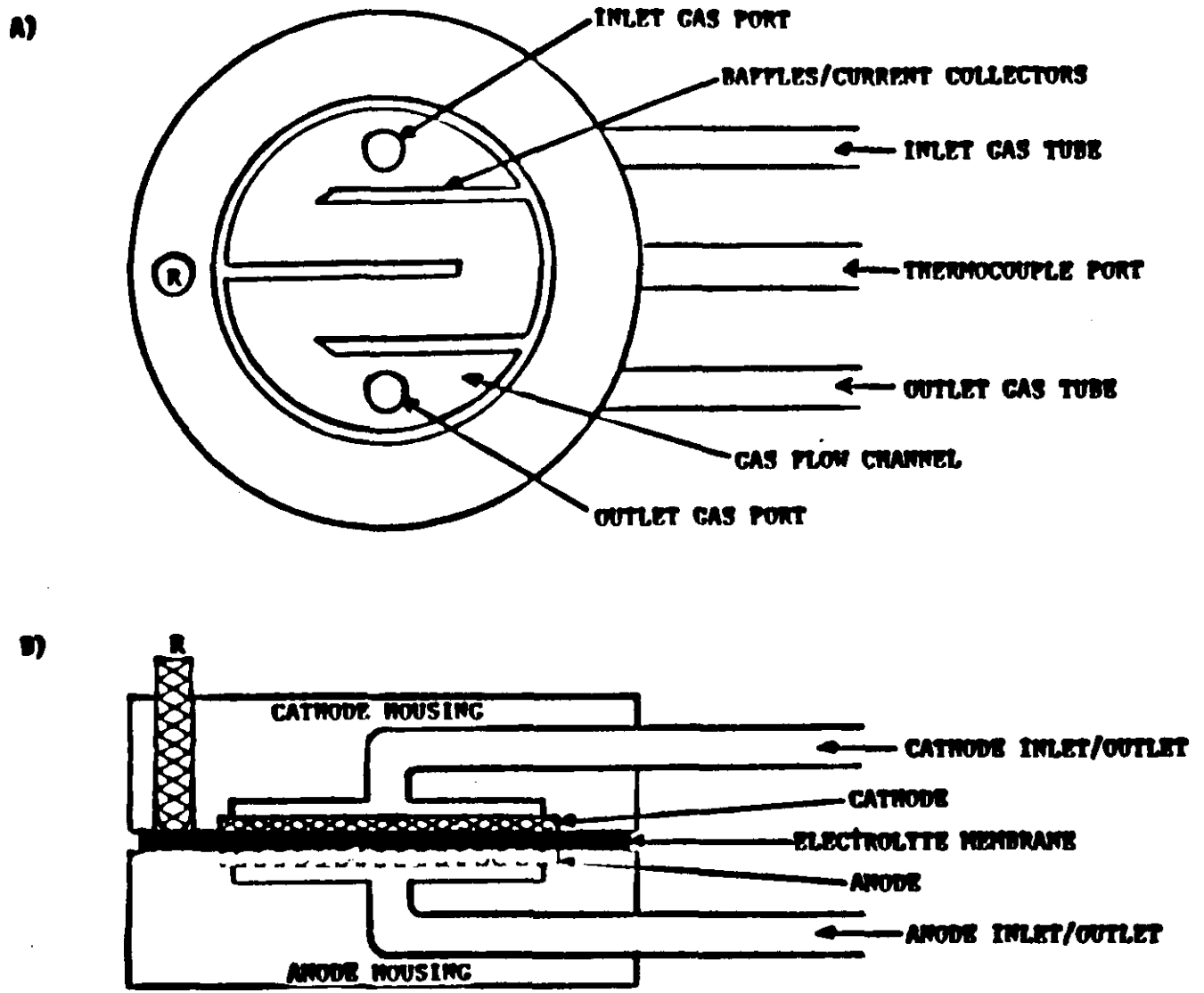


Figure V-1 Schematic of Membrane Cell A) Cell housing B) Assembled cell cross-section

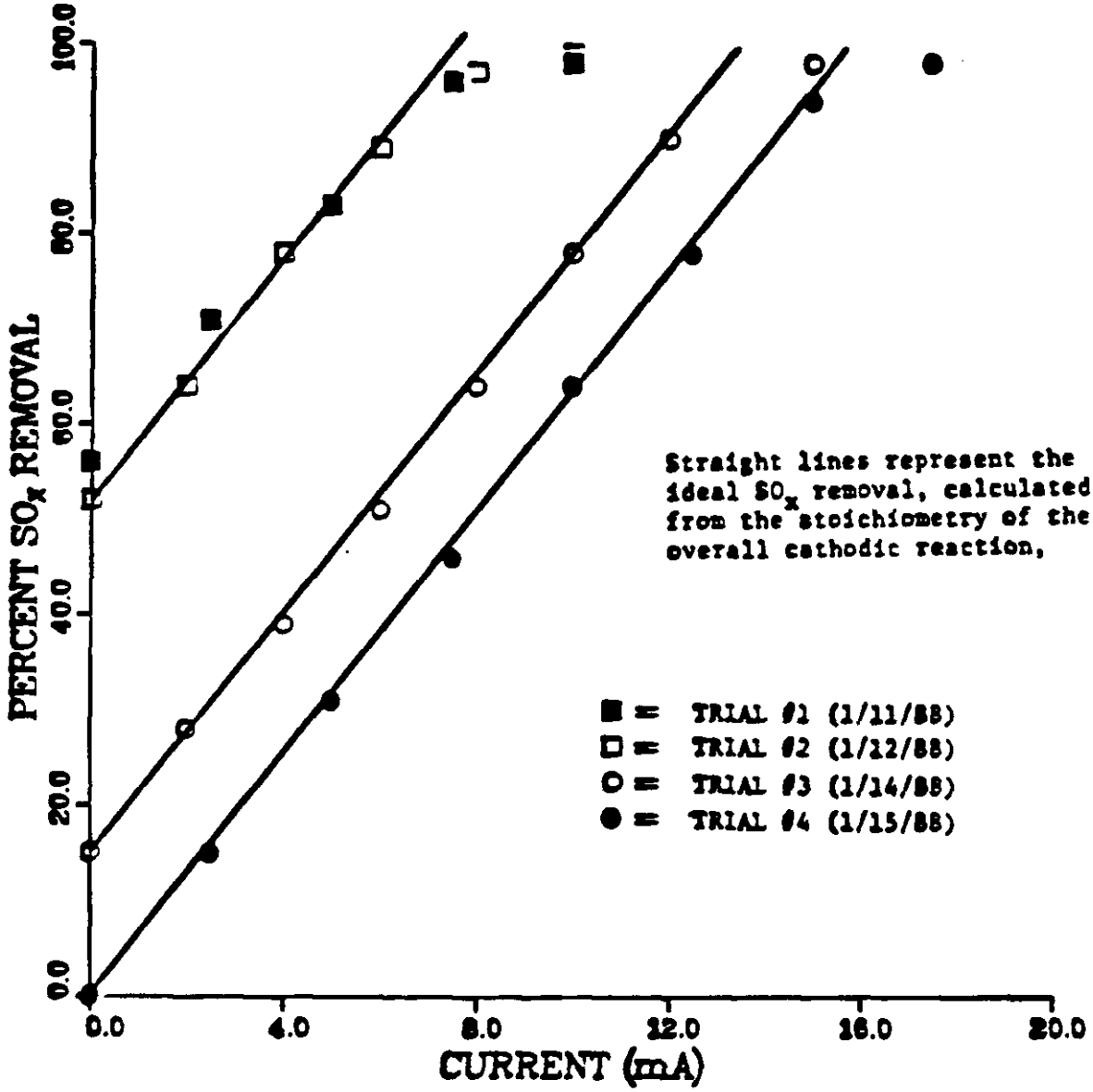


Figure V-2 Cathodic $SO_x$ removal as a function of applied current, 40 cc/min (0.3% $SO_x$, 3.0% $O_2$, 15% $CO_2$ in $N_2$) and 400°C. A catalyst plug oxidizes the inlet so that virtually all $SO_x$ is $SO_3$

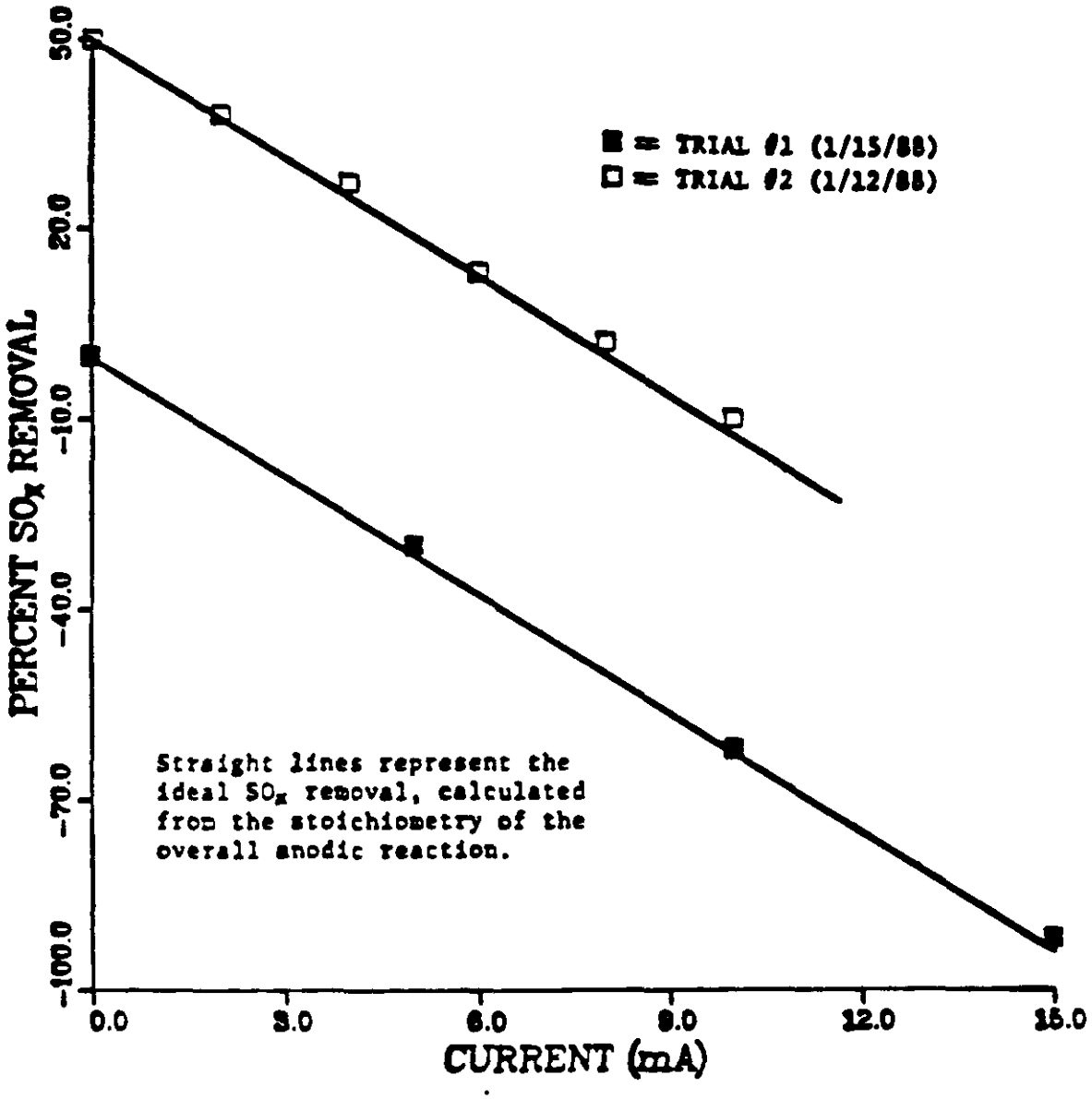


Figure V-3 Anodic $SO_x$ removal as a function of applied current, 40 cc/min (0.3% $SO_x$, 3.0% $O_2$ 15% $CO_2$ in $N_2$) and 400°C. A catalyst plug oxidizes the inlet so that virtually all $SO_x$ is $SO_3$

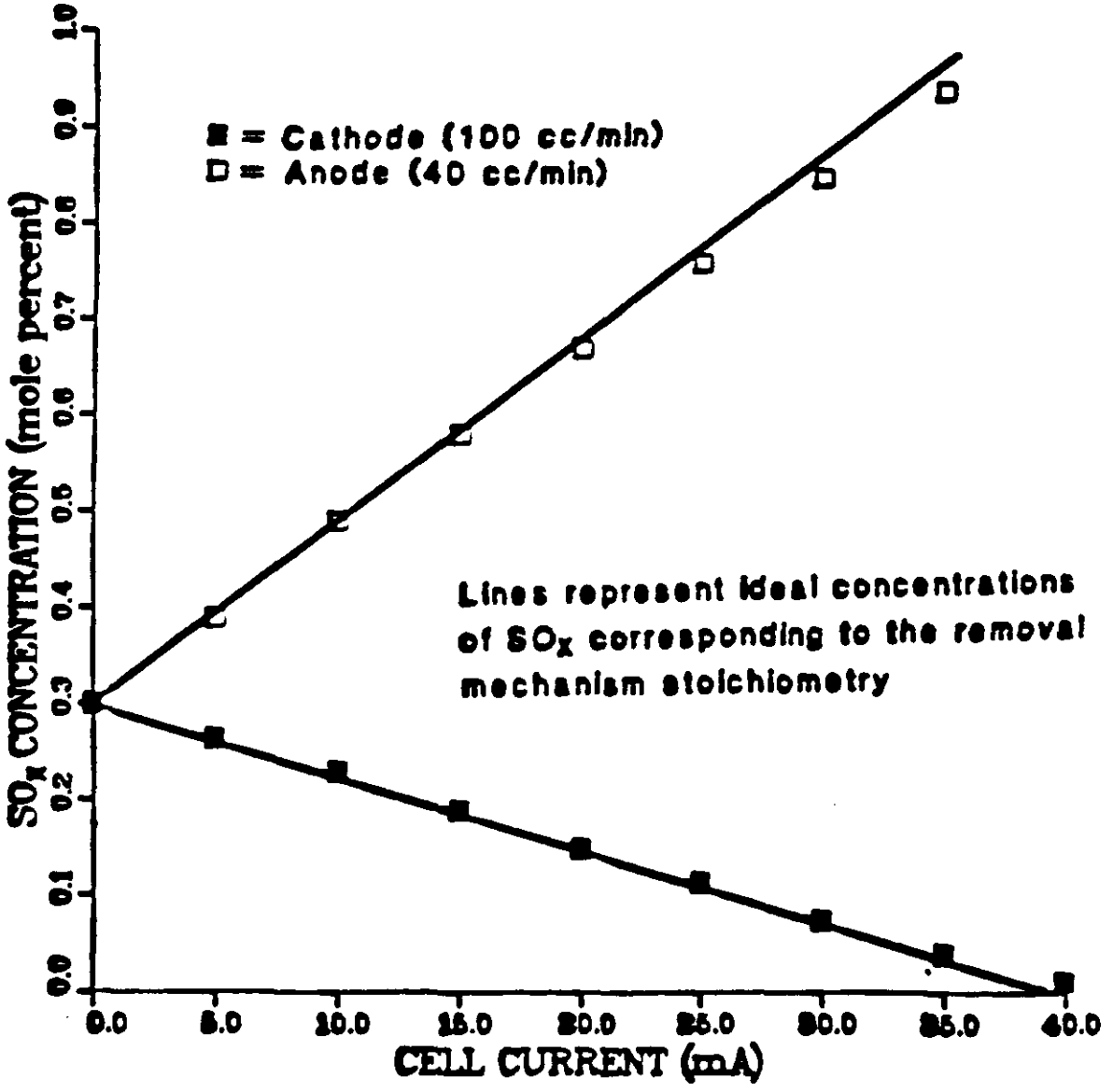


Figure V-4 Cathodic and anodic cell performance at 400 C with simulated flue gas flowing into both compartments (0.3% $SO_2$, 3.0% $O_2$, 15% $CO_2$ in $N_2$)

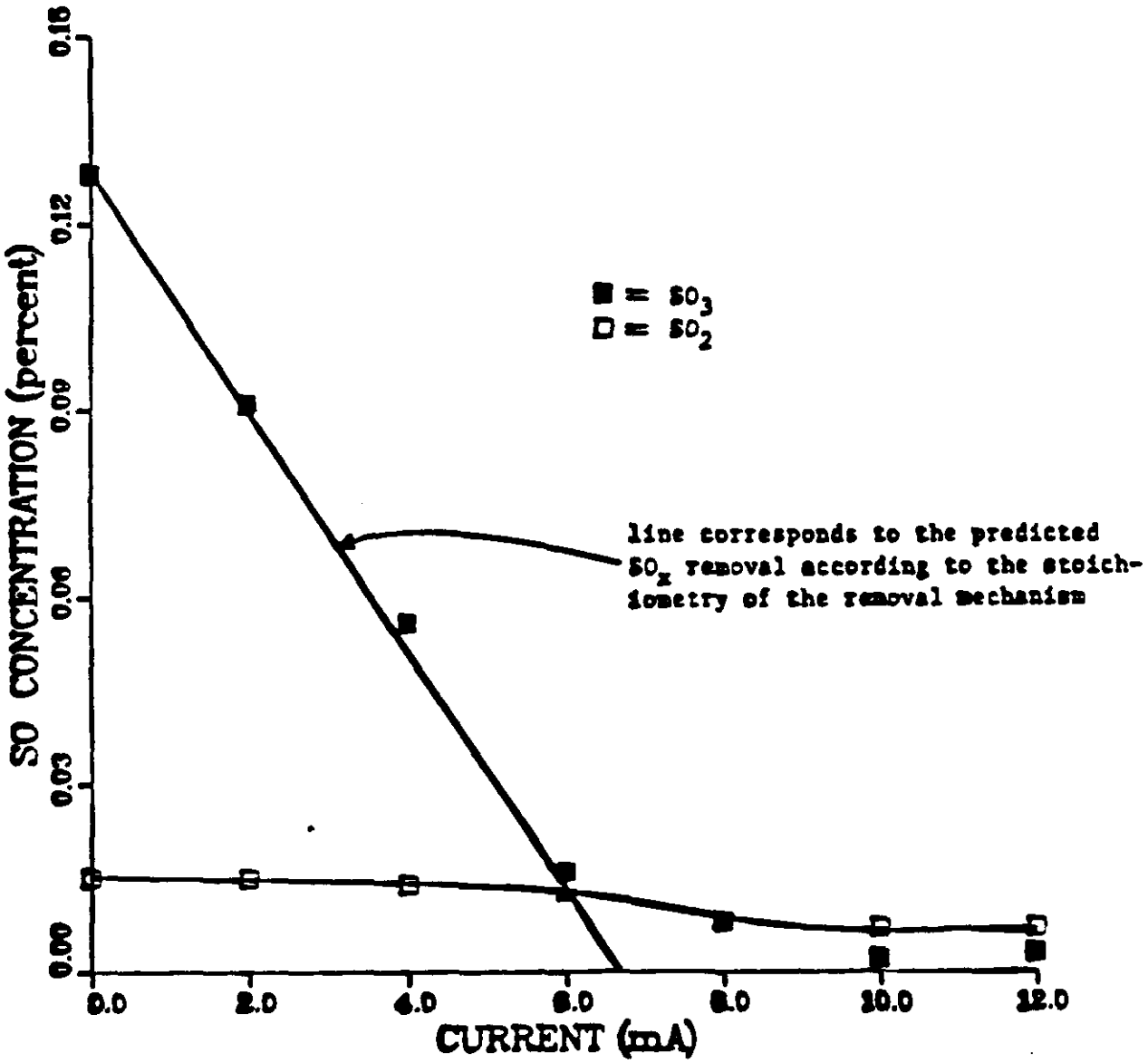


Exhibit V-5 **Cathodic cell performance at 375 C with simulated flue gas as the cathode feed (0.3% $SO_2$, 3.0% $O_2$, 15% $CO_2$ in $N_2$) at 40 cc/min.**

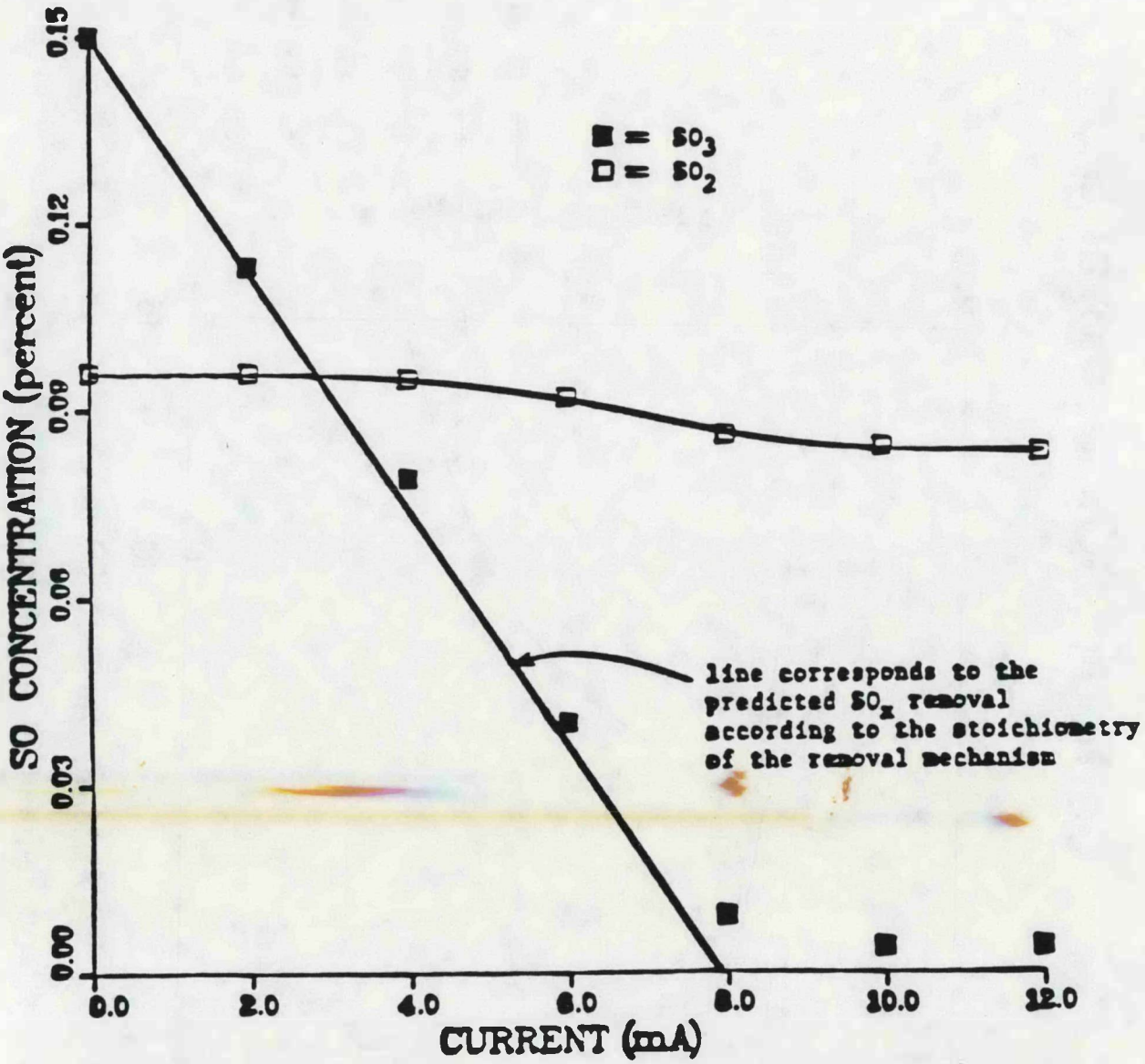


Figure V-6 Cathodic cell performance at 350°C with simulated flue gas as the cathode feed (0.3% $SO_2$, 3.0% $O_2$, 15% $CO_2$ in $N_2$) at 40 cc/min.

# Cathodic SOx Removal Study

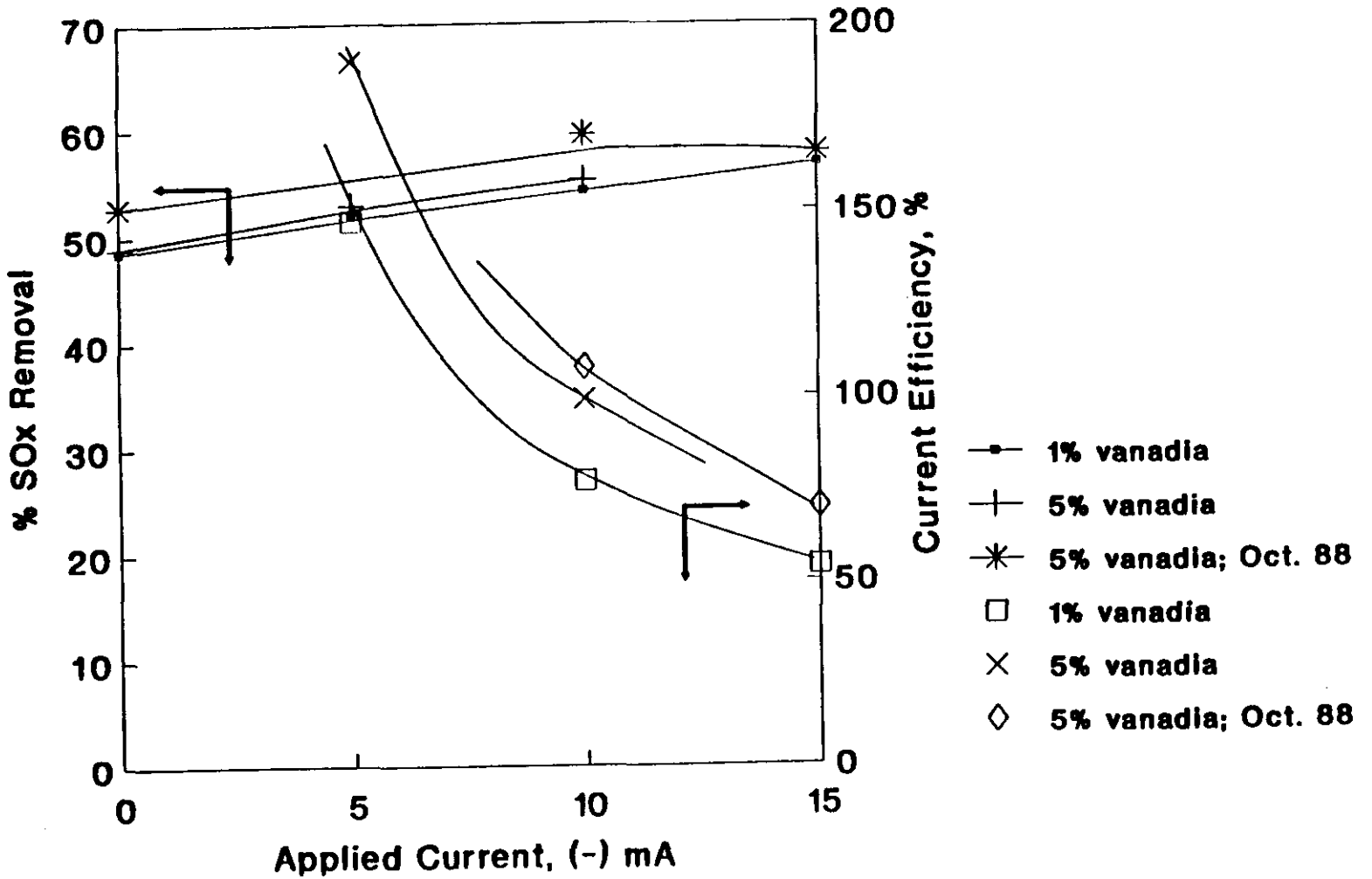


Figure V-7. 400 degrees C.

# NOx Study

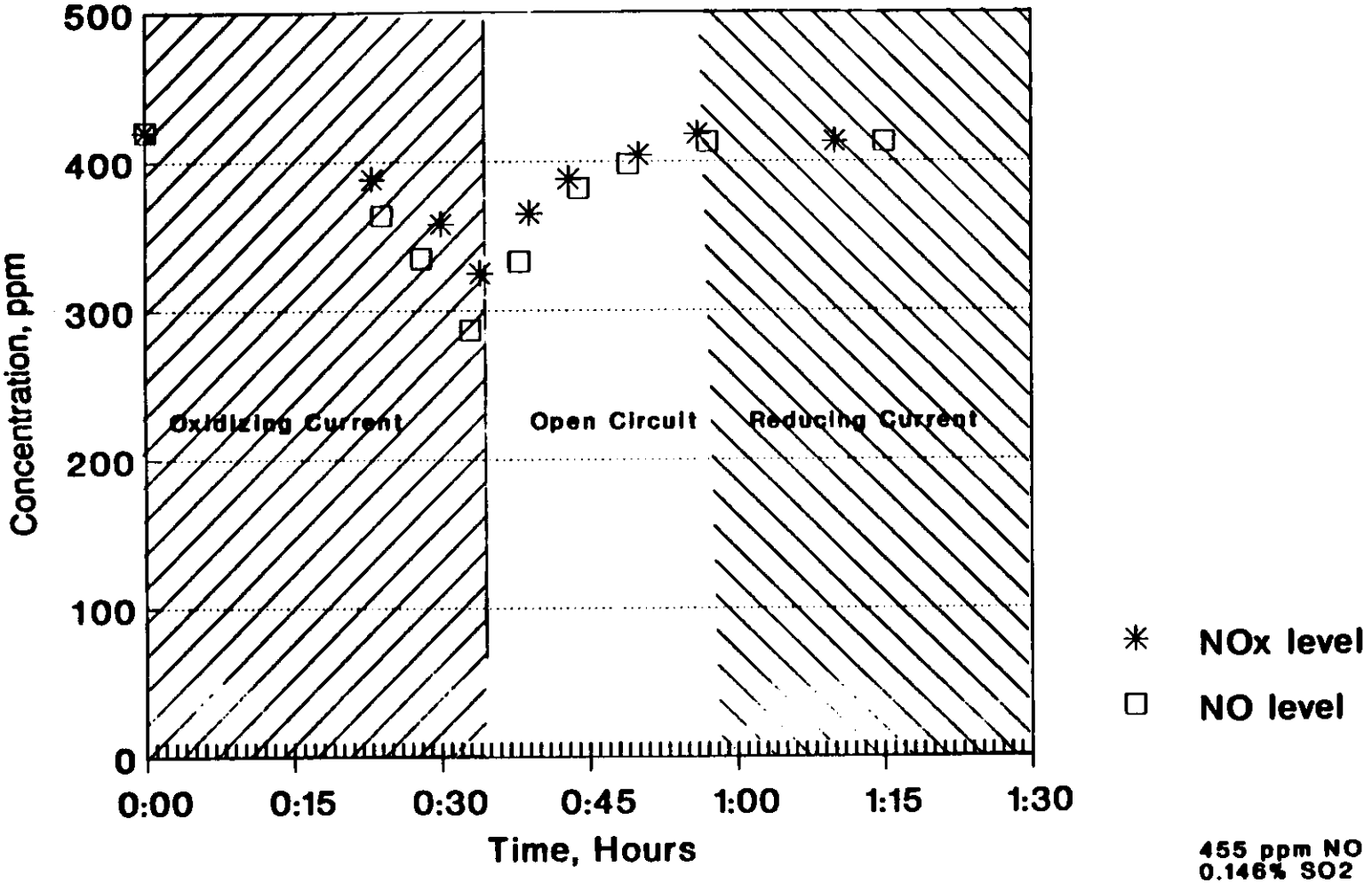


Figure V-8. 400 degrees C.

# NOx Study

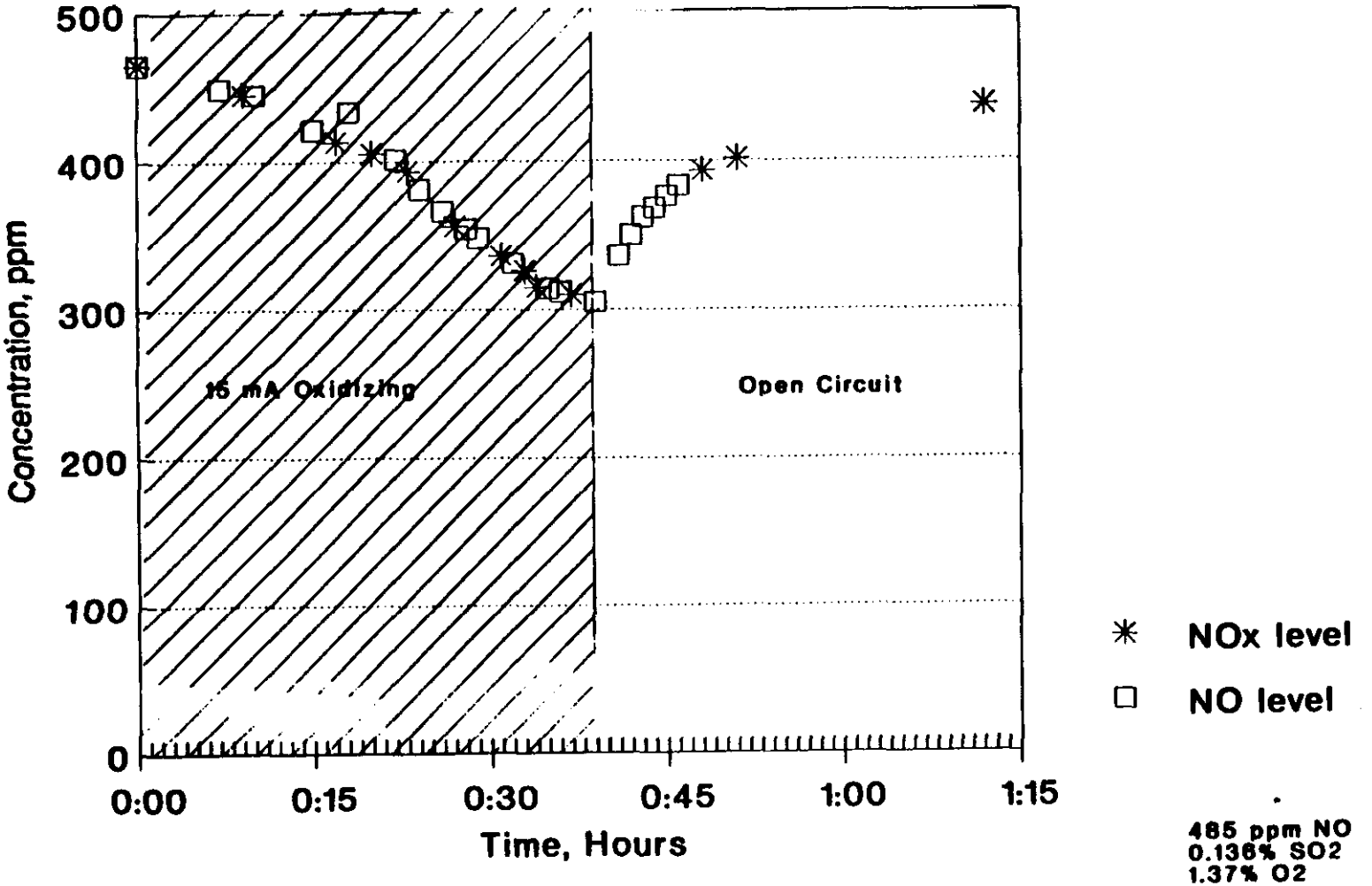


Figure V-9. 400 degrees C.

# NOx Study, Oxidizing Current

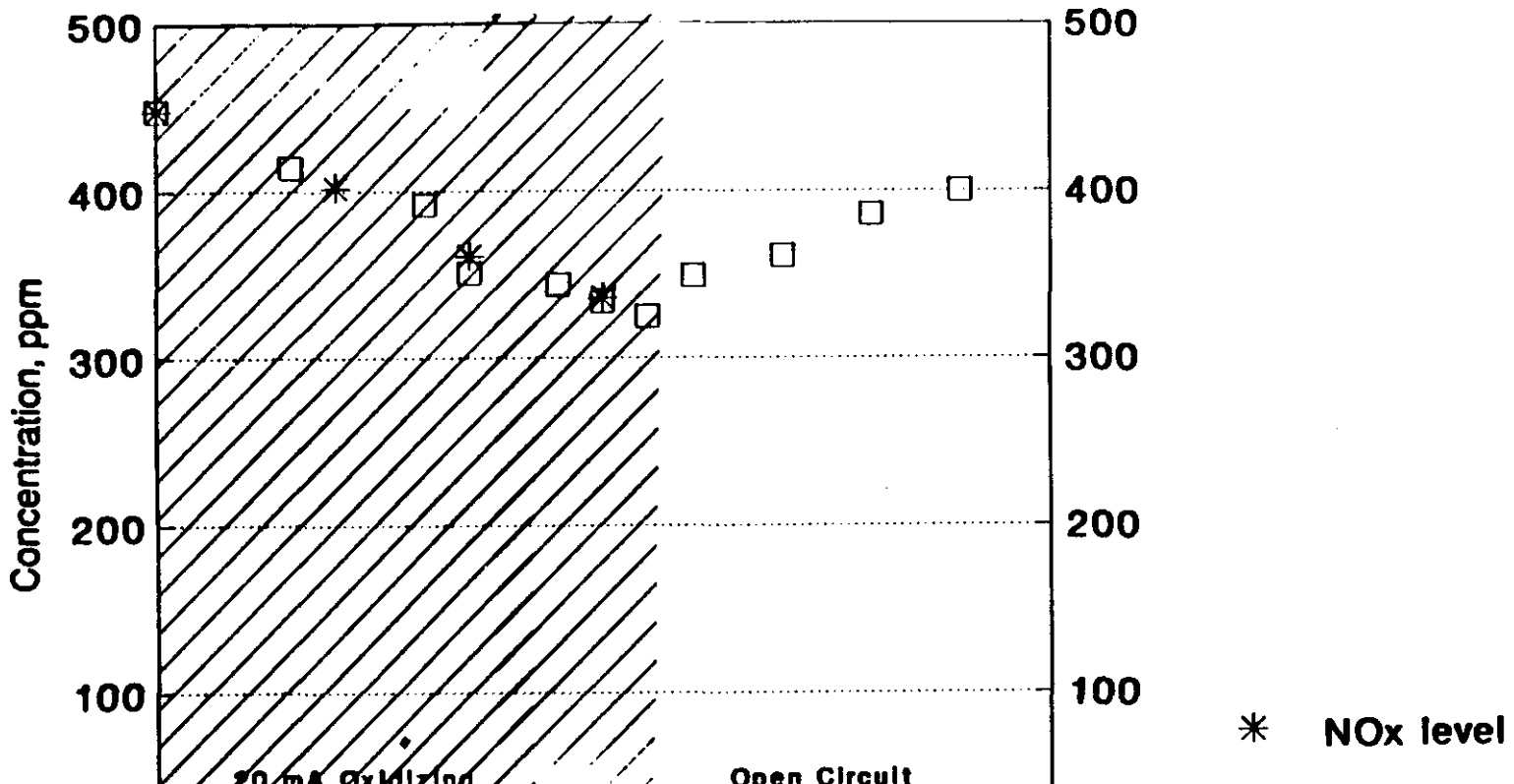


Figure V-10.

# NOx Study

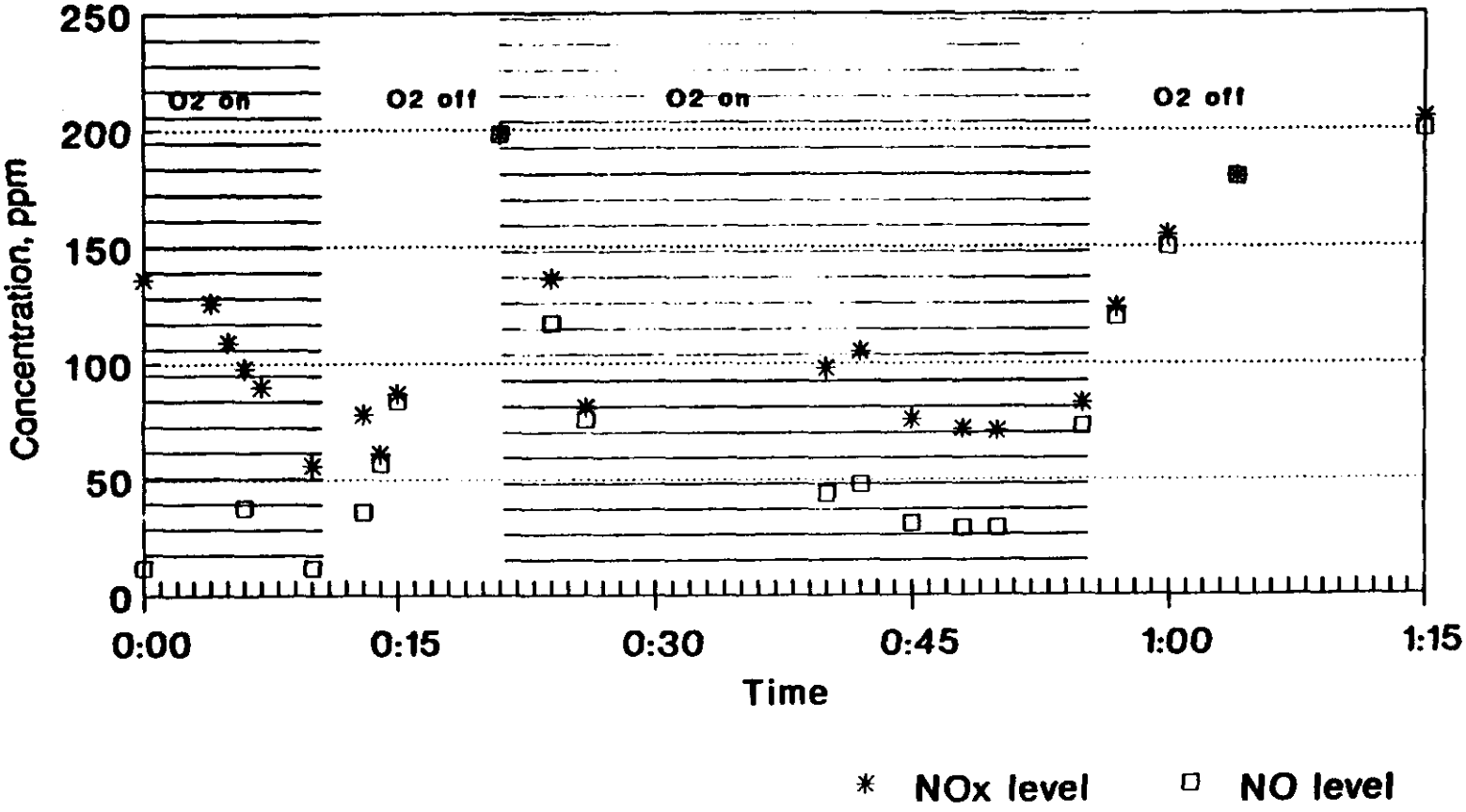


**Figure V-11. 400 degrees C.**
**50 ml/min of 567 ppm NO2 in N2**
**10 mA Reducing Current**

# NOx Study

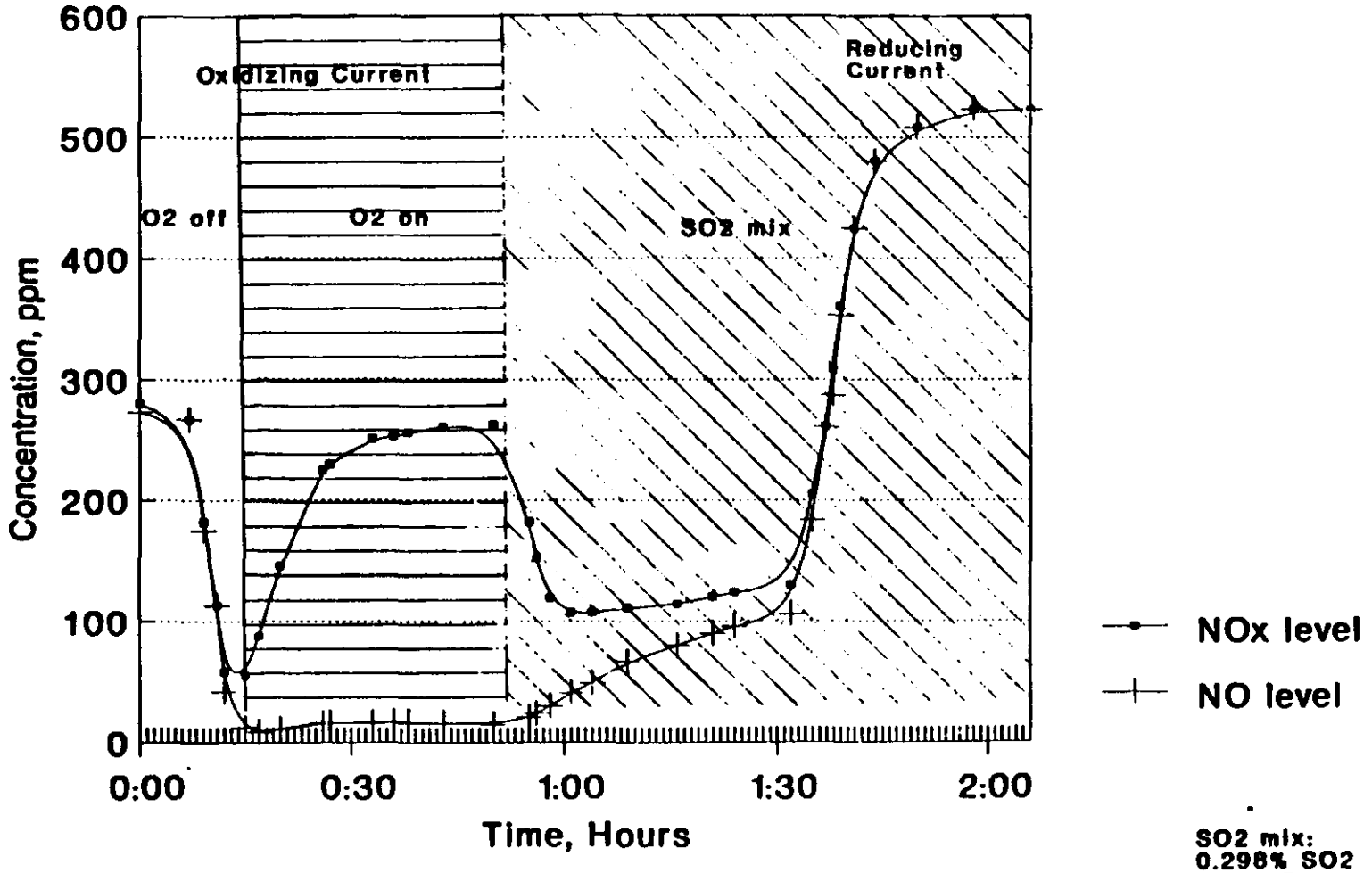


Figure V-12. 400 degrees C.
50 ml/min of 567 ppm NO2 in N2

SO2 mix:
0.298% SO2
3.01% O2
Balance N2
49 ml/min

# NOx Study, Oxidizing and Reducing Current

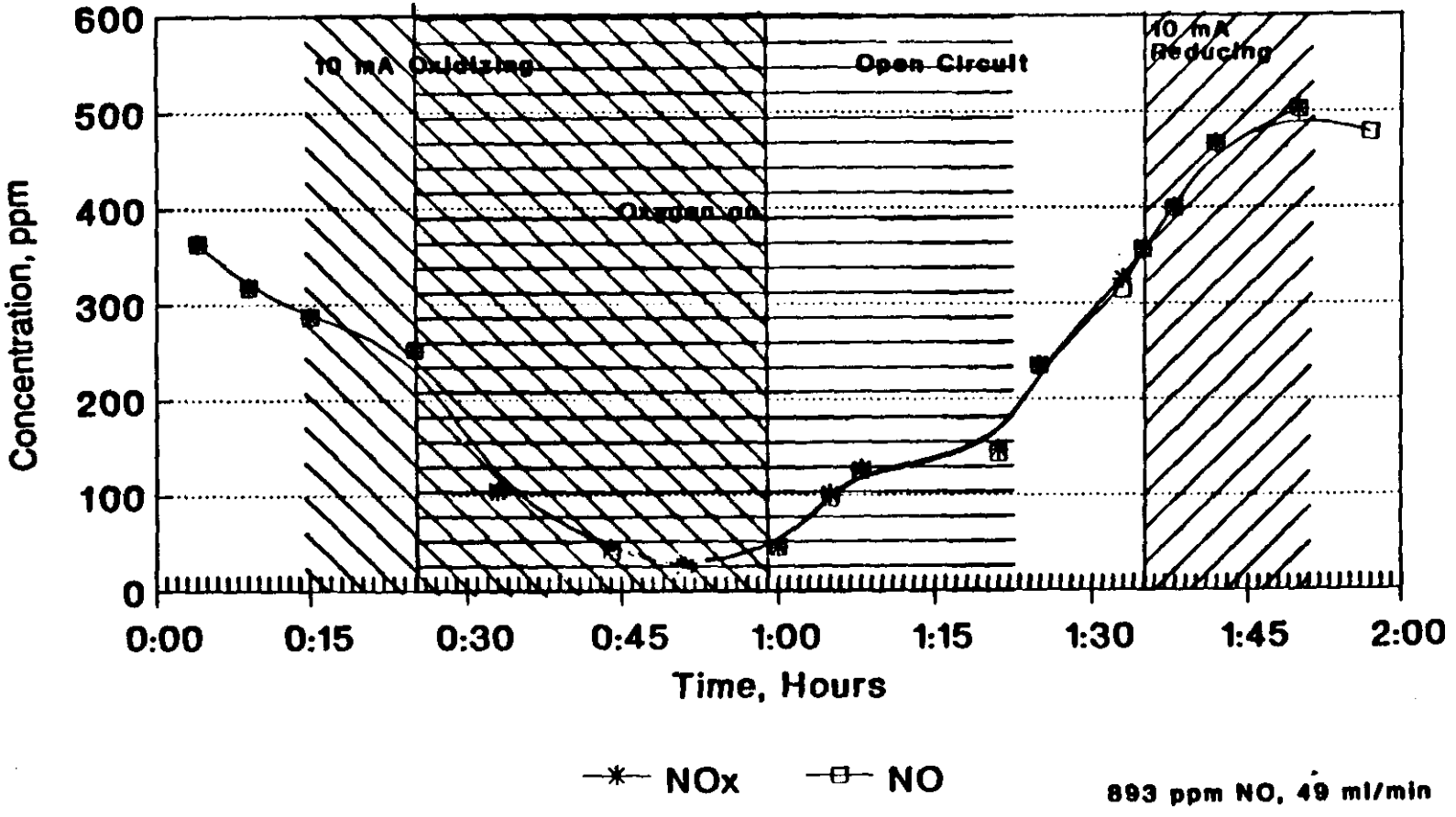


Figure V-13. 425 degrees C.

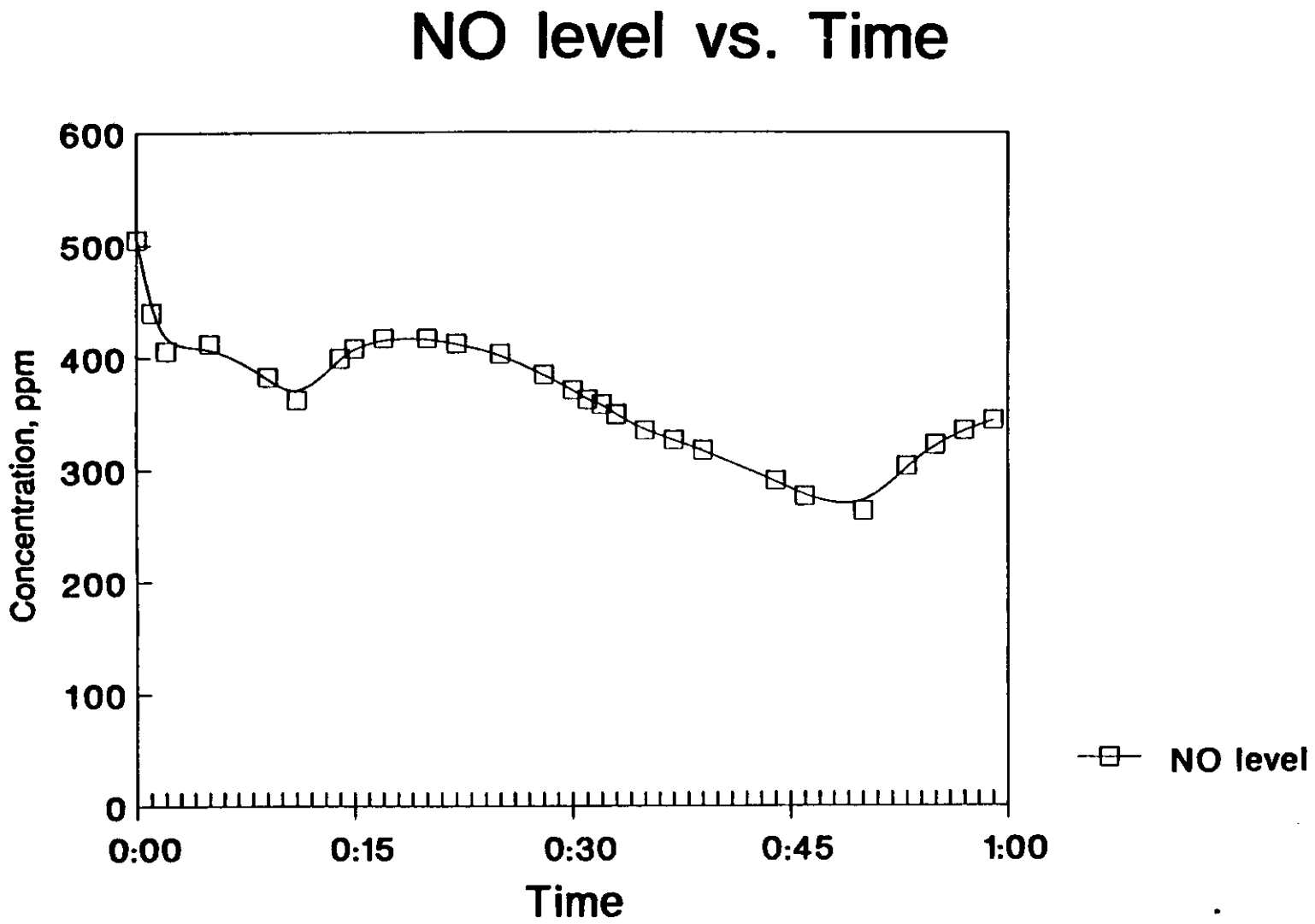


**Figure V-14.**
**Working Electrode • normal perovskite**
**Counter Electrode • large particles**

**Gas Mix to Working**
**47 ml/min 893 ppm NO in N2**
**44 ml/min 0.298% SO2, 3.06% O2 in N2**

# Potentiostatic Operation

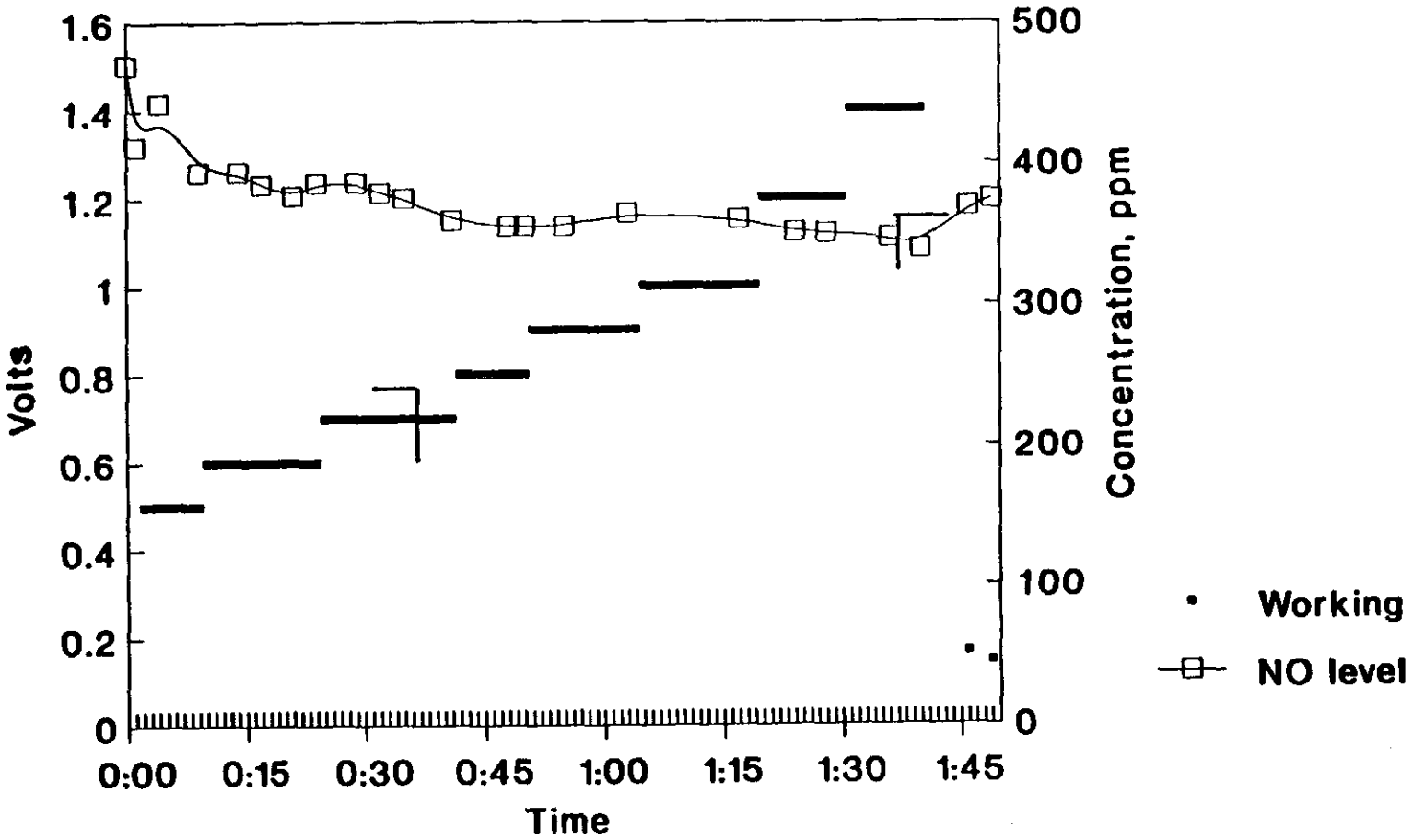


**Figure V-15.**
**Working Electrode = large particles**
**Counter Electrode = normal perovskite**

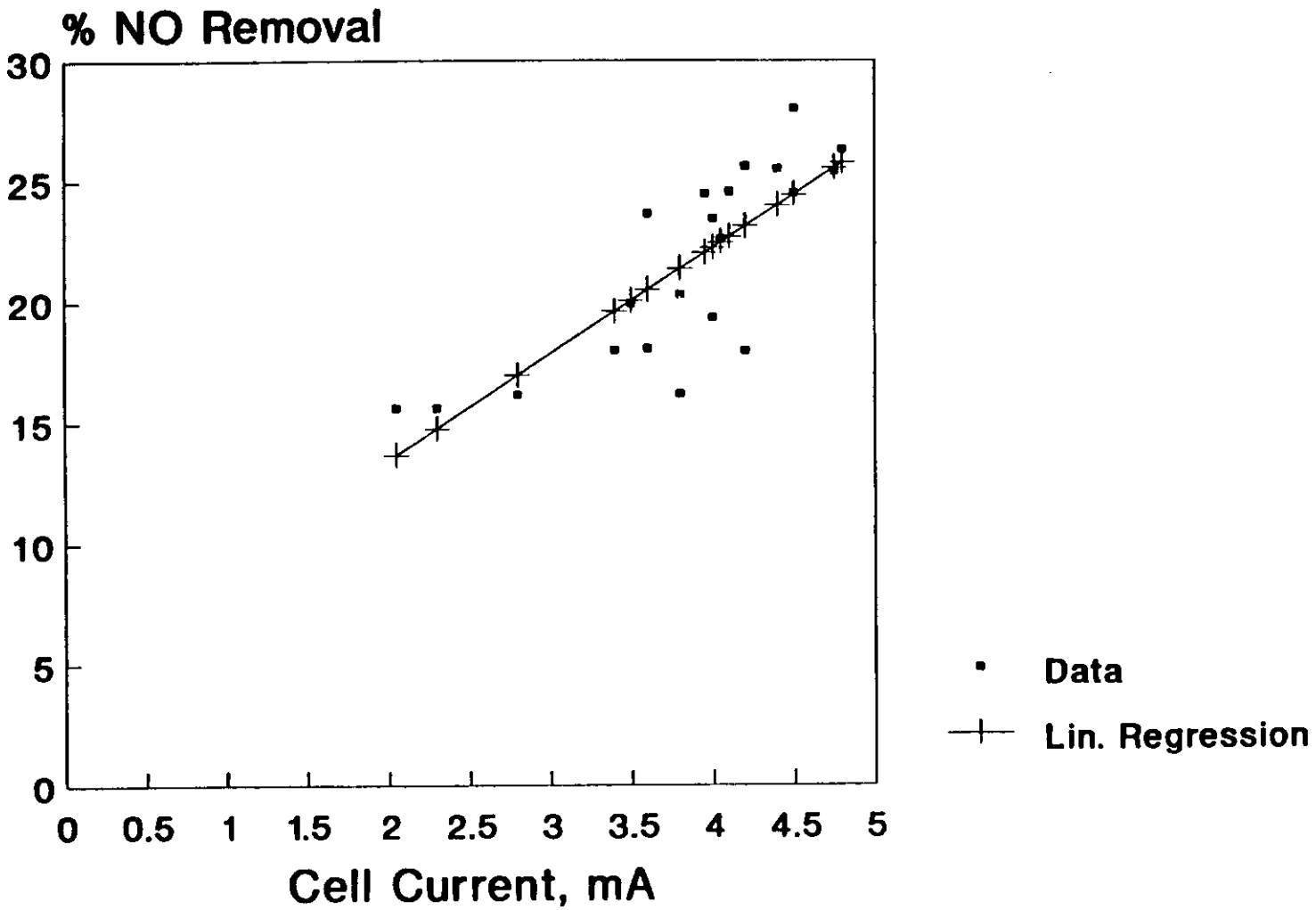
% NO Removal
30
25
20
15
10
5
0
0
0.5
1
1.5
2
2.5
3
3.5
4
4.5
5
Cell Current, mA
Data
Lin. Regression

Figure V-16.

# NO Removed vs. Current

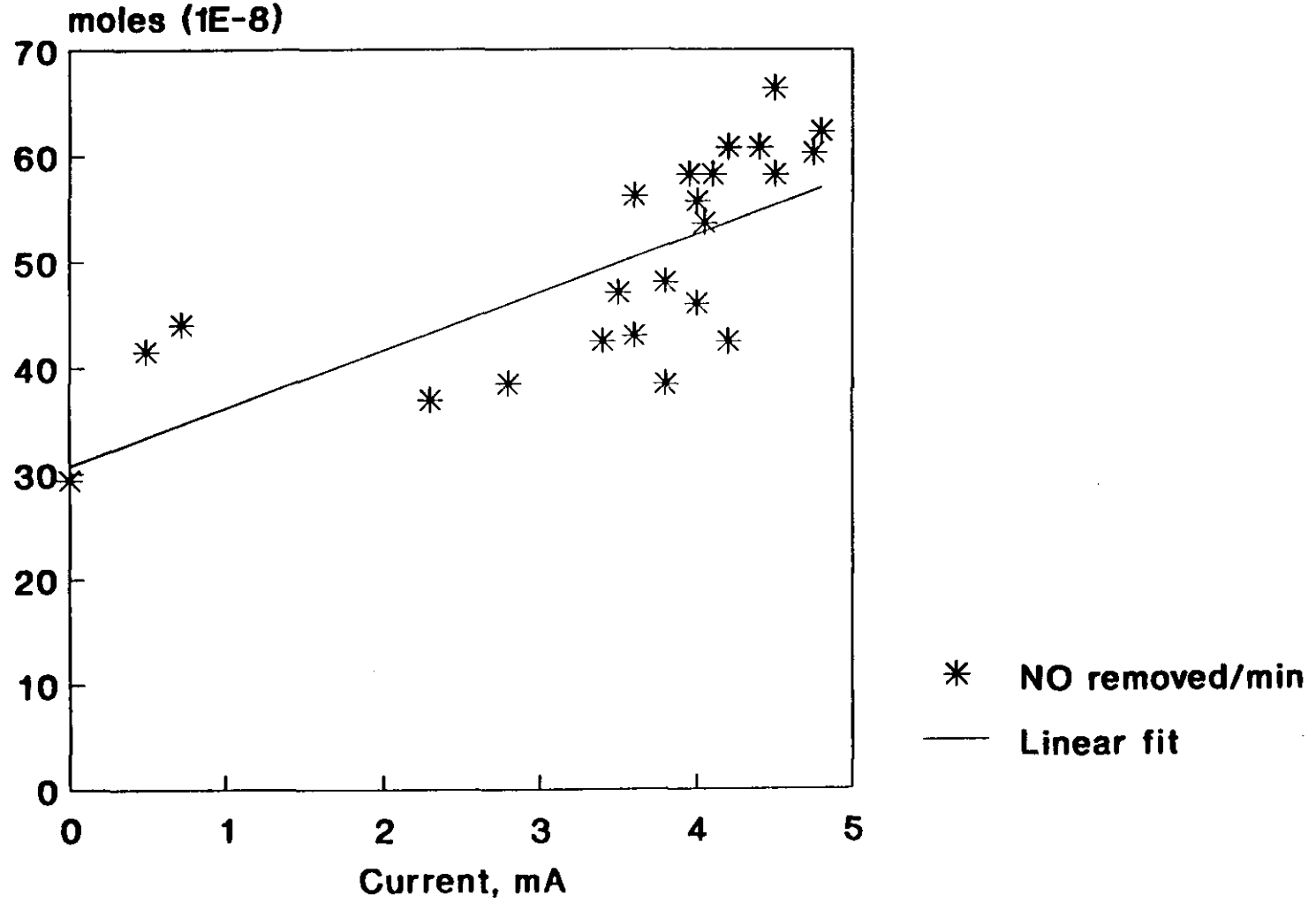


Figure V-17.

# Potential vs. Time

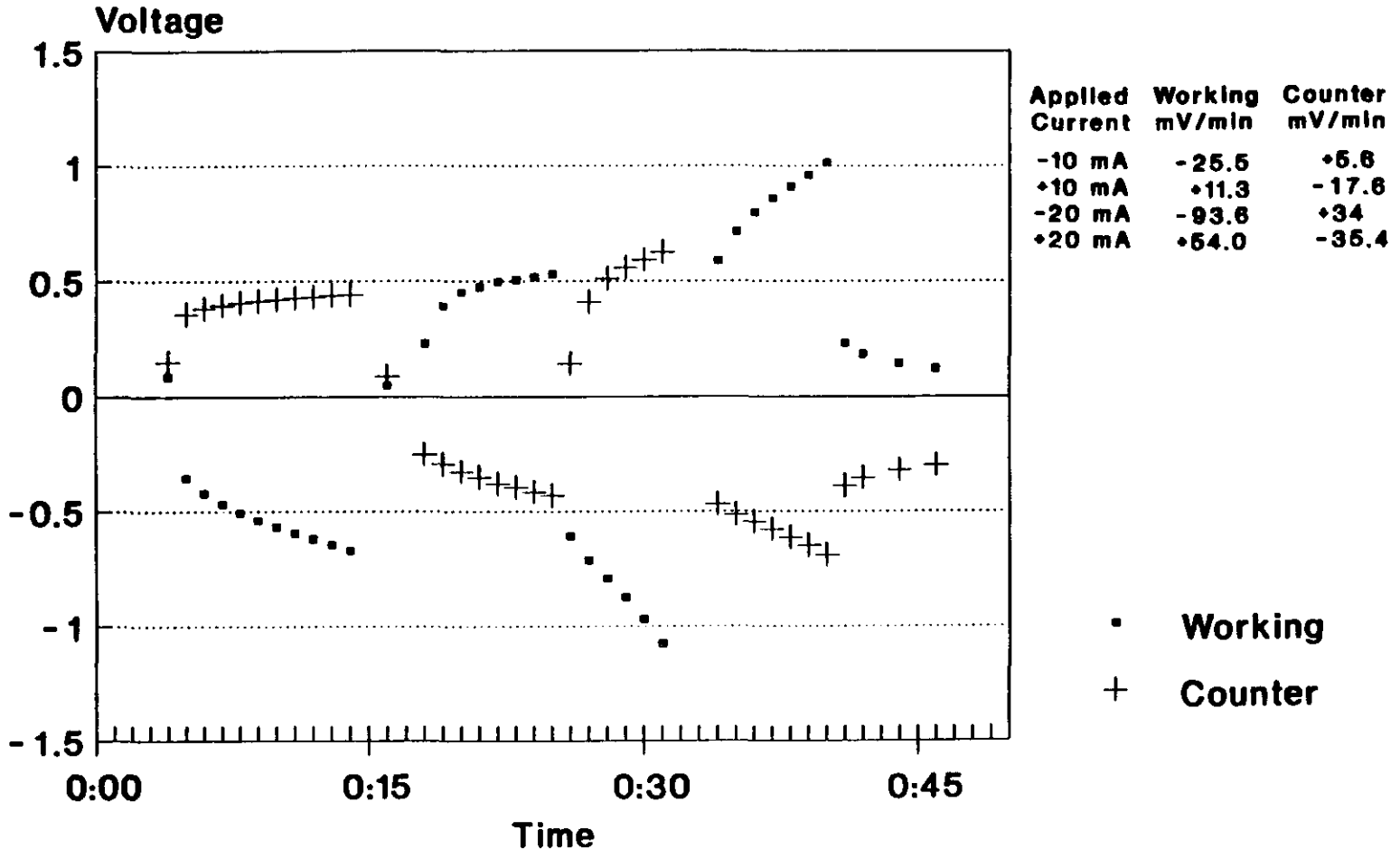


**Figure V-18. Electrode Response to I**
**Working Electrode - normal perovskite**
**Counter Electrode - large particles**

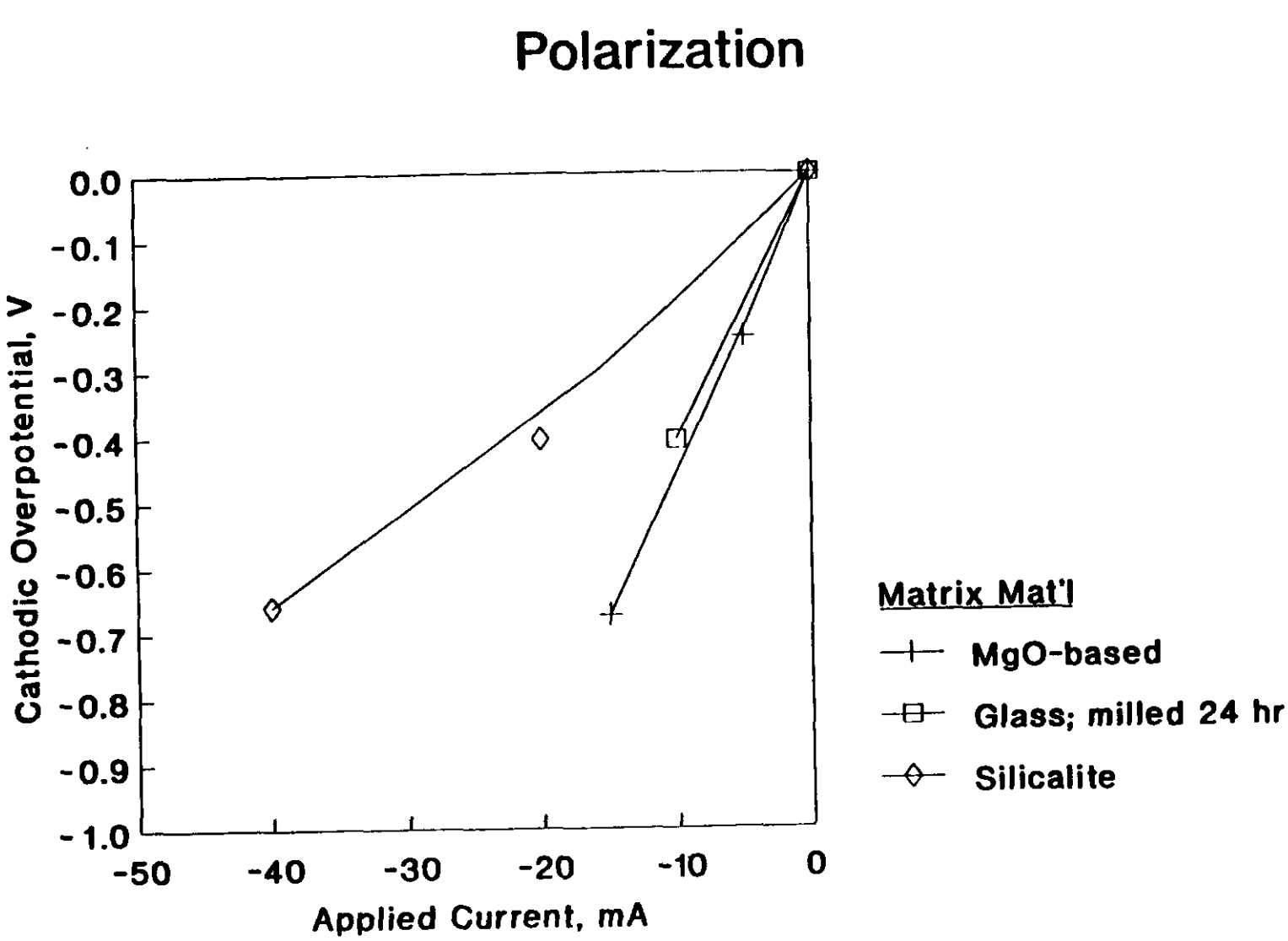


**Figure V-19. 400 degrees C.**
**MgO-based run had pre-oxidation catalyst**
**Other runs had no pre-oxidation catalyst**

# -20 mA Applied at 400 degrees C.

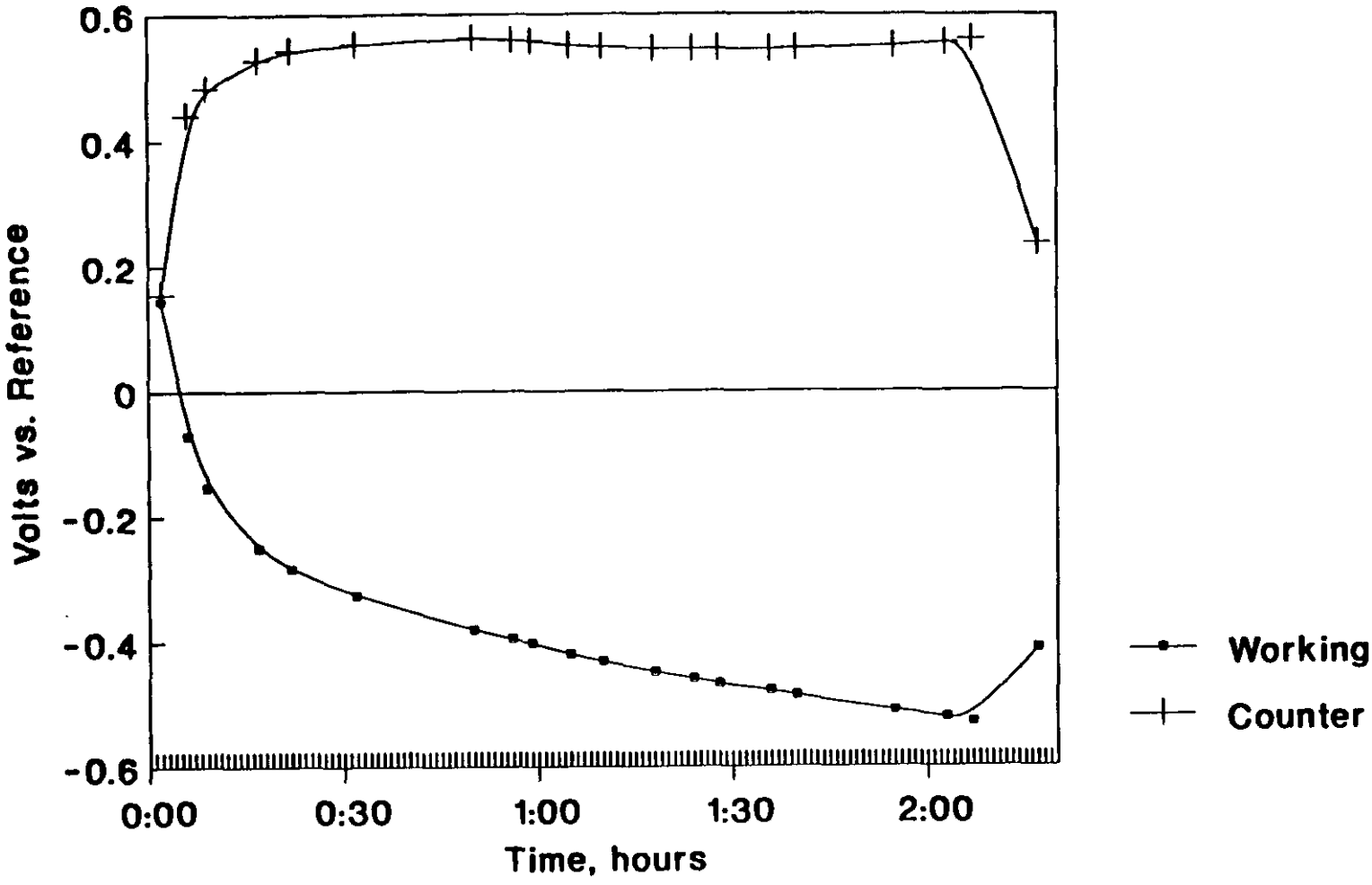


Figure V-20. Eight hours after start-up

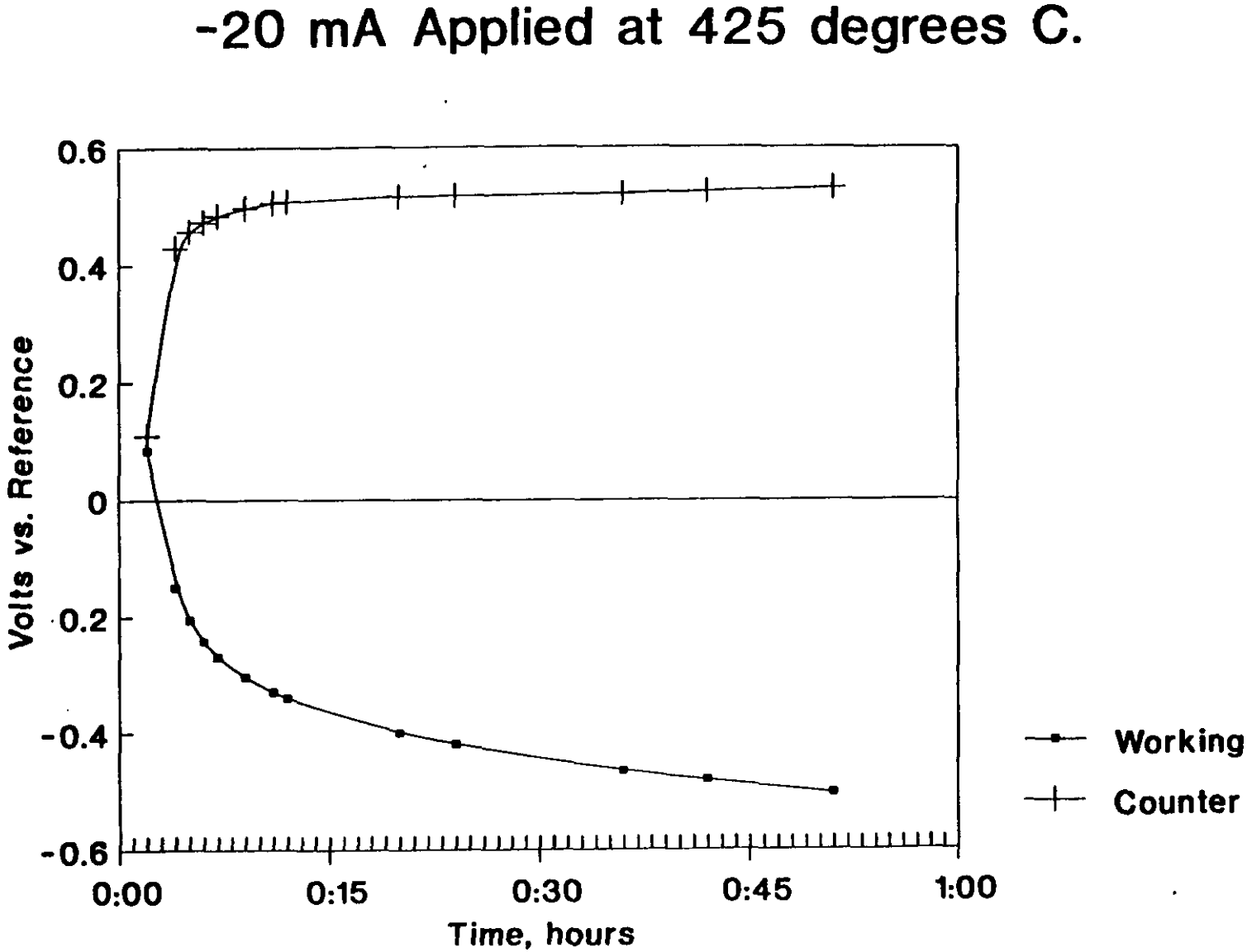


Figure V-21. Twenty-four hours old

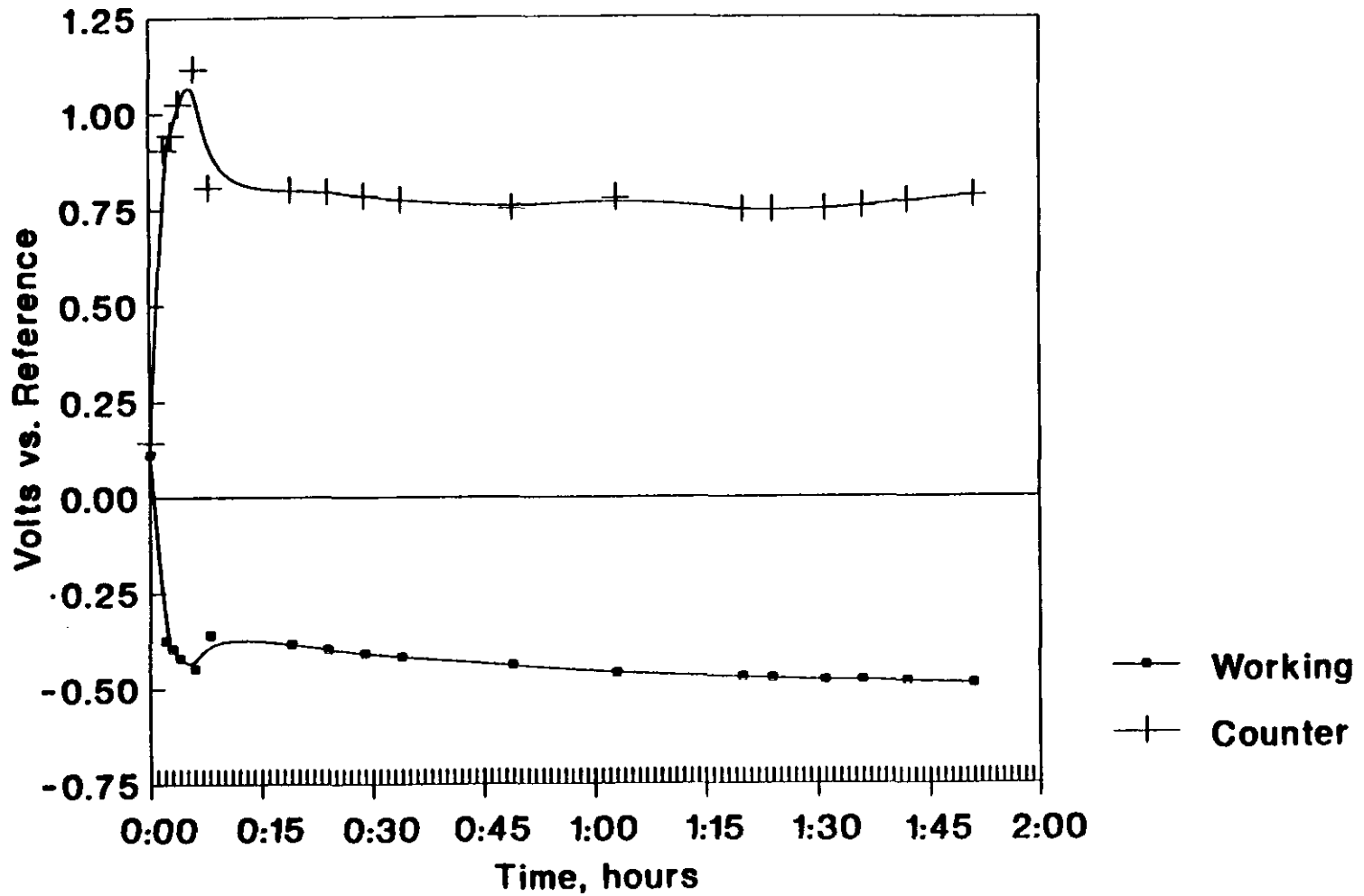


Figure V-22. -20 mA; then -10 mA

# Overpotential vs. Time

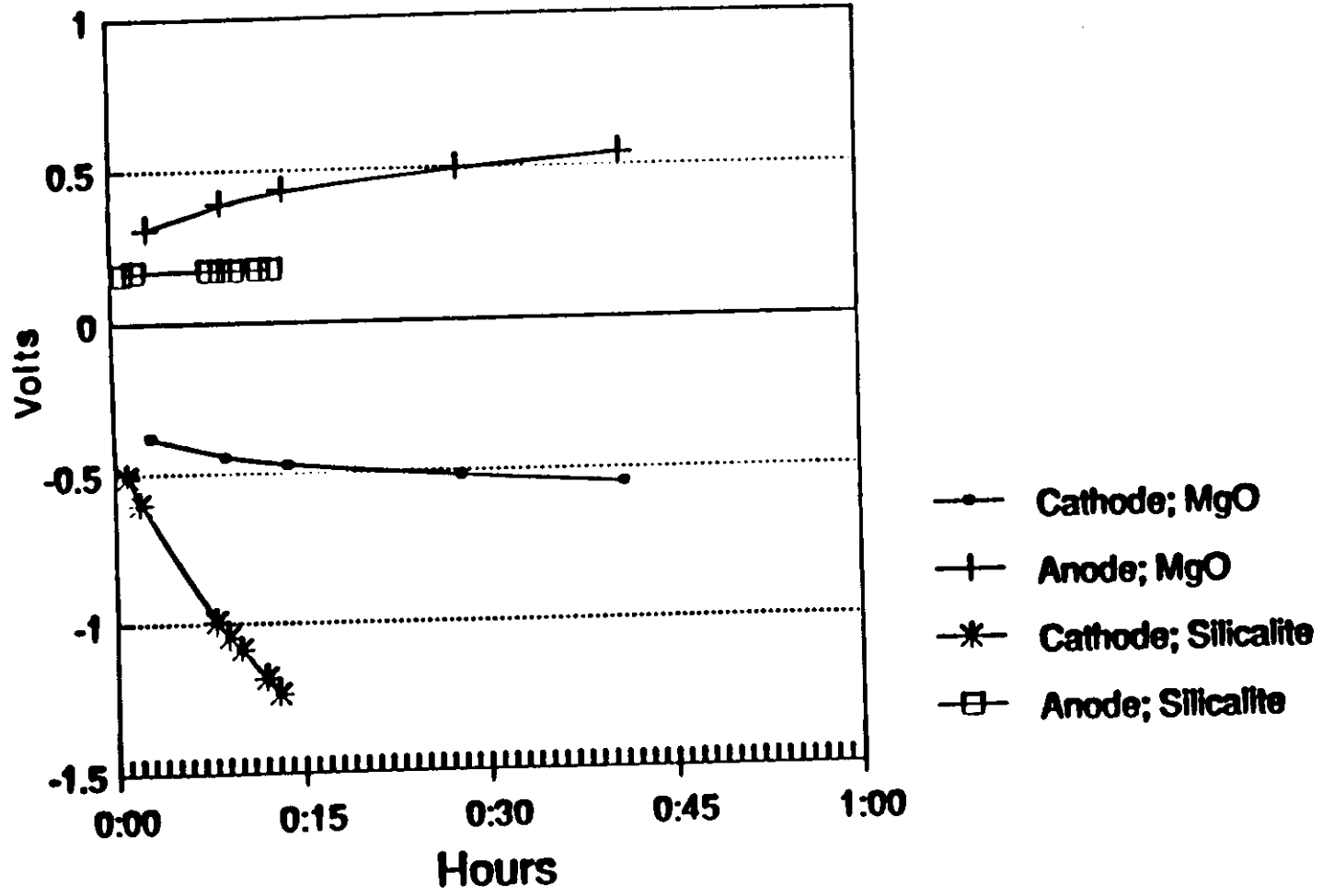


Figure V-23. -10 mA Applied to Cathode

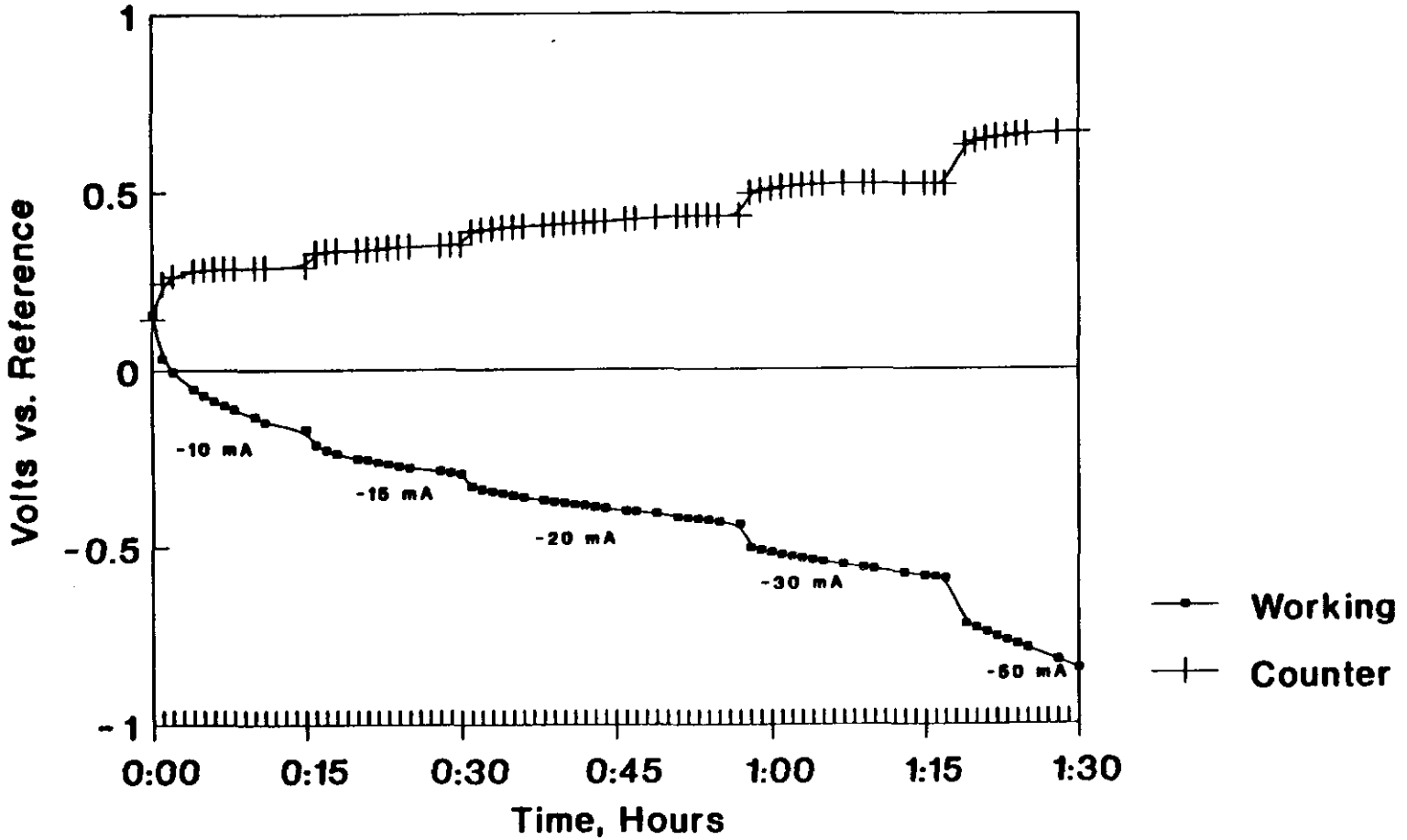
Potential vs. Time
Silicalite membrane
Volts vs. Reference
1
0.5
0
-0.5
-1
-10 mA
-15 mA
-20 mA
-30 mA
-60 mA
0:00
0:15
0:30
0:45
1:00
1:15
1:30
Time, Hours
Working
Counter

Figure V-24.

# Overpotential vs. Time

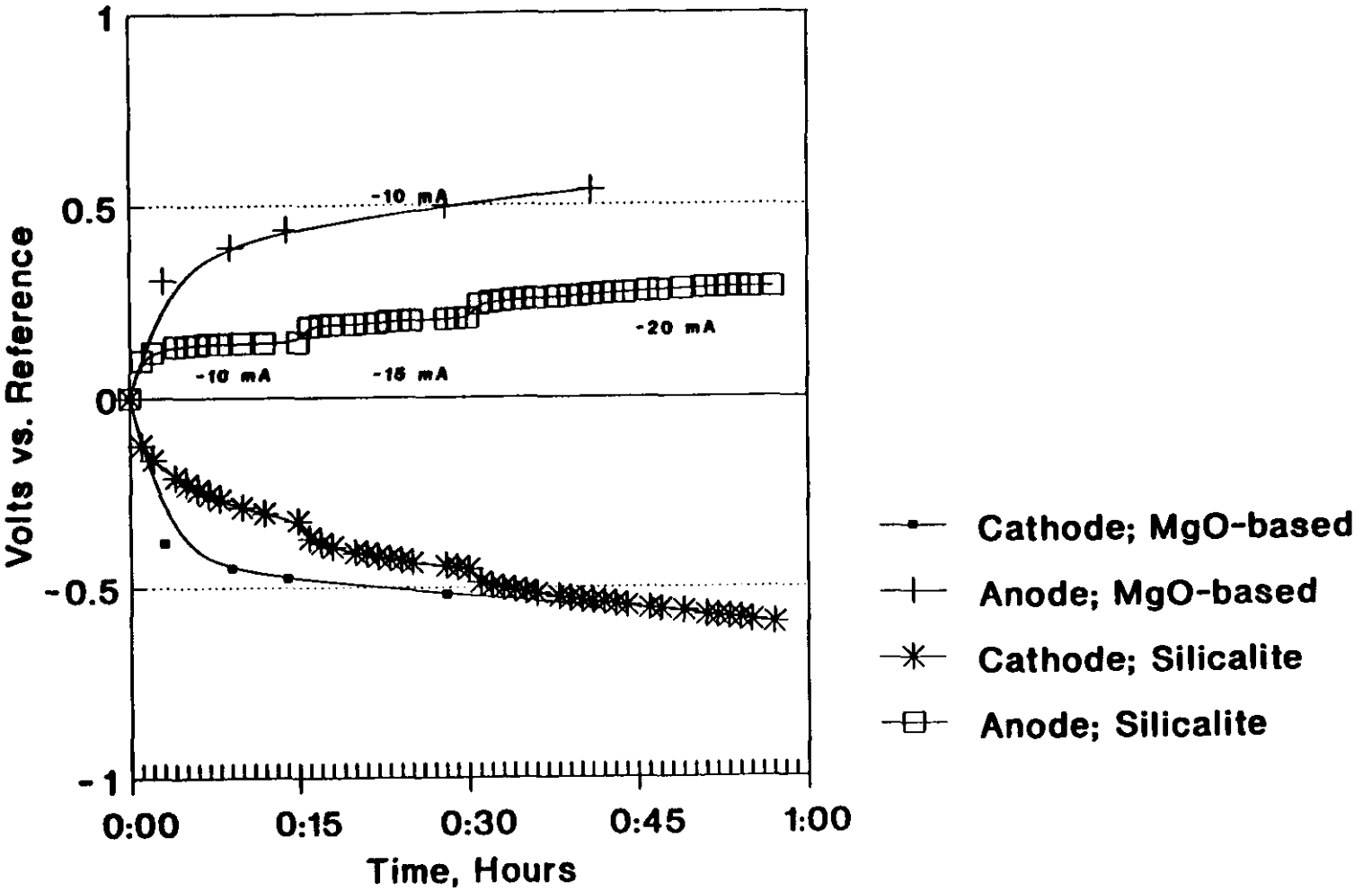


Figure V-25.

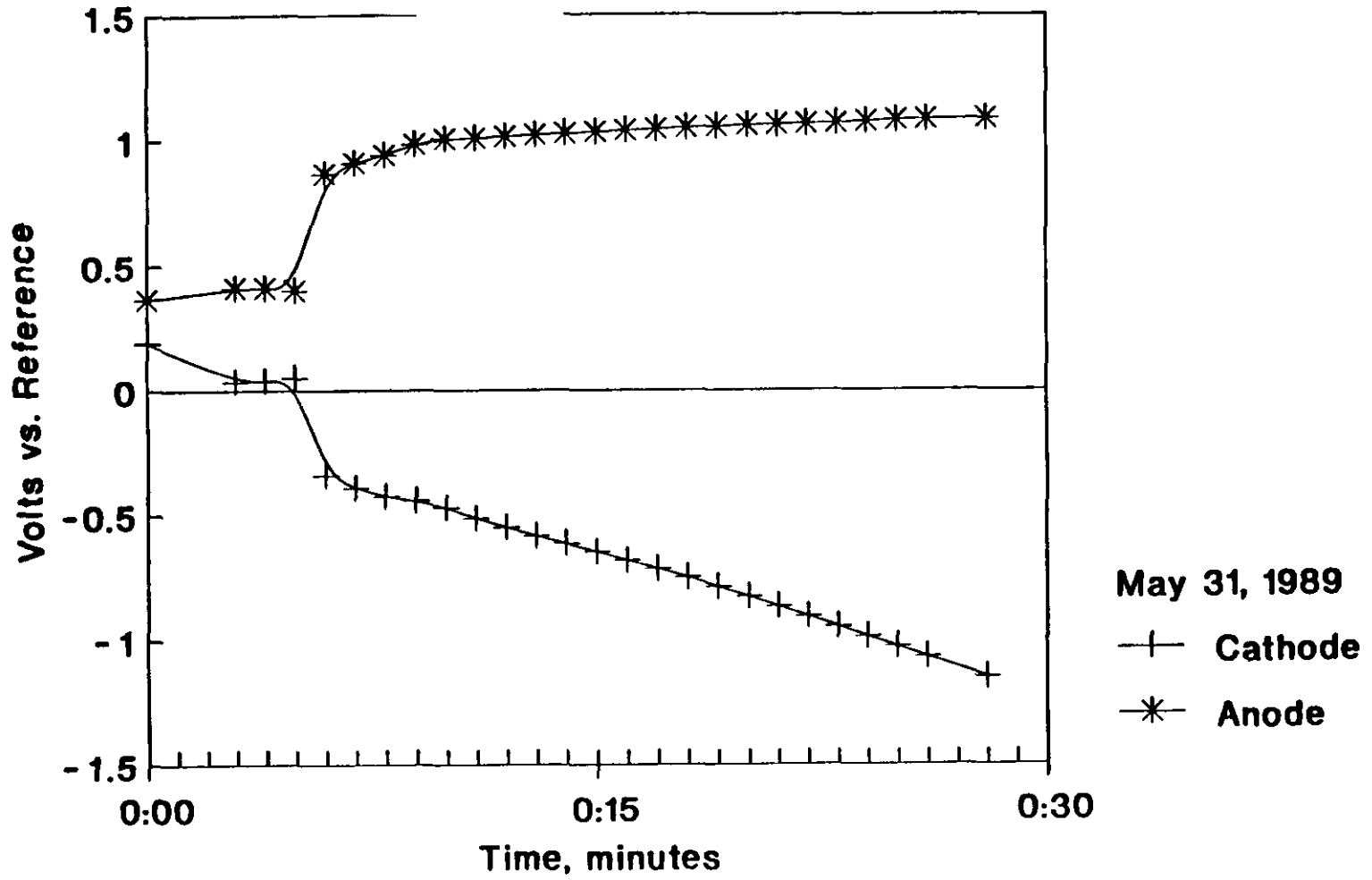


Figure V-26. 325 deg. C

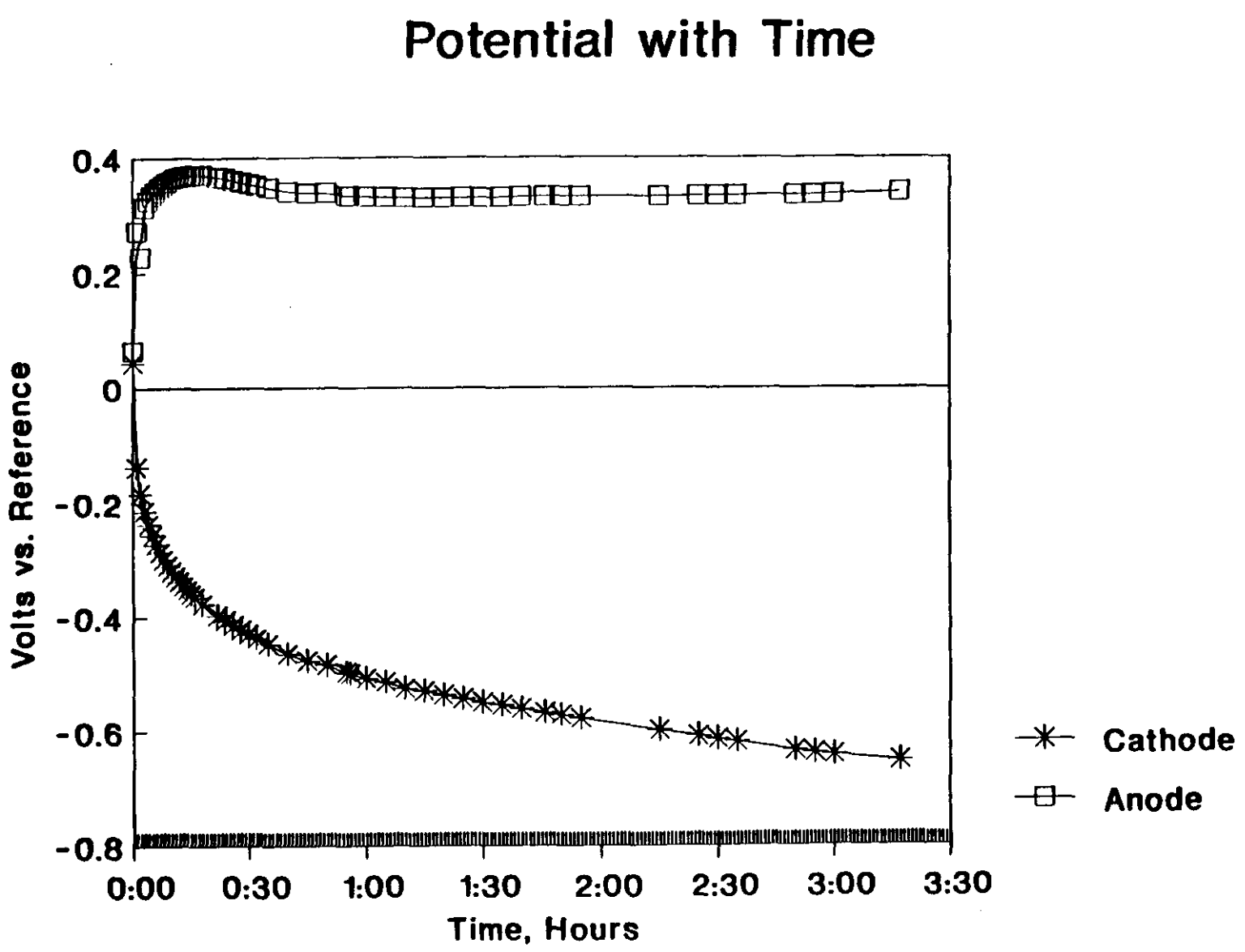


Figure V-27. 400 degrees C. and -20 mA

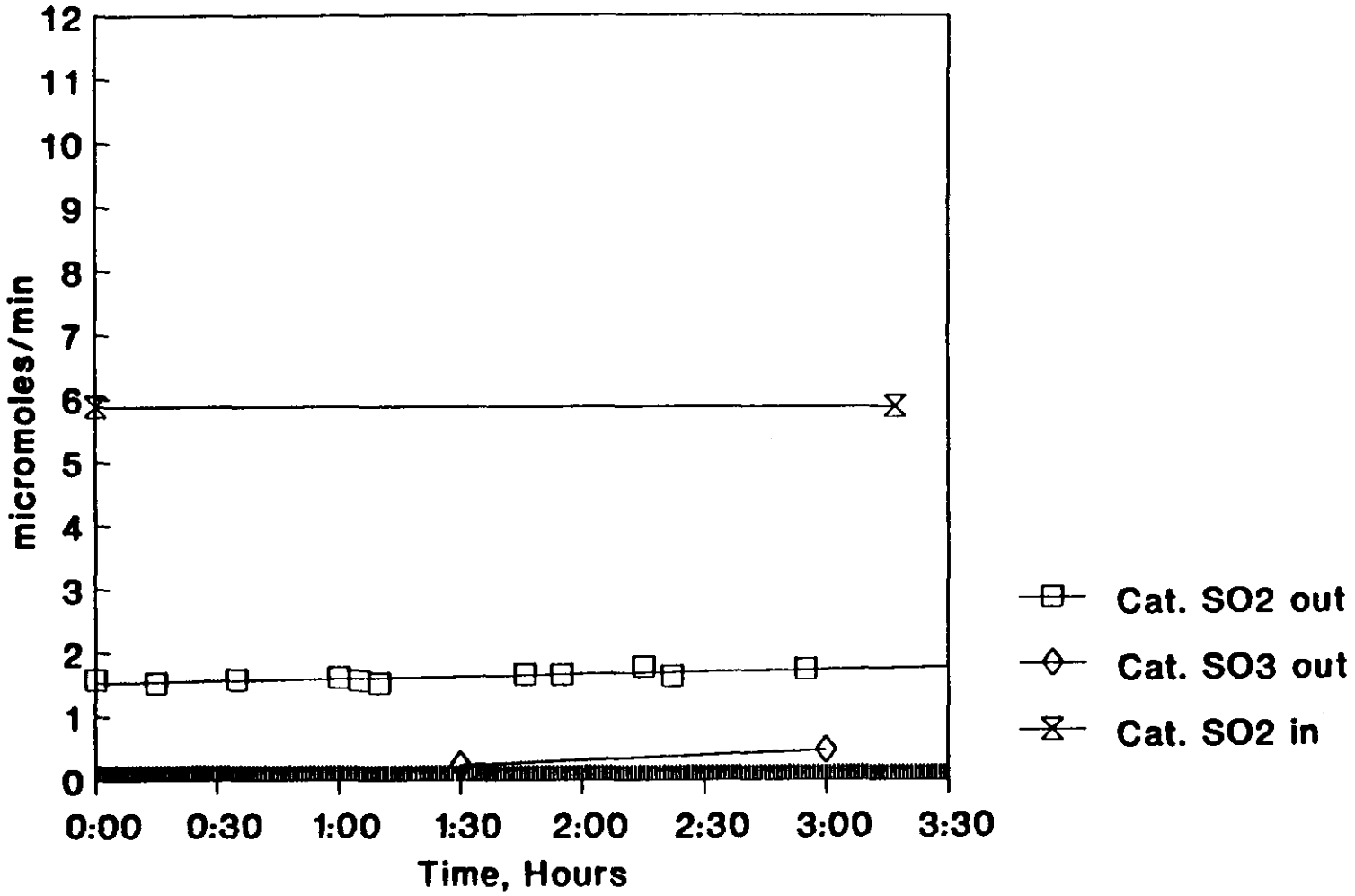


Figure V-28. 400 degrees C. and -20 mA

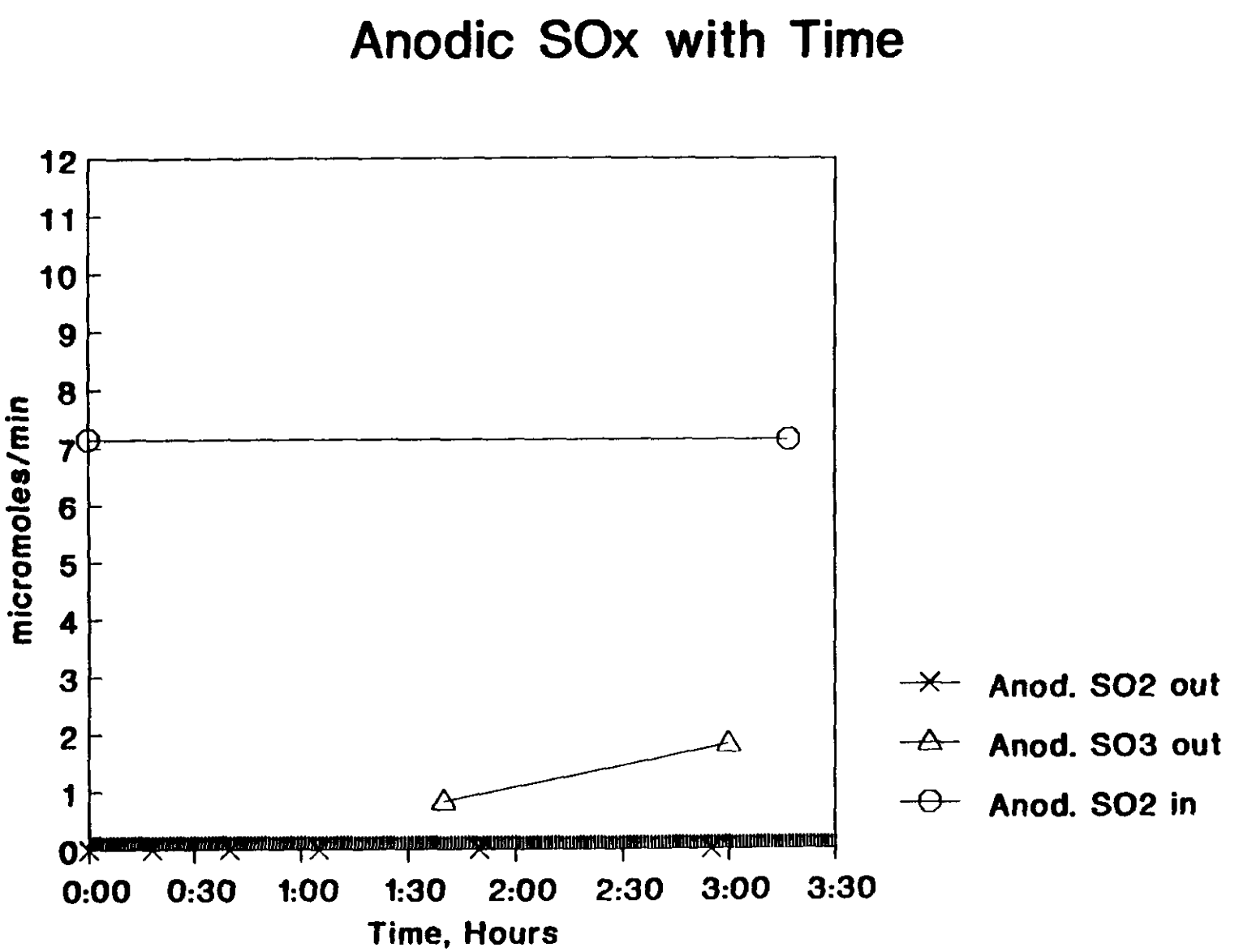


Figure V-29. 400 degrees C. and -20 mA

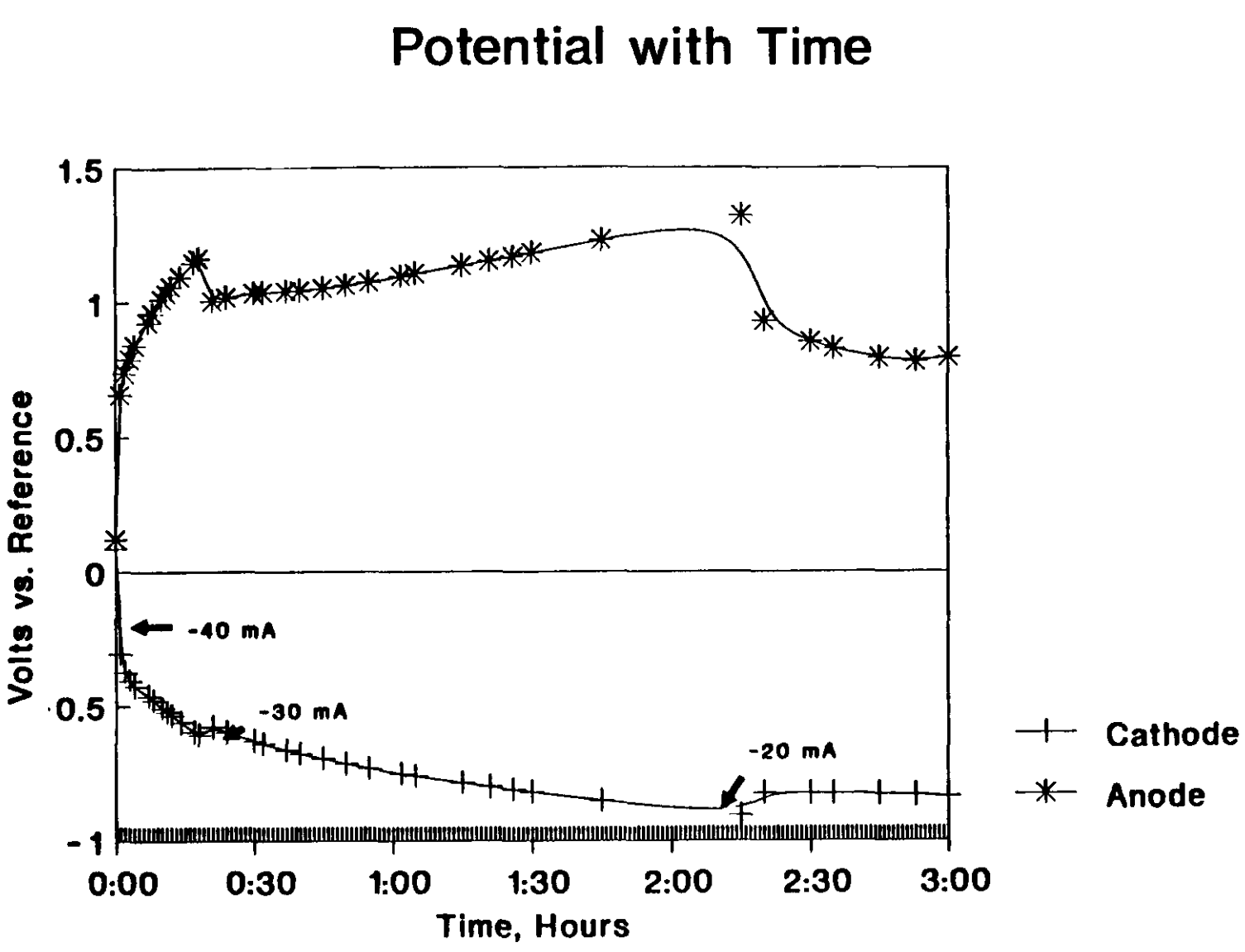


Figure V-30. 400 degrees C.
Current as shown.

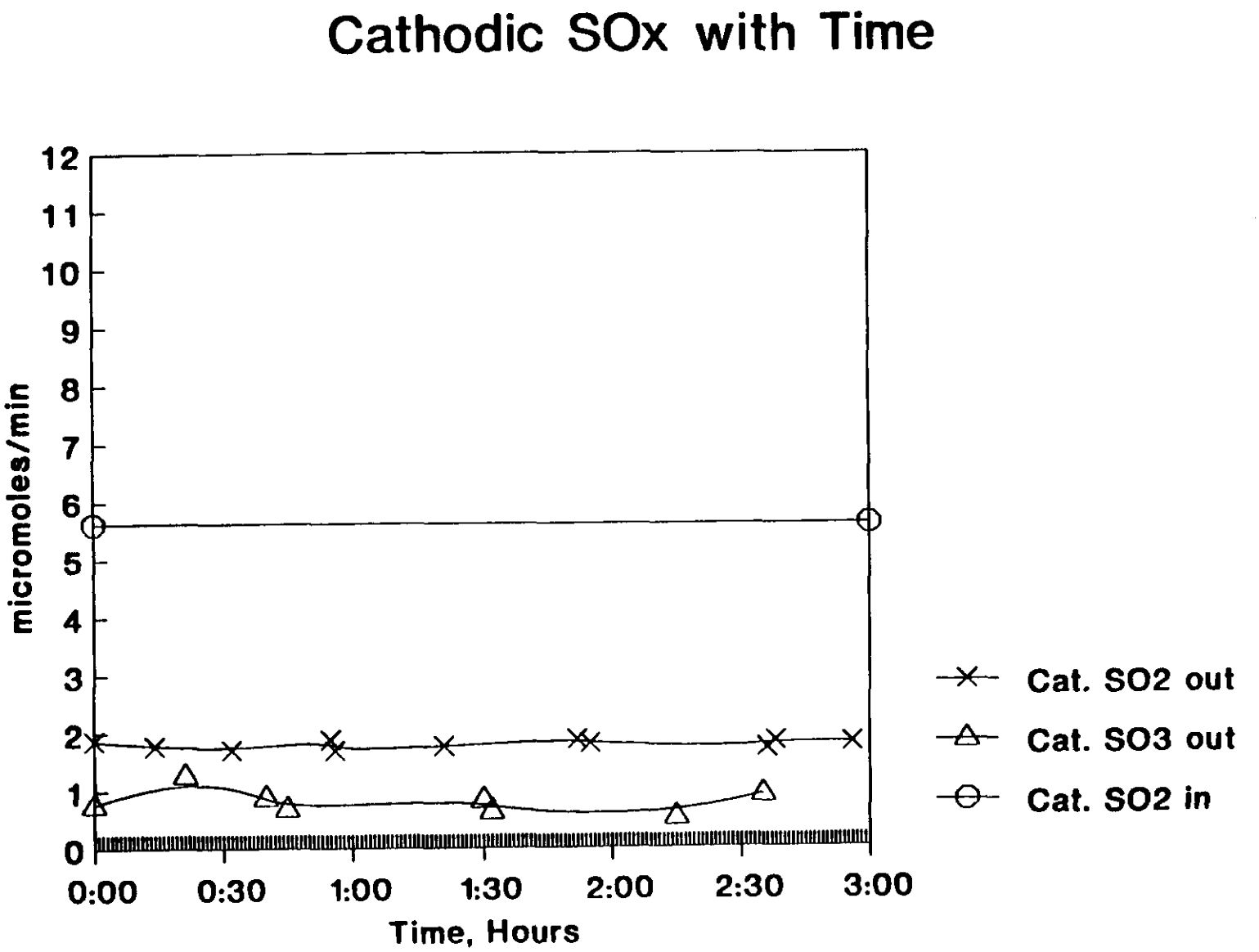


Figure V-31. 400 degrees C.

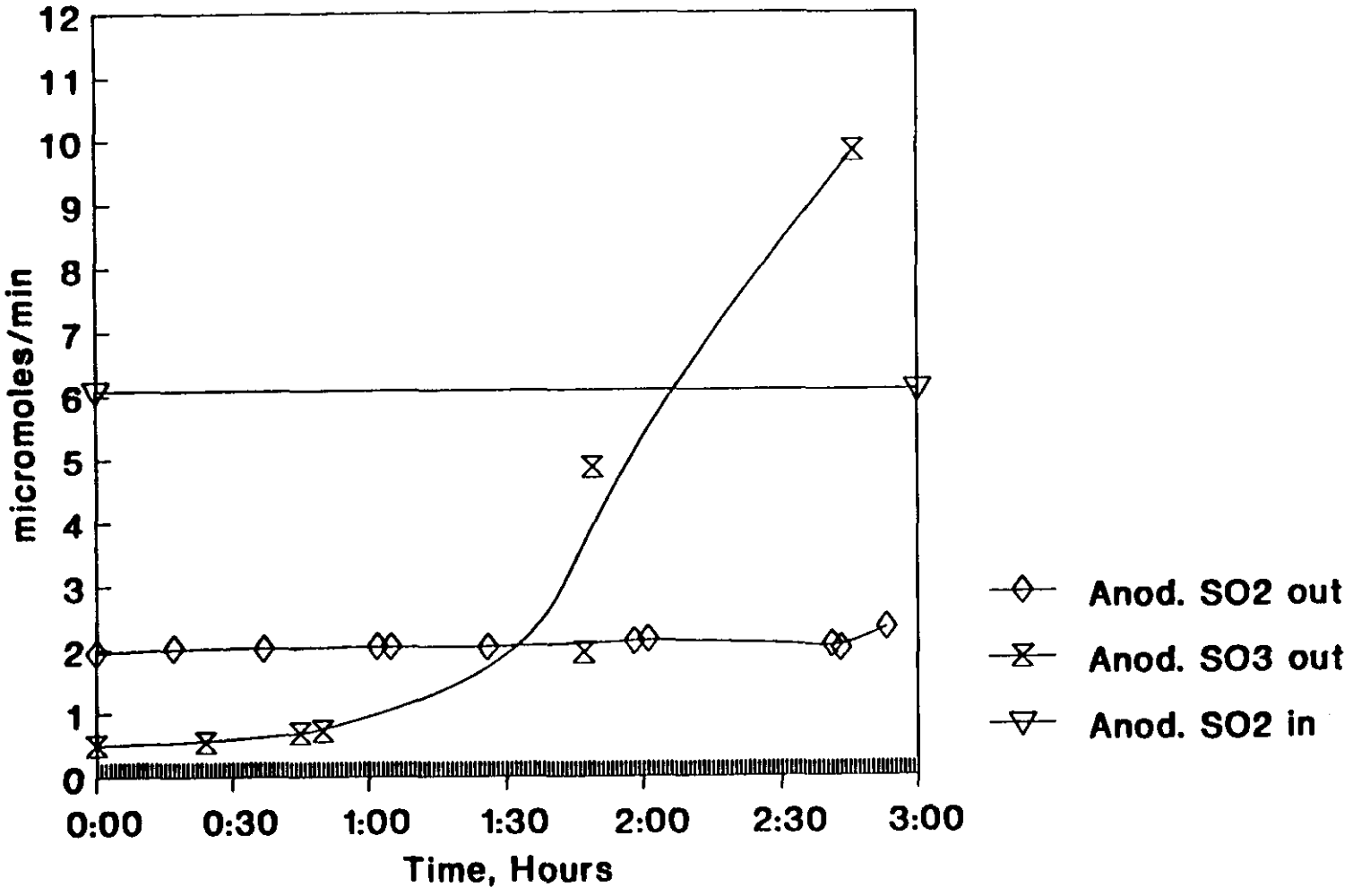


Figure V-32. 400 degrees C.

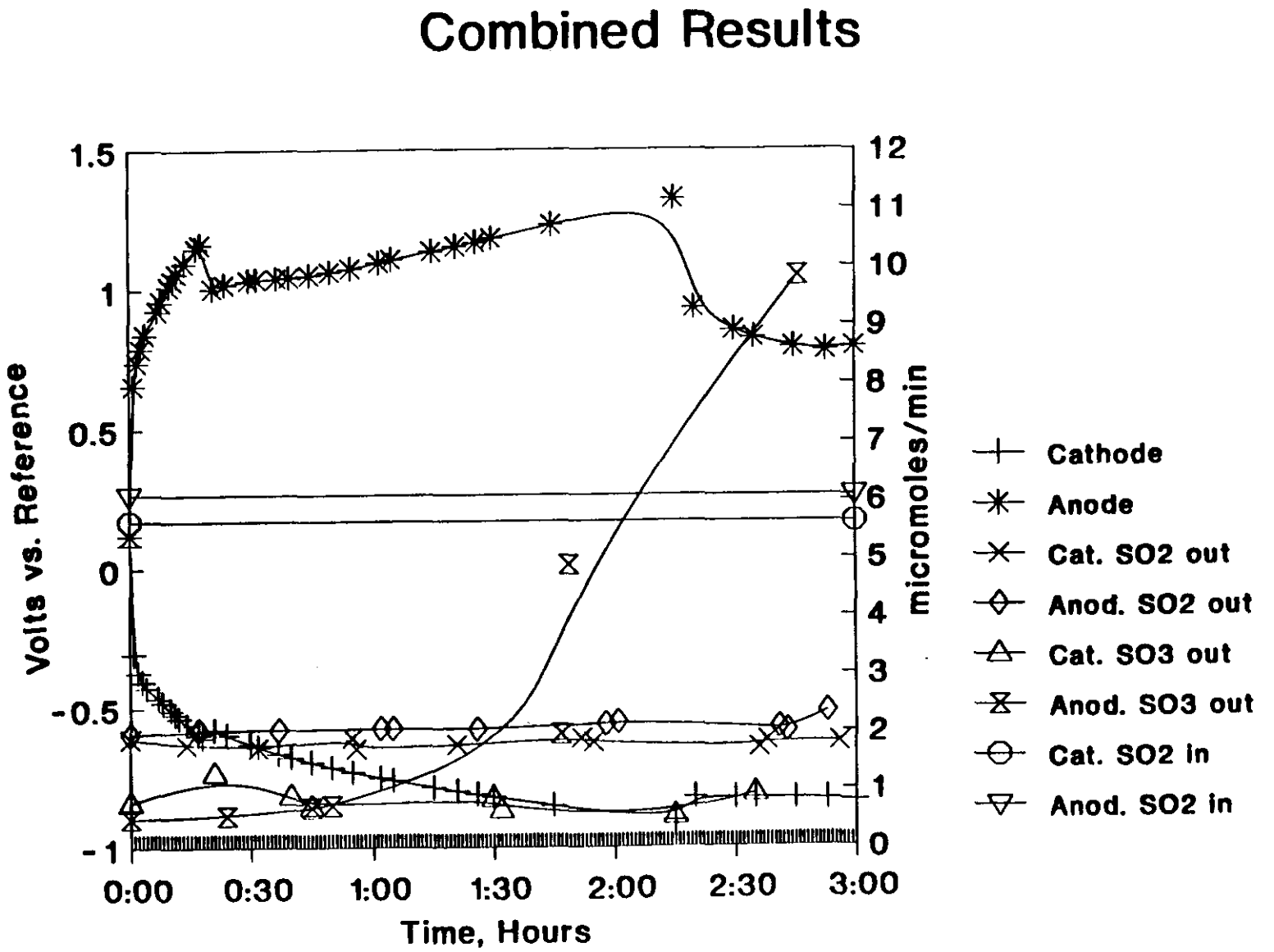


Figure V-33. 400 degrees C.

## VI. Process Economics

The outlook for economic viability, at least for $SO_x$ treatment, is extremely good. This prediction is based on a combination of results obtained in this study and existing fuel cell technology.

The analysis is based on a 500 $MW_e$ power plant burning a 3.5% sulfur coal in 20% excess air. The heating value of the coal is assumed to be 10,000 BTU/lb with a thermodynamic efficiency of 35%. The feed rate of the coal is therefore 61.1 kg/sec, and the composition of the resultant flue gas stream is 0.24% $SO_2$, 3.5% $O_2$, 17% $CO_2$ in $N_2$. The total flow rate of the stream is 28,000 gmol/sec, and at 350°C, the volumetric flow rate is approximately 1430 $m^3$/sec. It is also assumed that 90% of the $SO_x$, or 60.5 moles/sec, must be removed. By Faraday's law, 60.5 moles/sec at a stoichiometry of 1 mole per 2 faradays corresponds to a current equivalent to 11,677,000 Amps. Assuming an operating current density of 0.05 A/$cm^2$, which the free electrolyte kinetic studies proved to be attainable, the active electrode is calculated as 23,400 $m^2$, (252,000 $ft^2$).

The design of commercial units are envisioned to be similar to the molten carbonate fuel cell, where each individual cell layer is a 1.2m square. This means approximately 16,200 cells are needed. If each individual layer is 0.5 cm thick, then 16 units, each 5 m in height and containing 1,000 individual cells, in series electrically, are required. The installed capital costs, including piping, controls, and electrical, were estimated from current

estimates of molten carbonate fuel cell stack costs, at $30.00/ft$^2$ Therefore, the overall installed cost of the EMS units is $7.6MM. This cost is considerably lower than that typically found for ambient-temperature electrolytic cells primarily due to the simple construction and ceramic components.

The majority of operating cost is for power to drive the cells. At high current densitites, as would be used in practice

$$i = i_o \, e^{-\eta n f} \qquad (62)$$

At the cathode,

- $i$ = current density, A/cm$^2$
- $i_o$ = exchange current density, A/cm$^2$
- $\eta$ = overpotential, volts
- $n$ = moles electrons/mole reaction
- $f$ = F/RT
- $F$ = Faraday's constant, 23062 cal/volt
- $R$ = gas constant, 1.987 cal/mol/K
- $T$ = absolute temperature, K

where the overpotential is negative. For a design current density of 0.050 A/cm$^2$, the kinetic overpotential will be about 30 mV, if the exchange current density, $i_o$, approaches that found in the free electrolyte tests, $3.0 \times 10^{-2}$ A/cm$^2$. An equivalent kinetic overpotential can be presumed at the anode; concentration overpotential at each electrode is less than 0.1V.

The polarization due to the ionic transport in the supported electrolyte is not easily calculated. It should be noted, however, that the molten carbonate fuel cell, configured nearly identically

to the EMS, routinely generates current densities greater than 0.20 $A/cm^2$. These current densities are achieved with less than 0.15V overpotential including concentration polarization. At our design level of 0.050 $A/cm^2$, the total voltage demand will be less than 0.5 V. At this voltage, with the current calculated directly for stoichiometry, the power duty is 5840 kW. At a rate of $0.05/kWh, the operating cost is estimated to be 0.6 mils/kWh. The labor rate is estimated to be about 0.1 mils/kWh. Therefore, the overall operating costs are approximately 0.7 mils/kWh.

## VI. Conclusions and Recommendation

The electrochemical membrane cell has been taken from concept to operational bench-scale status. The chain of chemical reactions observed in free pyrosulfate electrolyte have been proven out in the membrane cell, operating at steady-state. The removal of $SO_x$ from simulated flue gas occurs stoichiometrically at a rate of 2 Faradays per mole down to levels of 40 ppm $SO_x$. The generation of concentrated $SO_3$ at the other side of the membrane is likewise stoichiometric, thus producing a salable product at steady-state.

The components developed to date include:

- Porous, gas-diffusion, ceramic electrodes, devoid of precious metals;
- Electrolyte mix, melting below 300°C, composed of low-cost commercial reagents;
- Matrix materials of glass or common ceramics

In order to meet the projected capital cost, the operating current density must be improved to 50 $mA/cm^2$. This is achievable through the mass transfer, kinetic and ionic transport resistances, but the interfacial area between electrode and electrolyte must be significantly enhanced. This, in turn, requires a membrane with increased electrolyte retention to avoid electrode pore flooding.

Nitrogen oxide removal was found in free electrolyte, but in full-cell tests, occurred only under oxidizing current conditions. Several reaction paths are possible, but the fate of the nitrogen oxides is as yet unknown.

Future work must focus on improved membrane construction and the mechanism for nitric oxide removal. The prospects are excellent for resolution of these two remaining problem areas; at that point, development can proceed to tests of larger-scale modules. Still to be addressed at this next stage is the question of suspended particulates. Gas entrainment of particulates not removed upstream of the electrochemical cell is dependent on maintaining design velocity. This cannot be done in small-scale cells with contact time sufficient for required electrochemical transfer.